UNIVERSIDADE FEDERAL DE PERNAMBUCO
DEPARTAMENTO DE FÍSICA – CCEN
PROGRAMA DE PÓS-GRADUAÇÃO EM FÍSICA

JUAN MARCOS MARÍN RAMÍREZ

MAGNETIC PROPERTIES OF EUROPIUM CHROMITES ($EuCrO_3$)

Recife
2016

JUAN MARCOS MARÍN RAMÍREZ

MAGNETIC PROPERTIES OF EUROPIUM CHROMITES ($EuCrO_3$)

Dissertação apresentada ao Programa de Pós-Graduação em Física da Universidade Federal de Pernambuco, como requisito parcial para a obtenção do título de Mestre em Física.

Orientador:
Prof. Dr. Fernando Luis de Araujo Machado
Universidade Federal de Pernambuco

Co-Orientador:
Prof. Dr. Adolfo Franco Júnior
Universidade Federal de Goiás

Recife
2016

Catalogação na fonte
Bibliotecário Jefferson Luiz Alves Nazareno CRB 4-1758

M377m Marín Ramírez, Juan Marcos.
Magnetic properties of europium chromites ($EuCrO_3$) / Juan Marcos Marín Ramírez. – 2016.
117 f.: fig., tab.

Orientador: Fernando Luis de Araujo Machado.
Dissertação (Mestrado) – Universidade Federal de Pernambuco. CCEN. Física, Recife, 2016.
Inclui referências e apêndices.

1. Física da matéria condensada 2. Materiais magnéticos 3. Compostos de metais de terras-raras. I. Machado, Fernando Luis de Araujo. (Orientador). II. Titulo.

530.41 CDD (22. ed.) UFPE-FQ 2016-16

JUAN MARCOS MARÍN RAMÍREZ

MAGNETIC PROPERTIES OF EUROPIUM CHROMITES ($EuCrO_3$)

Dissertação apresentada ao Programa de Pós-Graduação em Física da Universidade Federal de Pernambuco, como requisito parcial para a obtenção do título de Mestre em Física.

Aprovada em: 10/03/2016.

BANCA EXAMINADORA

_____
Prof. Dr. Fernando Luis de Araujo Machado
Orientador
Universidade Federal de Pernambuco

_____
Prof. Dr. Adolfo Franco Júnior
Co-Orientador
Universidade Federal de Goiás

_____
Prof. Dr. Eduardo Padrón Hernández
Examinador Interno
Universidade Federal de Pernambuco

_____
Prof. Dr. Walter Mendes de Azevedo
Examinador Externo
Universidade Federal de Pernambuco

A mi madre Ruby y a mi querida familia.

Acknowledgements

We cannot tell the precise moment when friendship is formed [...] so in a series of kindnesses there is at last one which makes the heart run over.

Ray Bradbury (Fahrenheit 451)

It would take several pages to thank everyone involved even in a tiny part of this work, so for those that I may have omitted a forgiveness beforehand. I don't consider myself a very religious people, nevertheless I believe that there is something powerful above us, bigger than our comprehension. You can call it any way you want, for me, is *God*, so thank you for letting me be here in this moment of time and space. Every decision that I have made in my life has been supported by the most loving person in the world, my *mother*, **Ruby** who has inspired me always by example. Being away from home is not an easy task but it gets easier when you remember that there is a caring family behind your back, as my uncle *Nacho*, my two sisters *Mary* and *Luisa*, my nephews *Sebastian* and *Samuel*, from whom I have cherished every moment on their side. For almost nine years, someone has been the reason for many special moments, study sections, laughs and also who have offered me a shoulder to rest on through difficult times, being able to find love in each other is one of the highlights of my research in life so: *I love you, Johanna*.

To nine extraordinary friends a big hug and keep on engineering: *Anderson, Eduard, Jeison, Jhon, Felipe, Johanna, Liliana, Isabel and Deisy*. And the new ones: *Nacho, Johan, Edwin, Jaiver, Camilo, Sindy and Winnie*.

A big thank you to *Herminia*, *Danilo* and *Pablo* for their help and collaboration in every aspect of this research. To the *magnetocafé* crew, from whom I have learned to value the power of coffee, *Roberto, Obed, Paco, Rafael and Joaquin*. The guys from *Pelada DF* for the fun, the

goals and a nearly broken leg.

To my advisor Prof. *Fernando* who believe in me and gave me the chance to prove myself and study something that I love, when no one else did. My co-advisor professor *Adolfo* who also taught me and guide me in this period. To professors *Antonio*, *Eduardo*, *Sergio* and *Alexandre* for their help.

To the Institute of physics (IF) at the UFG and especially to the department of physics (DF) at the UFPE with their respective technicians, secretaries and general staff for their assistance throughout this dissertation. Finally, I would like to thank FACEPE (scholarship), CNPq, CAPES, and FINEP (Brazilian funding agencies).

“Now I understand,” Said the last man.

—ARTHUR C. CLARK (Childhood’s End)

Abstract

Rare earth chromites exhibit a diversity of interesting chemical and physical properties depending on the rare earth ion. $EuCrO_3$ shows a weak spontaneous magnetic moment below a Néel temperature of 181 K; attributed to a slight canting of the Cr^{3+} magnetic moments that are otherwise antiferromagnetically aligned. We have synthesized chromites by using a combustion reaction method applying urea as fuel. X-ray diffraction (XRD), Fourier transformed Infrared Spectroscopy (FT-IR), Scanning and Transmission Electron Microscopy (SEM and TEM), Thermogravimetric analysis and differential scanning calorimetry (TGA-DSC) were used to study the samples. The magnetization was measured by using a vibrating sample magnetometer (VSM) and a Physical Properties Measurement System (PPMS) at a wide range of temperature (5 K to 300 K). Rietveld analysis of the XRD data yielded to an orthorhombic structure (Pnma) for $EuCrO_3$, with an average crystallite size about 65 nm. Then, $EuCrO_3$ was doped with iron forming a mixed chromite $Eu_{1-x}Fe_xCrO_3$ ($0 \leq x \leq 1.0$). The presence of iron proved to be a source of microstrain in the system, due to the substitution of Eu^{3+} ions by Fe^{3+} in the perovskite structure. In fact, single phase $EuCrO_3$ is paramagnetic at room temperature. However, above x>0.2, an enhance in the exchange interaction among the magnetic ions. The magnetic properties of $Eu_{1-x}Fe_xCrO_3$ is accounted for by taking into consideration the lattice distortion introduced by the iron substitution in the $EuCrO_3$ perovskite structure mainly due to the large difference in the ionic radius of Eu^{3+} and Fe^{3+} and in their magnetic moments. One of the most important contributions of our work has been focus on the relation between the bond angle of Cr^{3+}-O^{2-}-Cr^{3+} and the Néel temperature. This angle is responsible for the weak magnetic behavior of the rare earth chromites. We have found that as a product of the induced stress the Néel temperature is modified, so does the bonding angle. This behavior has been also

found analyzing the shift towards higher values of the Hopkinson peak. To conclude, a thermal treatment at 800°C for the $Eu_{1-x}Fe_xCrO_3$ made at different times, shown a reduction in the microstrain of the system accompanied by an inhibition of the ferromagnetic-like character of the as-prepared samples.

Keywords: Rare earth chromites. Combustion reaction method. Magnetism.

Resumo

As cromitas, à base de terras raras, exibem várias propriedades químicas e físicas interessantes dependendo do íon de terra rara. $EuCrO_3$ mostra um momento magnético espontâneo fraco abaixo da temperatura de Néel (181 K); atribuída a uma ligeira inclinação dos momentos magnéticos do Cr^{3+} que são, de outra forma, antiferromagneticamente alinhados. Sintetizamos cromita de európio utilizando a técnica de reação por combustão. Difração de raios-X (XRD), espectroscopia de infravermelho por transformada de Fourier (FT-IR), microscopia electrónica de varredura e de transmissão (SEM e TEM), análises térmicas como termogravimetria e a calorimetria diferencial de varredura (TGA-DSC) foram utilizados para estudar nossas amostras. A magnetização foi medida usando um magnetómetro de amostra vibrante (VSM) e um PPMS (Physical Properties Measurement System) numa vasta região de temperatura (5 K até 300 K). O analises Rietveld dos difratogramas de XRD mostrou uma estrutura ortorrômbica (Pnma) para o $EuCrO_3$, com um tamanho médio de cristalito de 65 nm. Depois, o sistema foi dopado com ferro formando cromitas mistas do tipo $Eu_{1-x}Fe_x$ CrO_3 ($0 \leq x \leq 1{,}0$). A presença de Fe provou ser uma fonte de "micro-strain" no sistema, devido à substituição dos íons de Eu^{3+} por aqueles de Fe^{3+}. Na realidade, a fase pura de $EuCrO_3$ é paramagnética à temperatura ambiente. No entanto, acima de $x > 0,2$, uma melhora na interação de troca entre os íons magnéticos é encontrada. As propriedades magnéticas de $Eu_{1-x}Fe_xCrO_3$ são contabilizadas tendo em conta a distorção da estrutura introduzida pela substituição de ferro, principalmente devido à diferença no raio iónico de Eu^{3+} e Fe^{3+} e dos seus momentos magnéticos. A relação entre o ângulo de ligação de Cr^{3+}-O^{2-}-Cr^{3+} (responsável pelo magnétismo fraco das cromitas de terras raras em baixa temperatura) e seu efeito na temperatura de Néel é estudada. Verificou-se que como produto do "strain" induzido, a temperatura de Néel é modificada e o mesmo acontece

com o ângulo de ligação. Esse comportamento foi também encontrado analisando a mudança para valores mais elevados no pico de Hopkinson. Para concluir, um tratamento térmico feito a 800 °C para $Eu_{1-x}Fe_xCrO_3$ durante tempos diferentes, mostraram que existe uma redução no "micro-strain" do sistema acompanhado por uma inibição do caráter ferromagnético das amostras ($x > 0,2$).

Palavras-chave: Cromita de terras raras. Reação por combustão. Magnetismo.

Resumo em extenso

Devido este trabalho ser escrito completamente em inglês, como requerimento interno do programa de pós-graduação em física da UFPE, nesta seção será feito um resumo em extenso que contemple a síntese de cada capítulo ou partes do texto. Neste trabalho são apresentados resultados referentes às investigações de nanopós de cromita de európio ($EuCrO_3$) produzidos a partir do método de reação por combustão. Com o intuito de obter informações sobre os efeitos nas propriedades magnéticas e estruturais, esta cromita foi dopada com ferro ($Eu_{1-x}Fe_xCrO_3$). Dividido em seis capítulos, esse trabalho apresenta primeiramente uma breve descrição da dissertação. Seguido, no capítulo 2, de uma revisão sobre a importância e impacto das terras raras no desenvolvimento tecnológico, industrial e de pesquisa. Além de uma breve introdução de alguns dos trabalhos mais importantes na literatura que utilizam cromitas de terras raras. Esses materiais tem despertado um grande interesse devido a suas propriedades distintas, uma vez que dependem do íon de terra rara utilizado. Como, por exemplo, monocristais de cromita de európio ($EuCrO_3$) que apresentam um magnetismo (fraco) ao longo de um dos eixos cristalográfico, que é atribuído a uma ligeira inclinação de momentos do Cr^{3+}, que normalmente estão alinhados antiferromagneticamente, entretanto pouco foi feito até o presente momento para compreender a origem desse magnetismo. Sabe-se também que a $EuCrO_3$ apresenta um comportamento de vidro de spin e exchange bias em baixas temperaturas, com antiferromagnetismo abaixo da temperatura de Néel (181 K).

A teoria básica de magnetismo abordando os conceitos de momento magnético, magnetização e susceptibilidade magnética são vista no capitulo 3. Juntamente com a classificação dos materiais magnéticos com as principais classes desses materiais, divididos entre ferromagnéticos, ferrimagnéticos, e vários outros, os quais podem ser definidos em termos da orientação rel-

ativa e magnitude dos momentos magnéticos. É abordada a dependência da magnetização com a temperatura, em seguida, os vários tipos de anisotropia magnética, definida como a energia necessária para girar a direção da magnetização e por fim as interações magnéticas. No Capítulo 4 é apresentada a importância e os aspectos técnicos do método de reação por combustão para a produção de nanomateriais. Hoje em dia esta técnica de síntese é muito utilizada como uma rota alternativa e versátil, por se tratar de um método barato e fácil de usar. Uma das principais aplicações é na produção de cerâmicos para uma variedade de aplicações avançadas, por proporciona um bom controle na estequiometria e estrutura final do material desejado. Basicamente, o processo consiste em formar uma solução aquosa misturada com alguns sais de metais, nitratos, entre outros materiais, do composto que será preparado juntamente com um combustível orgânico (normalmente ureia). Com a ajuda de uma fonte de calor externa a solução atinge uma temperatura de combustão completando a reação, obtendo como resultando um pó cristalino, fino e seco. E nesse capítulo são apresentados conceitos básicos das técnicas de caracterização, divididas nas categorias: estruturais, magnéticas, térmicas, óticas e de microscopia.

No capitulo seguinte, é detalhado o processo da síntese das amostras estudadas ($EuCrO_3$ e as cromitas dopadas com ferro ($Eu_{1-x}Fe_xCrO_3$)) através do processo de reação por combustão, mencionando o calculo estequiométrico assim como os materiais utilizados no processo. No capítulo 6, têm-se os resultados e as análises das diferentes técnicas de caracterização. Na primeira parte, são apresentados os destaques da pesquisa sobre a síntese de EuCrO3 puro. Posteriormente, foi explorada a evolução do sistema com a dopagem de ferro e como as propriedades do composto são modificadas pela substituição de íons de Eu por aqueles de Fe, com o intuito de estudar a relação entre a temperatura de Néel e o ângulo de ligação entre os íons Cr^{3+}-O^{2-}-Cr^{3+}, sendo essa a relação importante para explicar o magnetismo fraco das cromitas de terras raras. E por fim, são apresentados três apêndices: no primeiro, a teoria clássica e quântica do paramagnetismo, juntamente com as regras de Hund, que fornece uma prescrição empírica para determinar o estado de menor energia de um átomo ou um íon. No segundo, uma descrição simples do set-up e a interface de usuário (feita com LabVIEW) para a medição de magnetoimpedância gigante e, no último apêndice, encontram-se resumos e eventos que foram apresentados durante a execução deste projeto.

List of Figures

List of Tables

Contents

1 Introduction

In this dissertation nanopowders of $EuCrO_3$ prepared using the combustion reaction method are investigated. This sample preparation technique offers some advantages in terms of easy stoichiometric control, time of synthesis and efficiency because in some cases there is no need for subsequent heat treatments to obtain the final product. It can be also considered as an alternative route of synthesis to those already reported [1, 2, 3, 4], with only a few studies on this topic [5, 6, 7]. In addition, the $EuCrO_3$ has been doped with iron in order to study its effect on the magnetic and structural properties. The morphology and composition of the samples were investigated by X-ray diffraction (XRD), scanning electron (SEM) and transmission (TEM) microscopy. Thermal analysis was performed using thermogravimetric analysis (TG) and differential scanning calorimetry (DSC). The magnetic properties of these compounds were studied using a vibrating sample magnetometer from 100 K to 300 K. Zero Field Cooling (ZFC) and Field Cooling (FC) curves were recorded down to 5 K by using a Physical Properties Measurement System (PPMS) in ACSM mode.

The present work is divided into six chapters. In the second chapter we have made a general review of the role and impact of both research and industry sectors of rare earth elements. As quoted by Kittel *"No other group of elements on the periodic table is as fascinating"* [8]. A brief introduction to some of the works develop to understand the rare earth chromites is presented with special emphasis in europium chromites. As our main objective is to understand the nature of magnetism in these chromites, a basic theory of magnetism is introduced in Chapter 3, with important concepts that are addressed in the manuscript. Chapter 4 explains the combustion reaction process in detail with their respective parameters; we have also made a brief description of the characterization techniques used throughout this work. Then, the sample preparation and conformation process of the nanometric powders are shown in Chapter 5.

Chapter 6 presents the final results and the discussions related to the research developed in the present work. Conclusions are presented in the last chapter. Three appendices are included. The first one about the classical and quantum treatment of paramagnetism with additional content about Hund's rules. The second displays the "construction" and programming of an improved control and data acquisition system for a giant magneto-impedance set-up at the calorimetry, transport and magnetometry lab. Finally, are presented the abstracts and events in which we participate during the execution of this project.

2 General overview

The magnetic properties of materials can be divided into two general categories: those that are structure sensitive and those that are not. Structure-insensitive refers to properties not markedly affected by changes in materials processing or by small changes in composition, including small amounts of certain impurities. Properties such as the saturation magnetization and resistivity are largely dependent on the composition of the particular alloy and are not changed substantially in the process of manufacturing. On the other hand, structure-sensitive properties are those that are drastically affected by impurities. These elements tend to locate at interstitial sites in the crystalline lattice and consequently, the lattice can be severely strained or elongated. As a result, small concentrations of these elements can have large effects on some of the magnetic properties like permeability, coercivity, hysteresis losses, remanence, and magnetic stability. These structure-sensitive properties are controlled by processing the material, including mechanical and thermal treatments [9]. Hence, it is important to study magnetic materials prepared by novel ways, which may lead to new and exciting properties.

2.1 Rare earth elements

The term rare earth (RE) is related to the fifteen metallic elements of the *lanthanide* series, coupled with the chemically similar yttrium, and occasionally scandium. In fact, they are not so rare at all and almost each one of them are abundant in earth's crust. The term "rare" is actually referred to their uneven distribution in low concentrations around the world. The term "rare earths" was suggested after their discovery by Carl Axel Arrhenius in 1787 in the dumps of the Ytterby (Sweden) quarries; "rare" because, when the first elements were discovered, he

thought that they were present only in small amounts, and "earths" because their oxides have an earthy appearance [10]. These elements are never found as pure metals, instead, they are found in a variety of minerals including silicates, oxides, carbonates, phosphates, and halides. Consequently, their extraction and production is complicated producing tons of pollution and industrial waste with potential environmental impact. Despite the importance of the RE's there are only few deposits being exploited at the moment. Fig. 2.1 shows that since 1990, China plays a dominant role in RE's production leading several countries (such as Japan and the USA) to a direct dependence of China's market with a continuous and almost critical increase in the demand for this resource [11]. China's Bayan Obo mine is one of the largest on the planet.

Rare earths are often divided into two categories: "light rare-earth element" (LREE) or "heavy rare-earth element" (HREE). The LREE are defined as lanthanum, atomic number 57 through gadolinium, atomic number 64. The HREE are defined as terbium, atomic number 65 through lutetium, atomic number 71, including also yttrium, $Z = 39$.

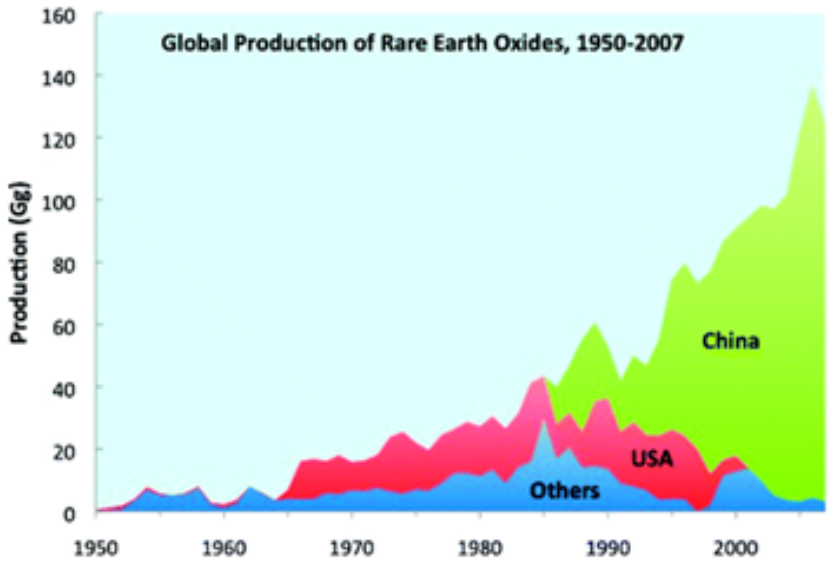

Figure 2.1: Global production of rare earth element [11].

But, why do we need rare earth elements? The answer is simple: because of their unique physical and chemical properties. Nowadays, they are used in a growing number of applications and have become indispensable for several critical technologies [11]. Demand have increased in recent years due to their growing usage in high-technology applications, including high strength permanent magnets, phosphors for electronic displays, and applications in a variety of renewable energy technologies, and as alloying agents in metals [12].

As stated before, rare earth elements have a noticeable nature of occurring together. Thus

Table 2.1: Electronic configuration and effective magneton numbers for trivalent lanthanide group ions [8]

		(Near room temperature)		
Ion	Configuration	Basic level	p(calc) = $g[J(J+1)]^{1/2}$	p(exp), approximate
Ce^{3+}	$4f^1 5s^2 p^6$	$^2F_{5/2}$	2.54	2.4
Pr^{3+}	$4f^2 5s^2 p^6$	$^3H_4$	3.58	3.5
Nd^{3+}	$4f^3 5s^2 p^6$	$^4I_{9/2}$	3.62	3.5
Pm^{3+}	$4f^4 5s^2 p^6$	$^5I_4$	2.68	—
Sm^{3+}	$4f^5 5s^2 p^6$	$^6H_{5/2}$	0.84	1.5
Eu^{3+}	$4f^6 5s^2 p^6$	$^7F_0$	0	3.4
Gd^{3+}	$4f^7 5s^2 p^6$	$^8S_{7/2}$	7.94	8.0
Tb^{3+}	$4f^8 5s^2 p^6$	$^7F_6$	9.72	9.5
Dy^{3+}	$4f^9 5s^2 p^6$	$^6H_{15/2}$	10.63	10.6
Ho^{3+}	$4f^{10} 5s^2 p^6$	$^5I_8$	10.60	10.4
Er^{3+}	$4f^{11} 5s^2 p^6$	$^4I_{15/2}$	9.59	9.5
Tm^{3+}	$4f^{12} 5s^2 p^6$	$^3H_6$	7.57	7.3
Yb^{3+}	$4f^{13} 5s^2 p^6$	$^2F_{7/2}$	4.54	4.5

a close chemical similarity is predicted. Furthermore, the fact that it took nearly 160 years to isolate and identify them give us a wider view of their likeness [13]. This similarity is mainly a consequence of a resemblance in their electronic configuration (Tab. 2.1), where the trivalent ions present in the outermost electron shell have a $5s^2 5p^6$ configuration and the $4f$ shell is empty. As the atomic number increases, it also does the occupation in the $4f$ shell, varying from 0 to 14 through the series from La (lanthanum-$4f$) to Lu (lutetium-$4f^{14}$). This occupation factor has a direct influence on the magnetic properties of rare earth elements because the $4f$ electrons are so deep in the atom. Some radial wavefunctions for rare earth atoms are shown in Fig. 2.2a; we can see that the $4f$ electrons are well embedded within the atom, and shielded by the $5s$ and $5p$ states from the surroundings. Thus, there is a very low contribution from the crystalline electric field of the surrounding ions; as if they were free electrons. Consequently, the orbital moment is not quenched, and the total magnetic moment has both orbital and spin components [14].

Another interesting characteristic is the so-called *Lanthanide contraction*. Rare earth elements exhibit a reduction of their ionic radii with increasing atomic number, thus the term contraction (Fig 2.2b). This reduction is smooth and goes from nearly 0.11 nm to 0.085 nm. The cause of the contraction is stated to be the imperfect shielding of one electron by another in the same subshell. Then, what distinguishes the magnetic behavior of one ion species from another is the number of $4f$ electrons compacted in the inner shell with a radius of perhaps 3

nm [8].

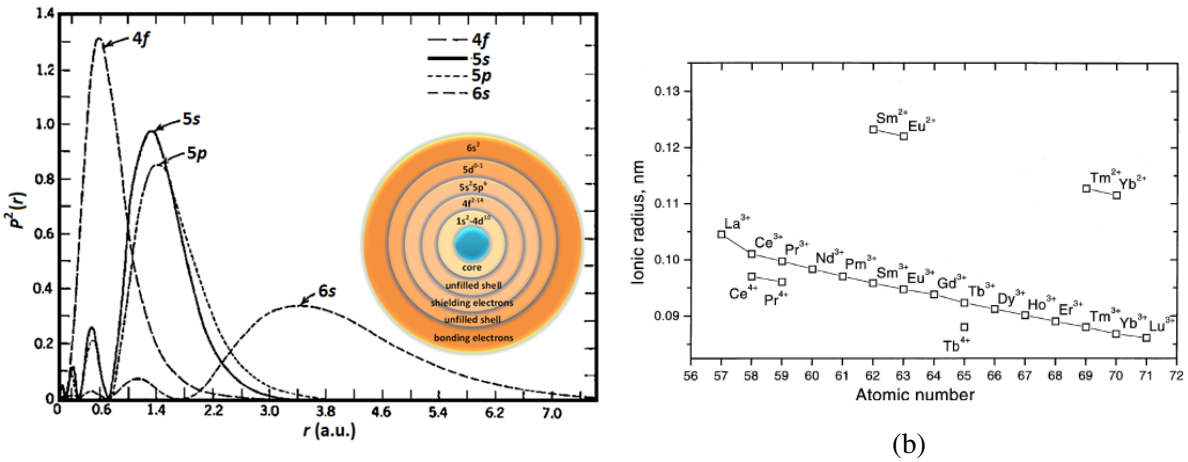

(a) (b)

Figure 2.2: (a) Wavefunction probability for rare earth orbitals; [13]; (b) Lanthanide contraction of rare earth trivalent ions [15].

Table 2.2: Effective magneton numbers for trivalent lanthanide group ions, theoretical and experimental values [16].

	Magnetic moment (M_B)						
	M_{eff}				M_s		
	Theory		Experiment		Theory		
R	Hund	V.V.-F.	3+ Ion	Metals	(gJ)	Experiment	Ref.
La	0	0	0	0			
Ce	2.54	2.56	2.52	2.51	2.14		38
Pr	3.58	3.62	3.60	2.56	3.20		39
Nd	3.62	3.68	3.50	3.3–3.71	3.27		40, 41
Pm	2.68	2.83	—	—	2.40		
Sm	0.85	1.55	—	1.74	0.72		38
Eu	0.00	3.40	—	8.3	0.0		42–4
Gd	7.94	7.94	7.80	7.98	7.0	7.55	45
Tb	9.72	9.70	9.74	9.77	9.0	9.34	46
Dy	10.64	10.6	10.5	10.65	10.0	10.20	47
Ho	10.60	10.6	10.6	11.2	10.0	10.34	48
Er	9.58	9.6	9.6	9.9	9.0	8.0	49
Tm	7.56	7.6	7.1	7.6	7.0	3.4	50
Yb	4.53	4.5	4.4	0.0	4.0		
Lu	0	0	0	0	0		

Rare earth metals display a strong anisotropy and also a predominant paramagnetic character, except scandium, yttrium, lanthanum, ytterbium, and lutetium. When cooled down, LREE remain paramagnetic for a maximum Néel temperature of 91 K, and then five of seven become antiferromagnetic. On the other hand, for HREE, we have that six become ferromagnetic at sufficiently low temperatures, and five of these (terbium, Tb, through thulium, Tm) pass through

an intermediate antiferromagnetic state before becoming ferromagnetic. Gadolinium (Gd) just misses being ferromagnetic at room temperature [14]. Fig. 2.3 shows the calculated effective moment using Hund's Rules (see appendix A). Experimental results confirm that those calculated are in good agreement with most of them, with a marked discrepancy for Sm^{3+} and Eu^{3+} ions. For these ions, it is necessary to consider the influence of the high states of the L-S multiplet, as the intervals between successive states of the multiplet are no longer compared to k_BT at room temperature [8]. The highest value of the magnetic moment of any naturally occurring element is shown by holmium, Ho, which is 10.34 μ_B per atom (Table 2.2), being almost five times greater than iron ($2.2\mu_B/atom$). The discussion about the nature of magnetism in rare earth elements could go on further, more information can be found in several textbook [8, 13, 14, 15, 16, 17, 18, 19].

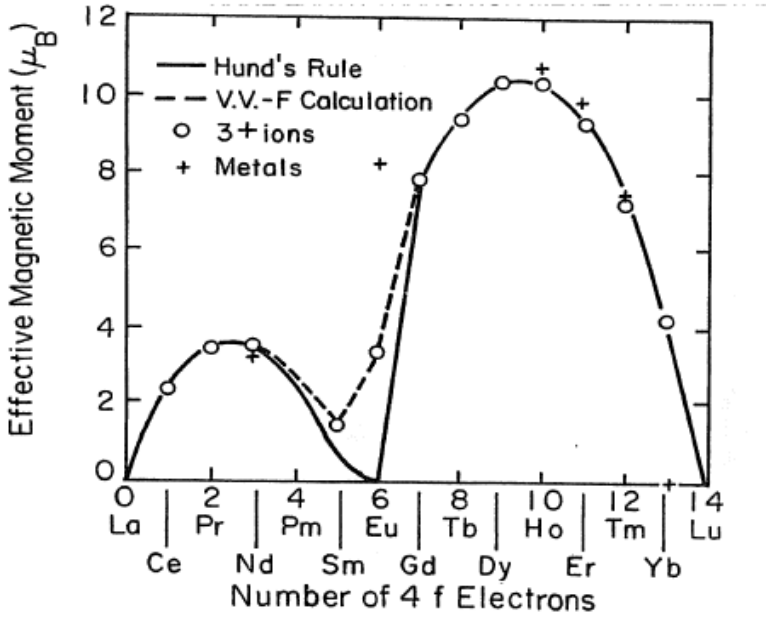

Figure 2.3: Variation of the Hund effective moment and the moments observed for +3 ions and metals of the rare-earth series [17].

After this brief introduction about rare earth elements, we will give a few insights about europium. This elemental material is utilized primarily for its unique luminescent behavior. Excitation of the europium atom by absorption of ultraviolet radiation can result in specific energy level transitions within the atom creating an emission of visible radiation. In energy-efficient fluorescent lighting, europium provides not only the necessary red but also the blue. Several commercial red phosphors are based on europium for color TV, computer screens, and fluorescent lamps. Its luminescence is also valuable in medical, surgical and biochemical applications [13].

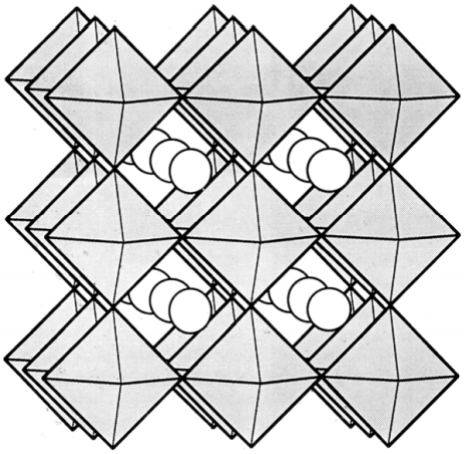

$$t = \frac{(r_A + r_O)}{\sqrt{(2)}(r_B + r_O)} \tag{2.1}$$

Figure 2.4: Perovskite structure. The A cations are represented by circles and the B cations are located at the center of the polyhedra: oxygenatoms are located at the apices of the polyhedra [20].

2.2 Rare earth based chromites

The perovskite nomenclature corresponds to any substance that adopts the same crystal structure as calcium titanate ($CaTiO_3$), namely, ABX_3. The understanding of functional ABX_3 (A: large cation with different valence, B: transition metal and X: oxides and halides) compounds is a very active research area with relevance to both fundamental and application issues. Structural prediction based on physical and chemical parameters is an important part of research in ABX_3 systems. Generally, for trivalent ABO_3 structures there are two principal factors involved in the evolution of the structure: (1) A and B cations of approximately equal size and of a size suitable for coordination within the octahedral interstitial site of a closest packed oxide framework; (2) an A cation comparable in size to O^{2-} which together with oxygen can form AO_3 closest packed layers with high coordination numbers in the A site. Oxides of the first group form sesquioxide structures, while among the second group we have a predominant tendency to perovskite structures (Fig. 2.4). To predict in which of the above categories our system will be formed, we can use several approaches, but the *tolerance factor* (t) has been widely accepted as a major criterion [20]. The Goldschmidt tolerance factor is calculated using Eq. 2.1, which gives us a general idea of the constraints necessary to form the perovskite structure, for example, for $0.8 < t \leq 1.0$ the perovskite structure often forms, while $t \leq 0.8$ sesquioxide structures form. Fig. 2.5 shows the cell parameters and tolerance factor for rare earth chromites, from this relation we can infer that almost each chromite forms a perovskite structure.

Ideal ABO_3 perovskites systems have B cations coordinated by six O anions while A cations

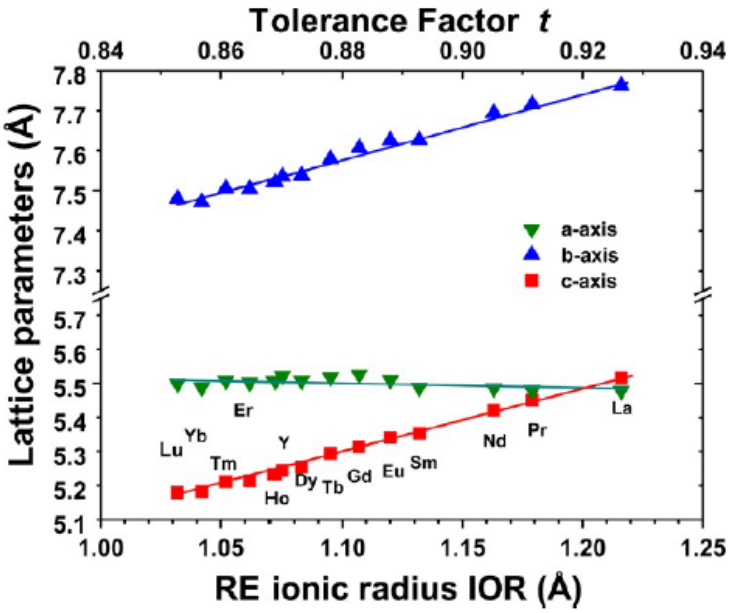

Figure 2.5: Lattice parameters *a*, *b*, and *c* versus the *RE* ionic radius and the perovskite tolerance factor for the (RE)CrO_3 series [3].

present coordination number 12 (also coordinated by O anions). The O anions have coordination number 2, being coordinated by two B cations, since the distance A-O is about 40% larger than the B-O bond distance [21]. One of the most interesting properties of perovskites is their particular capacity to adopt a multitude of different structural distortions. This is so because to the possible incorporation of almost every element of the periodic table into their structure. For example, magnetic and electronic interactions and the interplay between the two component elements, in our case, rare earth ion and transition metal, can be influenced.

Such distortions can be driven by external parameters, like temperature, pressure, or chemical composition, which leads to an extraordinary richness of physical properties within the family of perovskites [22]. Additionally, these materials have been receiving great attention from the scientific community in recent years due to the observation of a coupling effect between their electrical and magnetic properties. This magneto-electrical coupling has placed these materials in the class of *multiferroics*, which by definition are materials that exhibit more than one primary ferroic order parameter (ferromagnetism, ferroelectricity, ferroelasticity, and ferrotoroidicity) simultaneously. For example, magnetoelectric coupling typically refers to the linear magnetoelectric effect or the induction of magnetization by an electric field or polarization by a magnetic field [23]. However, this definition has been extended to include other long-range or non-primary order parameters, such as antiferromagnetism. The mutual control of electric and magnetic properties is of significant interest for applications in memory storage

devices, electric field-controlled ferromagnetic resonance devices, sensors, actuators and other potential devices. Only a few compounds ($BiFeO_3$ and $YMnO_3$) present these properties at relatively high temperatures. Heavy rare earth manganites have an analogous behavior [24]. In fact, rare earth chromites ($RECrO_3$) exhibit a diversity of interesting chemical and physical properties depending on the rare earth ion lying on the A site [25].

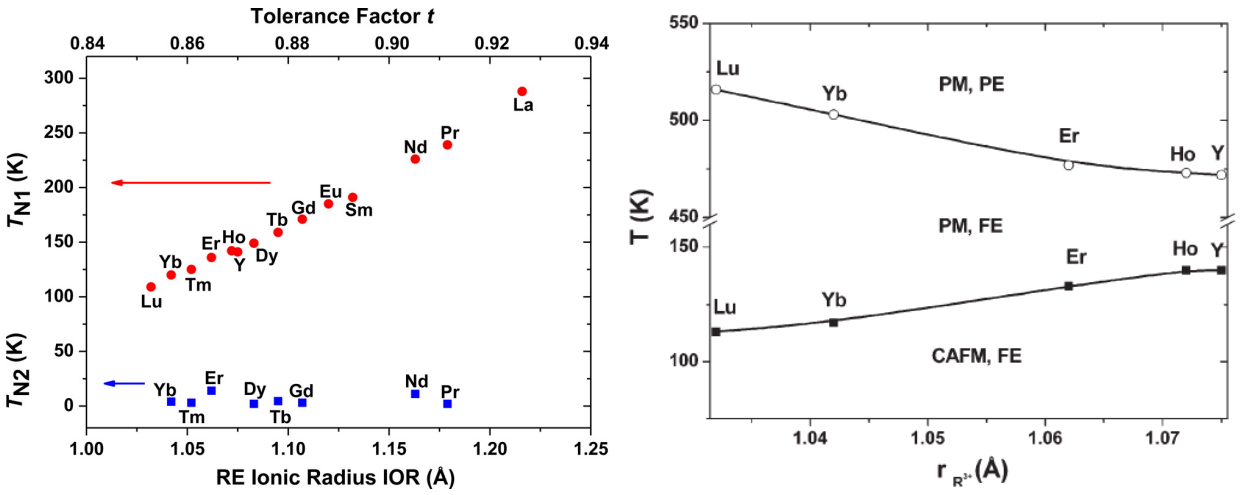

Figure 2.6: Néel temperature for the $Cr^{3+} - Cr^{3+}$ (T_{N_1}) and $RE^{3+} - RE^{3+}$ ordering (T_{N_2}) versus the RE IOR and the perovskite tolerance factor [3] and (b) Multiferroic phase diagram for some heavy rare earth elements [24].

$RECrO_3$ orthochromites have a rich variety of different magnetic spin interactions [26], where three different types may occur: (1) $Cr^{3+} - Cr^{3+}$, (2) $Cr^{3+} - RE^{3+}$, and (3) $RE^{3+} - RE^{3+}$, with isotropic, symmetric, and antisymmetric anisotropic exchange interactions, respectively. All of them are paramagnetic (PM) at room temperature and undergo several magnetic transitions upon cooling. The antiferromagnetic Néel temperature (T_N) for $Cr^{3+} - Cr^{3+}$ ordering increases with the RE cationic radius, which is associated with diminishing lattice distortions and increasing $Cr^{3+} - O^{2-} - Cr^{3+}$ bond angles approaching the ideal 180° (Fig. 2.6a) [3]. They also exhibit a canted-antiferromagnetic (CAFM) order of localized Cr^{3+} moments below the Néel temperature, with Cr^{3+} parallel to a crystallographic axis [24]. Other works have been also developed to understand the electric properties of these compounds [3, 24, 27]; ferroelectric (FE) measurements of the dielectric constant show that for heavy rare earth atoms there is a maximum value accompanied by a transition in a temperature range of nearly 500 K. It is also found that there is an inversely proportional relation between the rare earth ion size and dielectric constant. Based on its findings, Sahu *et al* [24] introduced a phase diagram to describe the

multiferroic properties of heavy rare earth ions, with three distinct regions: (i) CAFM-FE, (ii) PM-FE and (iii) PM-PE (Fig. 2.6b). One final remark was that the T_N decreases with the decrease in the radius of the rare-earth ion while the ferroelectric transition (T_E) increases slightly with a decrease in size.

Rare earth chromites are *p*-type semiconductors with conductivities larger than the parent rare earth oxide, but comparable to that of the corresponding transition metal oxide. The electrical transport properties of these solids can be explained in terms of the localized behavior of the *d*-electrons; there is also evidence of formation of small polarons. Among the three series of rare earth compounds, namely chromites, manganites and ferrites, chromites exhibit the highest conductivity, lowest activation energy, and largest drift mobility [28]. Some of the applications for the $RECrO_3$ systems have been related to properties such as, their electrical conductivity, oxidation resistance, and high melting points, which make them possible to be used as refractory conducting ceramics leading to applications in high-temperature furnace heating elements, interconnects in solid oxide fuel cell and potential gas sensing.

One interesting member of the $RECrO_3$ family is the europium-orthochromites ($EuCrO_3$) which are assumed to be crystallographically (and magnetically) isostructural with $GdFeO_3$, i.e. to crystallize in a distorted orthorhombic perovskite structure (space group *Pbnm*). Despite the discovery of the existence of soft magnetism along one of the crystallographic axes in monocrystals of this system in late 60's, this material remains as one of the less investigated for rare earth chromites. Thus, the origin and nature of its magnetic behavior have not been widely studied. As stated before, $EuCrO_3$ shows a weak spontaneous magnetic moment below a Néel

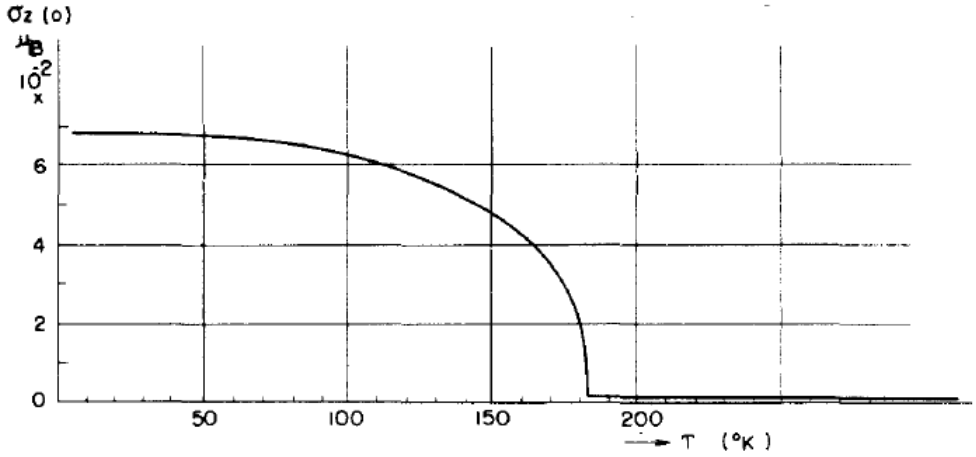

Figure 2.7: Temperature dependence of weak-ferromagnetic moment along *c*-axis of $EuCrO_3$. [1]

temperature of 181 K, attributed to a slight canting of the Cr^{3+} moments that are otherwise antiferromagnetically aligned. The direction of easy magnetization for this phenomena occurs along the *c*-axis of the cell, with the Cr^{3+} moment alignment. A Weak ferromagnetic moment was measured down to 4.2 K when approaching to 0 K the spontaneous moment has a magnitude of 0.07 μ_B per molecule (Fig. 2.7) [1]. It is known also, that $EuCrO_3$ undergoes a magnetic transition when subjected to high-power optical pumping and could thus be considered as an active medium in high-density optical storage and optical processing devices [5, 29]. The occurrence of the new state has been attributed to the dependent on exchange interaction between the Eu^{3+} ions, which become magnetic as a result of the pumping, via ions of the Cr matrix. Fig. 2.8 presents the magnetic susceptibility (χ) measurements for some chromites. They exhibit low values of χ and a ferrimagnetic moment below Néel temperature, as the difference between the ZFC-FC curve revealed. As explained before this moment is attributed to the small canting between the Cr^{3+}. In the case of $EuCrO_3$ and $LuCrO_3$, the RE magnetic ground state is diamagnetic and, therefore, the low temperature magnetic properties are dominated by the Cr^{3+} spin system [30].

A recent study has been made addressing the effects of calcium doping in the magnetic behavior of $EuCrO_3$ chromites [4]. At low Ca content ($x = 0.1$), a decrease in T_N is observed but the curve is rather similar to that of pure europium chromite, indicating a magnetic homogeneity at low temperatures, Fig. 2.9b. For the non-doped system using Curie-Weiss fitting, it has been found a Weiss temperature of -302 K that suggests a predominantly antiferromagnetic interac-

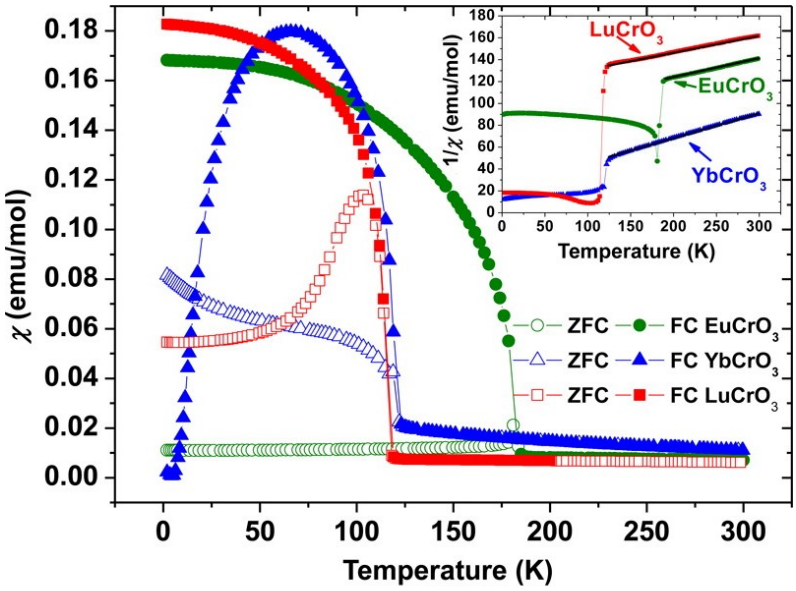

Figure 2.8: Magnetic susceptibility χ versus temperature T for $LnCrO_3$ [3].

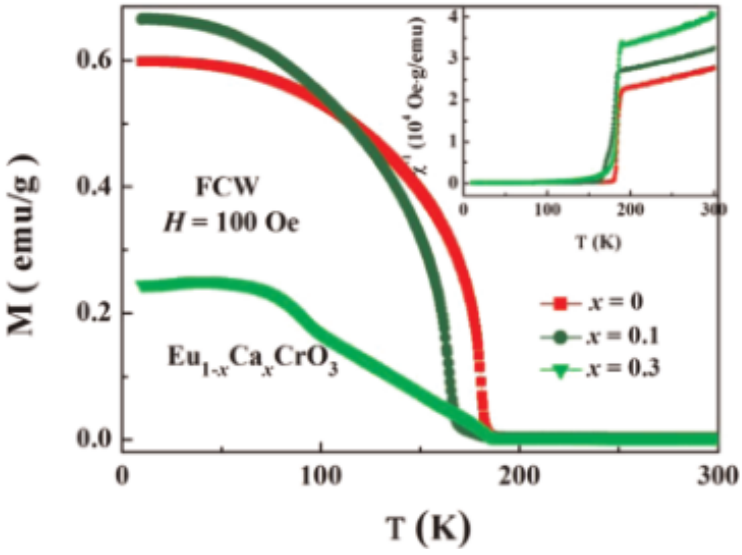

(a)

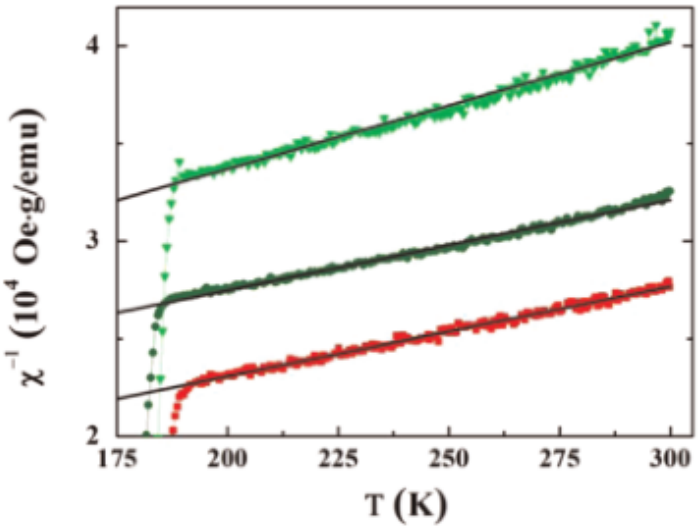

(b)

Figure 2.9: (a) Temperature dependence of magnetization with FC procedure at 100 Oe for $Eu_{1-x}Ca_xCrO_3$ and (b) $\chi^{-1}(T)$ in high temperature range [4].

tion below Néel temperature, confirming the presence of a canted antiferromagnet character. There is a reduction of the Weiss temperature when we compared the two doped chromites which have been connected to a lower value of the Curie constant, i.e. a reduced magnetization value as exposed in Fig. 2.9a. Above the Neél temperature, all the samples are paramagnetic. Considering the different types of ordering which the insertion of Ca^{2+} can introduce into the perovskite structure, the coexistence of two CAFM phases can be found. In fact for the sample with $x = 0.3$, the T_N cannot be obtained straightforwardly from the $M(T)$ curves since the

increase of M is obviously broadened (see Fig. 2.9a). This is attributed to the appearance of Cr^{4+} ions in the sample with the bivalent Ca^{2+} substitution of Eu^{3+}, which brings a disruption of the long-range antiferromagnetic order of Cr^{3+} ions. With increasing doping level, clusters with Cr^{3+}–O–Cr^{3+} ordering and different sizes may then distribute randomly in the sample. Finally, it has been found the presence of a spin-glass-like phase for $x = 0.3$ confirmed by the observation of magnetic relaxation, memory effect, and exchange bias.

To study the possible magnetoelectric properties of these materials ($RECrO_3$), there have been efforts to produce these compounds using various techniques, for example, direct hydrothermal [31], solid state or mechano-synthesis [2, 27], co-precipitation [32] and microwaved-assisted [3], even though prolonged synthesis time and calcinating steps are sometimes required. With the growing interest in nanostructured materials and nanocomposites, the study of this kind of systems demands an investigation that takes into account the morphology and particle size, and how these quantities affect the magnetic behavior of the end product; furthermore, there is a need to develop successful and simple alternative routes that can reduce the synthesis time and use of elevated temperatures, hence the introduction of self-propagating high-temperature synthesis or combustion reaction process, arises as a rapid and effective way to produce nanopowders of $EuCrO_3$ and doped related compounds [5, 6, 33].

3 Basic theory of magnetism

3.1 Introduction

Magnetism, the phenomenon by which materials assert an attractive or repulsive force or influence on other materials, has been known for thousands of years. The story of magnetism begins with a mineral called magnetite (Fe_3O_4), already known to the Ancient Greeks and Chinese over 2500 years ago. In the ancient world, the most plentiful deposits occurred in the district of Magnesia, in what is now modern Turkey, and our word magnet is derived from a similar Greek word, said to come from the name of this district [14].

One of the early application of magnetic materials was the compass. It was found that a properly shaped piece of magnetite, if supported so as to float on water, would turn until it pointed approximately north and south. Nowadays, many of our modern technological devices rely on magnetism and magnetic materials; these include electrical power generators and transformers, electric motors, radio, television, telephones, computers, and components of sound and video reproduction systems [34].

In 1269, Pierre de Maricourt found that the directions of a needle near a spherical natural magnet formed lines that encircled the sphere and passed through two points diametrically opposite each other, which he called the poles of the magnet. The first truly scientific study of magnetism was made by William Gilbert, who published his classic book *On the Magnet* in 1600. The relationship between magnetism and electricity was discovered in 1819 when, during a lecture demonstration, Hans Christian Ørsted found that an electric current in a wire deflected a nearby compass needle. In the 1820's, further connections between electricity and magnetism were demonstrated independently by Faraday and Joseph Henry showing that an electric current can be produced in a circuit either by moving a magnet near the circuit or by changing the

Table 3.1: Magnetic quantities and units [19].

Quantity	Symbol	CGS	SI	Conversion factor
Magnetic induction	**B**	G	T	10^{-4}
Magnetic field intensity	**H**	Oe	A m^{-1}	$10^3/4\pi$
Magnetization	**M**	erg G^{-1} cm^{-3} *or* emu cm^{-3}	A m^{-1}	10^3
Magnetic polarization	**J**	–	T	–
Magnetic moment	m	erg/G ($\equiv$ emu)	J T^{-1} ($\equiv$ A m^2)	10^{-3}
Susceptibility (volume)	χ	–	–	4π
Magnetic permeability	μ	G/Oe	H m^{-1}	$4\pi \times 10^{-7}$
Relative permeability	μ_r	–	–	1
Magnetic constant (vacuum permeability)	μ_0	G/Oe	H m^{-1}	$4\pi \times 10^{-7}$

current in a nearby circuit [35]. These observations demonstrate that a changing magnetic field creates an electric field and later in 1825 the first electromagnet was made. Research on magnetic materials can be said to date from the invention of the electromagnet, which made available much more powerful fields than those produced by lodestones, or magnets made from them [14].

Magnetic units may be a source of confusion because there are really two systems in common use. SI uses rationalized MKS (meter-kilogram-second); the others come from the CGS–emu (centimeter-gram-second–electromagnetic unit) system. In Table 3.1 are presented some magnetic quantities and units used and explained in this section. This table is useful to obtain the values of the quantities in the SI by multiplying the corresponding CGS values by the conversion factors [19].

3.2 Magnetic moment

First, it is necessary to defined the fundamental object in magnetism called the *magnetic moment* (**m**). In the classical representation proposed by Ampère a magnet is equivalent to a circulating electric current; then **m** can be represented by a tiny current loop. If the area of the loop is **A** square meters and the circulating current is I amperes, then

$$\mathbf{m} = I\mathbf{A}. \tag{3.1}$$

A generalization of the relation (eq 3.1) between the magnetic moment and the current is described by eq. 3.2 where $j(r)$ is now the current density at a point r, and $|j| = I/A$, where A is the cross section in which the current flows [36].

$$\mathbf{m} = \frac{1}{2}\int \mathbf{r} \times \mathbf{j}(\mathbf{r}) d^3 r \tag{3.2}$$

The magnetic moment of a free atom has three principal sources: the spin with which electrons are endowed; their orbital angular momentum about the nucleus; and the change in the orbital moment induced by an applied magnetic field [8]. Nevertheless, the corresponding nuclear moments are three orders of magnitude smaller than those associated with electrons, because the magnetic moment of a particle scales as 1/mass, therefore their effects are often neglected [36].

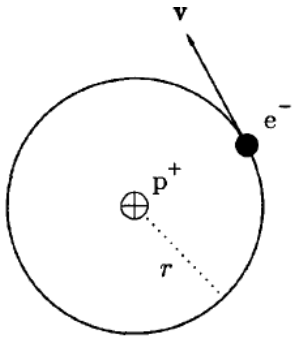

Figure 3.1: Classical model of an electron in a hydrogen atom orbiting with velocity v around the nucleus [37].

The electron spin is quantized in such a way that it can have just two possible orientations in a magnetic field, 'up' and 'down'. Spin is the source of the electron's intrinsic magnetic moment, which is known as the Bohr magneton [36]. Consider an electron (charge $-e$ and mass m_e) orbiting around the nucleus of a hydrogen atom with a velocity v and circular radius r (Fig. 3.1). Then, the induced current around the atom is $I = -e/\tau$, where $\tau = 2\pi r/v$ is the orbital period. If we defined the magnitude of the angular moment of the electron in the ground state as $\hbar = m_e v r$ then m is equal to Eq. 3.3, where μ_B is the Bohr magneton [37] (Eq. 3.4).

$$|m| = IA = I\pi r^2 = -\frac{e\hbar}{2m_e} = -\mu_B, \tag{3.3}$$

$$\mu_B = \frac{e\hbar}{2m_e}. \tag{3.4}$$

This is a natural unit of magnetic moment, just as the electronic charge e is a natural unit of electric charge. The magnitude of μ_B is equal to 9.27×10^{-24} Am^2.

3.3 Magnetization and magnetic susceptibility

When a piece of iron is subjected to a magnetic field, it becomes magnetized, and the level of its magnetism depends on the strength of the field. We, therefore, need a quantity to describe the degree to which a body is magnetized. The magnetization (**M**) then, is defined as the magnetic moment per unit volume (eq. 3.5), where V is large enough volume to ensure an average measure but small compared to the whole sample. Thus, one can have the local magnetization.

$$\mathbf{M} = \frac{1}{V} \sum_{i=1}^{n} \mathbf{m}_i. \tag{3.5}$$

Another important quantity to identify is the *magnetic susceptibility* (χ), which is the relation between the magnetization and the applied macroscopic magnetic field (**H**) as denoted in eq. 3.6. In both systems of units, χ is dimensionless. Sometimes the susceptibility is defined referred to unit mass or to a mole of the substance. The molar susceptibility is written as χ_M; the magnetic moment per gram is sometimes written as σ [8].

$$\chi = \frac{dM}{dH}. \tag{3.6}$$

The magnetic induction, or magnetic flux density, denoted by B, represents the magnitude of the internal field strength within a substance that is subjected to an **H** field. The magnetic field strength and flux density are related according to eq. 3.7. The parameter μ is called the permeability, which is a property of the specific medium through which the **H** field passes and in which **B** is measured.

$$\mathbf{B} = \mu \mathbf{H}, \tag{3.7}$$

$$\mathbf{B} = \mu_0 (\mathbf{H} + \mathbf{M}). \tag{3.8}$$

The magnetic induction in matter depends on the magnetic field intensity **H** and the magnetization **M**, and is given by eq. 3.8 where $\mu_0 = 4\pi \times 10^{-7}$ H/m (henry per meter) is the vacuum

permeability, or magnetic constant [19]. The relation between the permeability and susceptibility is given by eq. 3.9. The relative permeability μ_r is a dimensionless quantity defined as the ratio between μ/μ_0

$$\mu = \mu_0(1+\chi). \tag{3.9}$$

Temperature can influence the magnetic characteristics of materials, modifying its susceptibility. An increase in temperature leads to an increment in the magnitude of the thermal vibrations of atoms, therefore, the magnetic moments are free to rotate and randomize the directions of any moments that may be aligned. The first systematic measurements of the susceptibility of a large number of substances over an extended range of temperature were made by Pierre Curie and reported by him in 1895. He found that χ was independent of temperature for diamagnetics, but varies inversely with the absolute temperature for paramagnetics,

$$\chi = \frac{C}{T}. \tag{3.10}$$

This relation is called the *Curie law*, where C is the Curie constant specific for each material. A generalization of this law was made by Weiss on his theory of ferromagnetism in 1907, introducing the concept of *molecular field* capable of aligning the neighboring spins parallel to one another in the absence of an applied magnetic field. He considered that a molecular field could be produced at the site of one spin by the interaction of the neighboring spins [16] and shown that the Curie law is only a special case of eq. 3.11 called *Curie-Weiss law*. T_c is referred as the Curie temperature where the spontaneous magnetization due to the alignment of the atomic magnetic moments depends on temperature falls precipitously to zero (see Fig. 3.2). In the appendix A we discuss a little bit more these concepts.

$$\chi = \frac{C}{T - T_c}. \tag{3.11}$$

In an antiferromagnet, the spins are ordered in an antiparallel arrangement with zero net moment when **H** is parallel to the easy axis. As the temperature increases, the ordered spin structure tends to be destroyed, and the susceptibility increases, contrary to the case of the normal paramagnet. However, above some critical temperature, such spin ordering disappears completely, so that the temperature dependence of the susceptibility becomes similar to that of an ordinary paramagnet [16]. This temperature is known as the Neèl temperature which follows

the relation,

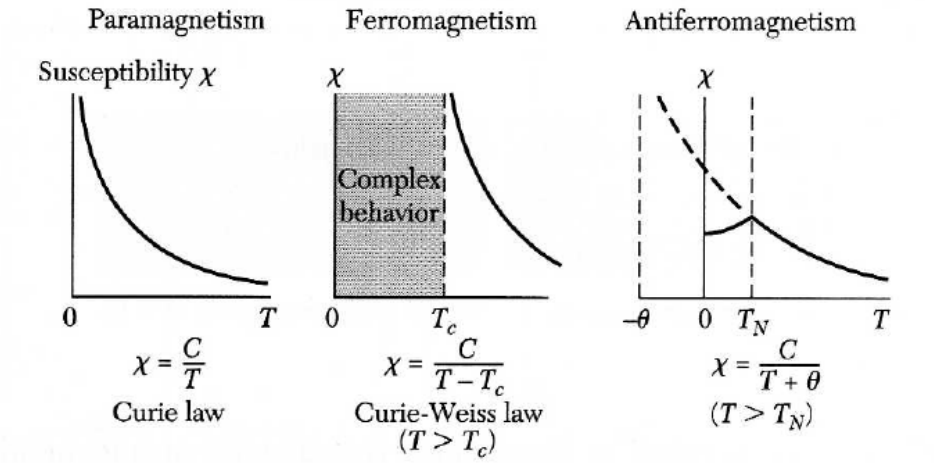

Figure 3.2: Temperature dependence of the magnetic susceptibility for different materials. [8]

$$\chi = \frac{C}{T+\theta}. \tag{3.12}$$

3.4 Classification of magnetic materials

The most interesting materials from the magnetism point of view are those, where atomic magnetic moments **m** are present. Systems where these moments exist, although are not ordered, are known as paramagnets, and usually contain atoms of d transition elements ($3d$, $4d$, $5d$), lanthanides ($4f$), and actinides ($5f$) [19]. Another type of material where all the contribution by the magnetic moments of the electrons are oriented such way that they cancel one another is called antiferromagnetic (see Fig. 3.3).

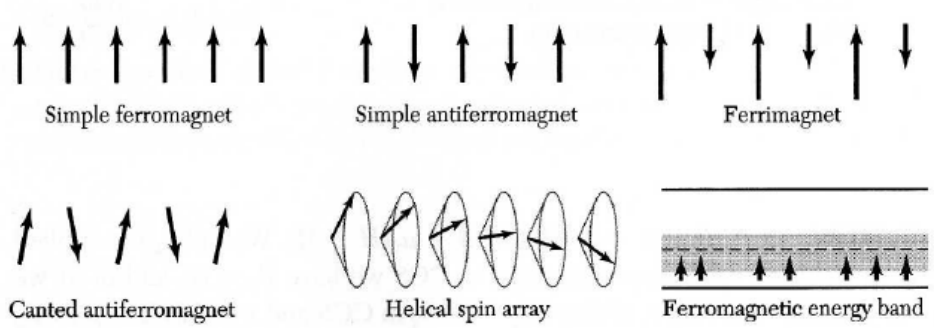

Figure 3.3: Ordered arrangements of electron spins [8].

Magnetically ordered materials, or shortly, magnetic materials; have a spontaneous mag-

netic moment **m**. The existence of a spontaneous moment suggests that electron spins and magnetic moments are arranged in a regular manner as schematized in Fig. 3.3 where the magnetic moments are represented by arrows. The main classes of magnetic materials can be defined in terms of the relative orientation and magnitude of the atomic or molecular magnetic moments, so we have ferromagnets, ferrimagnets, and several others. As presented in Chapter 2, at low-temperature europium chromite presents a transition from paramagnetic to canted antiferromagnetic behavior, hence, we shall introduce a brief definition on this kind of magnetism.

When spins with the same magnitude are perfectly antiparallel to each other there is no net magnetic moment and we have a perfect antiferromagnetism. Nevertheless, occasionally, the antiferromagnetic spins are not perfectly aligned in an antiparallel orientation, but are canted by a few degrees (Fig. 3.3) which give rise to a weak spontaneous net magnetic moment, this is called Canted Antiferromagnetism or CAFM. The interaction which gives rise to the canting was first explained by Dzialoshinski on grounds of symmetry and the thermodynamics of phase transitions. Later, Moriya included the effect of spin-orbit coupling in the superexchange Hamiltonian of a system with a non-degenerate orbital ground state to find an anisotropic exchange[38]. The history of CAFM has had a really strong connection with hematite because it was one the first materials studied that present this type of interaction.

3.5 Magnetic anisotropy

The magnetic hysteresis curves will have different shapes depending on various factors, such as whether the specimen is a single crystal or polycrystalline, temperature, stress, etc. One factor which may strongly affect the shape of the hysteresis loop is magnetic anisotropy, which simply means that the magnetic properties depend on the direction in which they are measured [14]. The natural direction of magnetization in a microscopic ferromagnetic domain is usually constrained to lie along one or more *easy axes*. Then, the magnetic anisotropy is defined as the energy that it takes to rotate the magnetization direction from the easy into the hard direction.

There are several kinds of anisotropy [39]

1. *Magnetocrystalline anisotropy.* The magnetization is oriented along specific crystalline axes.

2. *Shape anisotropy*. The magnetization is affected by the macroscopic shape of the solid.

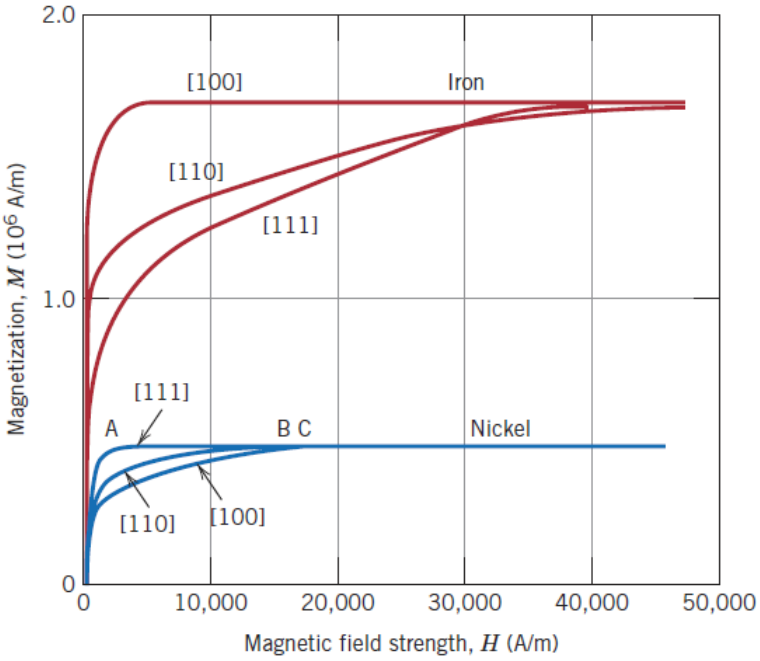

Figure 3.4: Magnetization curves for single crystals of iron and nickel [34].

3. *Induced magnetic anisotropy*. Specific magnetization directions can be stabilized by tempering the sample in an external magnetic field.

4. *Stress anisotropy (magnetostriction)*. Magnetization leads to a spontaneous deformation.

5. *Surface and interface anisotropy*. Surfaces and interfaces often exhibit different magnetic properties compared to the bulk due to their asymmetric environment.

Of these, only crystal anisotropy is intrinsic to the material. As seen in Fig. 3.4 for each of these materials (iron and nickel) there is one crystallographic direction in which magnetization is easiest—that is, saturation (of M) is achieved at the lowest H field; this is termed a direction of easy magnetization.

For cubic crystals[1] the crystal anisotropy energy E_a can be expressed in terms of a series expansion of the direction cosines of M_s relative to the crystal axes (Akulov, 1929). Let M_s make angles a, b, c with crystal axes and let α_1, α_2, α_3 be the cosines of these angles, which are called direction cosines. Then, the energy is achieved using Eq. 3.13, where $K_0, K_1, K_2, \cdots$ are constants for a particular material at a particular temperature.

$$E = K_0 + K_1(\alpha_1^2\alpha_2^2 + \alpha_2^2\alpha_3^2 + \alpha_3^2\alpha_1^2) + K_2(\alpha_1^2\alpha_2^2\alpha_3^2), \tag{3.13}$$

[1] bcc: Body-centered cubic, fcc: Face-centered cubic, simple cubic and others

In hexagonal crystals, like cobalt, which has an easy axis of magnetization along c axis with all of the other directions equally hard to magnetize. Thus, the anisotropy energy in a first approximation depends only on a single angle, the angle θ between the M_s vector and the c axis, and the anisotropy can be described as uniaxial with an energy E_a equal to Eq. 3.14. Elemental cobalt, barium ferrite, and many rare earth-transitional metal intermetallic compounds behave in this way [14].

$$E_a = K_0 + K_1 \sin^2 \theta + K_2 \sin^4 \theta. \tag{3.14}$$

The magnitude of the crystal anisotropy generally decreases with temperature more rapidly than the magnetization, and vanishes at the Curie point. Anisotropy is usually highly connected to the coercive field which goes to zero in the same way as the anisotropy. So, when anisotropy goes to zero (along with the coercive field) and a non-vanishing magnetization remains, a sharp peak is produced, this is the so-called Hopkinson effect. Hence, some susceptibility temperature dependences show a peak just below the transition temperature when heating the sample. This phenomenon was first noted for Hopkinson even before there was a theory to explain it [14]. Experiments have revealed that the Hopkinson effect is mainly dependent on crystal structure and magnetization. One of the accepted explanation for this effect is based only on domain-wall motion, when due to heating the domain wall mobility increases and consequently the magnetic susceptibility increases as well, which leads to a maximum in permeability [40]. The Hopkinson effect can be accounted for by the Stoner–Wohlfarth theory [41] (eq. 3.15), where $M_s(T)$ is the saturation magnetization, $H_a(T)$ is the magnetic anisotropy field of the particles at the temperature T, H is the fixed applying magnetic field and p is the packing fraction of the particles. Because both $M_s(T)$ and $H_a(T)$ decrease with increasing T, this competition produces a maximum of the magnetization near T_c, namely, Hopkinson peak [42]. Therefore, the Hopkinson effect; can be (and has been) used as a simple method to determine an approximate value of the Curie point.

$$M(T) = 2pM_s(T)H/3H_a(T). \tag{3.15}$$

3.6 Magnetic interactions

There are different types of magnetic interaction which are responsible for properties based on the fact that magnetic moments "feel" each other [39]. As a result, magnetic long range order can occur. With the concepts so far established, we can divide magnetism into two groups A and B. In group A we have materials where there is no interaction between the individual moments and each moment acts independently of the others (e.g. Dia- and pure paramagnetism). On the other hand, we have the group where magnetism occurs because the magnetic moments couple to one another and form magnetically ordered states. This exchange interaction between the neighboring magnetic ions will force the individual moments into parallel (ferromagnetic) or antiparallel (antiferromagnetic) alignment with their neighbors. In this section, we review some of the most relevant magnetic interactions from a basic point of view. For further discussion, refer to Chikazumi [16], Gezlaff [39] and Nolting [43].

3.6.1 Dipole-dipole interactions

Although this type of interaction is very weak (thousands of times smaller than the exchange interactions); the dipole interaction is very important in ferromagnetic materials, because leads to the formation of magnetic domains. Consider to magnetic dipoles m_1 and m_2 separated by the vector r, the energy of the system is given by Eq. 3.16, and thus depends on their distance and relative orientations of the magnetic moments (parallel or anti-parallel to each other). This expression (eq. 3.16) is only valid for $r \neq 0$. A general solution can be found in Yoshida (Chapter 2) [44]. The purely magnetic (dipole-dipole) forces are completely insufficient to provide a quantitative explanation for the high values of the Curie temperatures of the relevant magnetic materials, like Fe, Ni, and Co.

$$E = \frac{\mu_0}{4\pi r^3}\left(\mathbf{m}_1 \cdot \mathbf{m}_2 - \frac{3}{r^2}(\mathbf{m}_1 \cdot r)(\mathbf{m}_2 \cdot r)\right). \tag{3.16}$$

3.6.2 Exchange interactions

We describe now the physical origin of the interaction, which forces a ferromagnet into an ordered state below T_c. In the case of paramagnets, such an ordering is caused by an external

magnetic field. Therefore, it is reasonable to assume that, inside a ferromagnet, an internal magnetic field is produced, which, from now on, we call the *exchange field* or *molecular field*, which orients the existing permanent magnetic moments [43]. The exchange interaction was first treated by Heisenberg in 1928 to interpret the origin of the enormously large molecular fields acting in ferromagnetic materials and is responsible for the establishment of magnetic order in magnetic materials arising from a quantum effect with no classical analog, due to the indistinguishability of the electron [14].

Let us find then the interaction term between two electronic spins, which leads to the basic understanding of the ferromagnetic phenomena. The Schrödinger equation has the form:

$$\mathcal{H}\Psi = i\hbar\frac{\partial\Psi}{\partial t}, \tag{3.17}$$

If we suppose that there is no interaction between the spins we have a well-known solution, which is the sum of two partial hamiltonians

$$\mathcal{H}_0 = \mathcal{H}_0^1 + \mathcal{H}_0^2,$$

with eigenvalues $E_0 = E_m + E_n$ where m and n are quantum numbers to label each electron state. Now let us suppose that we have an interaction term between the electrons, originated by the coulombic potential $V_{12}(r_1, r_2) = e^2/r_{12}$. Thus, the halmiltonian can be described as:

$$\mathcal{H} = \mathcal{H}_0 + V_{12},$$

The energy states of the system in the presence of this perturbation is

$$E = E_0 + E_{12},$$

In order to find the eigenvalues of the system, we have

$$\begin{vmatrix} <1|\mathcal{H}_0+V_{12}|1> -E & <1|V_{12}|2> \\ <2|V_{12}|1> & <2|\mathcal{H}_0+V_{12}|2> -E \end{vmatrix} = 0$$

Considering $<1|V_{12}|1> = <2|V_{12}|2> = K_{12}$ and $<1|V_{12}|2> = <2|V_{12}|1> = \mathcal{J}_{12}$, becomes

$$\begin{vmatrix} (E_0+K_{12})-E & \mathcal{J}_{12} \\ \mathcal{J}_{12} & (E_0+K_{12})-E \end{vmatrix} = 0$$

So the eigenvalues are (Eq. 3.18)

$$E_{\pm} = E_0 + K_{12} \pm \mathcal{J}_{12}. \tag{3.18}$$

Where K_{12} is the electrostatic energy state of the electrons, and $\mathcal{J}_{12}$ is the so-called *exchange integral*. The autevectors are defined by Eq. 3.19

$$\Phi_{\pm} = \frac{1}{\sqrt{2}}(\Phi_1 \pm \Phi_2). \tag{3.19}$$

Experimentally has been observed that the total wavefunctions of a system is defined by the type of particle, for instance electrons or particles with half integer spin (*Fermions*) must be antisymmetric (A). On the other hand, particles with integer spin (*bosons*) have a symmetric (S) wavefunction. Then we must combined both, spacial (ϕ) and spin (χ) wavefunction in order to satisfy this conditions. For electrons then, we have two possible combinations,

$$\phi_A(r_1, r_2)\chi_S(\sigma_1, \sigma_2), \tag{3.20}$$

$$\phi_S(r_1, r_2)\chi_A(\sigma_1, \sigma_2) \tag{3.21}$$

where the symmetric (Eq. 3.22) and antisymmetric (Eq. 3.23) spin functions are the spin triplet and spin singlet states. Therefore, for two pair of spins $\frac{1}{2}$, we have three symmetric spin functions with total spin $S = 1$ (*parallel spins*), and one antisymmetric with spin $S = 0$ (*anti-parallel spins*).

$$\chi_S = \begin{cases} \uparrow_1\uparrow_2 \\ \frac{1}{\sqrt{2}}(\uparrow_1\downarrow_2 + \uparrow_2\downarrow_1) \qquad \text{Triplet state} \\ \downarrow_1\downarrow_2 \end{cases} \tag{3.22}$$

$$\chi_A = \frac{1}{\sqrt{2}}(\uparrow_1\downarrow_2 - \uparrow_2\downarrow_1) \qquad \text{Singlet State} \tag{3.23}$$

The sign of Eq. 3.18 and Eq. 3.19 must be the same, so if the sign is positive means that the space function is symmetric, therefore the spin wavefunction must be antisymmetric ($\uparrow\downarrow$). Hence, The state of minimum energy, or ground state corresponds to $\mathcal{J}_{12} < 0$ (antiferromagnetism). In the same way, a negative sign leads to a symmetric ($\uparrow\uparrow$) spin wavefunction then the ground state is equivalent to $\mathcal{J}_{12} > 0$ (ferromagnetism) [36, 45]. Consequently, the energy E in

these two cases depends on the relative orientation of the electronic spins; thus, to represent the interaction between the electrons, it suffices to introduce a term in the hamiltonian containing a factor

$$\mathbf{s}_1 \cdot \mathbf{s}_2.$$

This last term, plus the introduction of the interaction V_{12} leads to the appearance of a new energy term dependent of the relative orientation of the spins:

$$-2\mathcal{J}_{12} < \mathbf{s}_1 \cdot \mathbf{s}_2 > .$$

Finally, the hamiltonian which describes the interaction is

$$\mathcal{H} = -2\mathcal{J} \sum_{i<j} \mathbf{S}_i \cdot \mathbf{S}_j. \tag{3.24}$$

where now the sum is performed on each pair of atoms (i, j) and $\mathcal{J}$ is an effective exchange parameter. This is known as the *Heisenberg hamiltonian*, and it is widely used for the description of many magnetic properties of materials, particularly insulators [19].

To explain a little bit more conceptually the exchange interaction phenomena, we can suppose that two atoms with unpaired electrons approach each other. If the spins of these two electrons are antiparallel to each other, the electrons will share a common orbit, thus increasing the electrostatic Coulomb energy. If, however, the spins of these two electrons are parallel, they cannot share a common orbit because of the Pauli exclusion principle[2], so that they form separate orbits, thus reducing the Coulomb interaction [16]. When the two atoms are adjacent, we can consider electron 1 moving about proton 1, and electron 2 moving about proton 2. But electrons are indistinguishable, and we must also consider the possibility that the two electrons exchange places so that electron 1 moves about proton 2 and electron 2 about proton 1. This *exchange* introduces an additional term into the expression for the total energy of the two atoms.

If we expand the scalar product from Eq. 3.24 we reach,

$$\mathcal{H} = -2\mathcal{J} \sum_{i<j} \left(\mathbf{S}_i^x \mathbf{S}_j^x + \mathbf{S}_i^y \mathbf{S}_j^y + \mathbf{S}_i^z \mathbf{S}_j^z \right). \tag{3.25}$$

In highly anisotropic systems or under the effect of an external magnetic field, we could

[2]Pauli principle, forbids two electrons to enter in the same quantum state. Electrons cannot be in the same place if they have the same spin.

have a privileged spin direction, so the hamiltonian can be described as Eq. 3.26, better known as the *Ising hamiltonian*. This model accurately describes the magnetism of a large number of physical systems.

$$\mathcal{H} = -2\mathcal{J}\sum_{i<j}\mathbf{S}_i^z\mathbf{S}_j^z. \tag{3.26}$$

3.6.3 Indirect exchange interactions

Depending on the distance between the magnetic moments we distinguish between the direct and indirect exchange. The situation that the electrons of neighboring magnetic atoms directly interact is called "direct exchange" because the interaction is mediated without needing intermediate atoms. If the overlap of the involved wave functions is only small (e.g. for rare earth metal atoms with their localized $4f$ electrons) then the direct exchange does not represent the dominating mechanism for magnetic properties. For this class of systems, the indirect exchange interaction is responsible for magnetism [39].

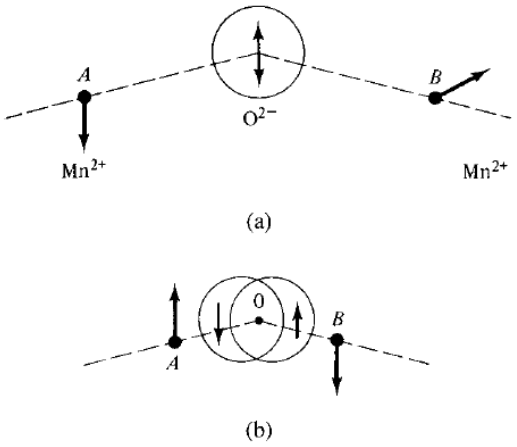

Figure 3.5: Superexchange [14].

The direct exchange mechanism, as presented before is frequently not acceptable as a coupling mechanism for magnetic materials for the reason that the separation between the magnetic ions is too large. Then, we have the indirect exchange. There are, however, a number of indirect exchange mechanisms which, within the framework of second-order perturbation theory, lead to an effective hamiltonian of the Heisenberg type [43]. Some of them are briefly presented in this section.

Superexchange. This type of indirect exchange interaction occurs in ionic solids. The

exchange interaction between non-neighboring magnetic ions is mediated by means of a non-magnetic ion which is located in-between. In these structures, the positive metal ions, which carry the magnetic moment, are too far apart for direct exchange forces to be of much consequence. Instead, they act indirectly through the neighboring anions (negative ions). Consider, for example, two Mn^{2+} ions being brought up to an O^{2-} ion from a large distance, as in Fig. 3.5(a). The directions of the moments on these two ions are at first unrelated. The oxygen ion has no net moment. But imagine that the outer electrons of the oxygen ion constitute two superimposed orbits, one with a net spin up, the other with a net spin down, as pictured in Fig. 3.5(a). When a manganese ion with an up spin is brought close to the oxygen ion, the up-spin part of the oxygen ion will be displaced as in Fig. 3.5(b) because parallel spins repel one another. If now another manganese ion is brought up from the right, it is forced to have a down spin when it comes close to the up-spin side of the "unbalanced" oxygen ion [14].

RKKY exchange (Ruderman, Kittel, Kasuya, Yosida). This is an indirect interaction between magnetic ions, which is mediated by quasi-free, mobile electrons in the conduction band. Was proposed in 1954 for Ruderman and Kittel and later develop by Kasuya and Yosida. They showed that a single magnetic impurity actually creates a nonuniform, oscillating spin polarization in the conduction band, which often results in complicated spin arrangements and leads to long-range oscillatory coupling between core spins (Fig. 3.6a). For free electrons, the polarization is proportional to the RKKY function (Eq. 3.27), where k_F is the Fermi wavevector [36].

$$F(\xi) = \frac{(\sin\xi - \xi\cos\xi)}{\xi^4}, \qquad (3.27)$$
$$\text{with } \xi = 2k_F r.$$

It is a type of coupling observed in particular in metallic $4f$-systems like rare earths. Among the rare-earth metals, only gadolinium has S as a good quantum number. The others have J as their quantum number, yet the exchange interaction couples spin. We, therefore, need to project S onto J when calculating the exchange coupling, whether direct or indirect. Since $L+2S = gJ$ and $J = L+S$, $S = (g-1)J$. This introduces a factor $(g-1)^2 JJ(J+1)$ into the exchange coupling. The factor is squared because the spin enters the exchange interaction between two rare-earths twice. The effective coupling is

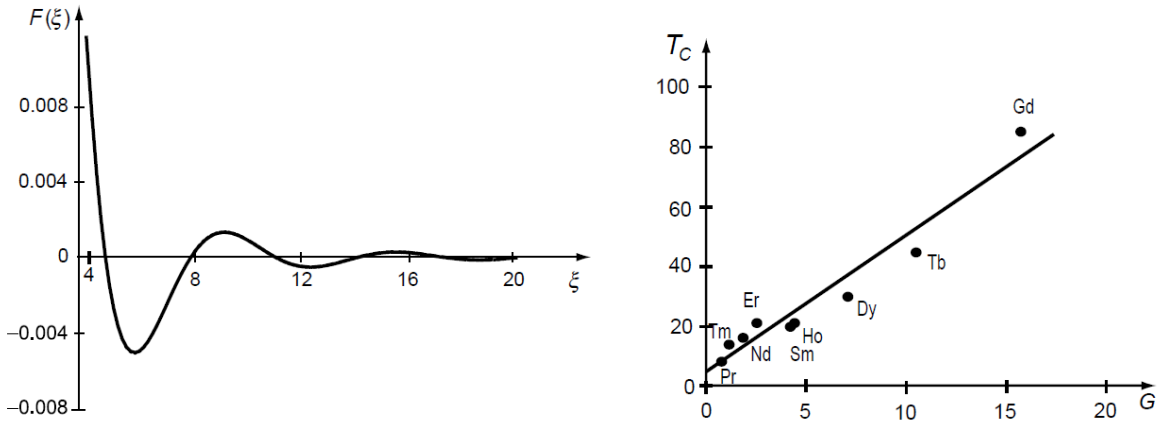

(a) (b)

Figure 3.6: (a) The RKKY function $F(\xi)$ [36]; (b) T_c as function of the de Gennes factor [36].

$$J_{RKKY} = GJ_{eff}, \tag{3.28}$$

where $G = (g-1)^2 J(J+1)$ is the *de Gennes factor*. In Fig. 3.6b is presented the evolution of the T_c against the de Gennes factor.

Double exchange. This interaction arises between $3d$ ions which have both localized and delocalized d electrons. Unlike ferromagnetic superexchange, mixed valence configurations are required for double exchange. One example is given by magnetite (Fe_3O_4) which includes Fe^{2+} as well as Fe^{3+} ions.

3.7 Mean field approximation

We can find the relation between the Weiss molecular field and the Heisenberg hamiltonian using the mean field approximation [19]. Considering the interaction of an atom with spin $\mathbf{S}_i$ with its z nearest neighbors:

$$\mathcal{H}_i = -2\mathcal{J}\sum_{j}^{z} \mathbf{S}_i \cdot \mathbf{S}_j.$$

Expressing this in terms of the projection σ ($\sigma = (g-1)J$) of S on the direction of the total angular momentum J, we have

$$\mathcal{H}_i = -2\mathcal{J}\sum_j^z \sigma_i \cdot \sigma_j.$$

Assuming the presence of a spontaneous magnetization over the individual magnetic moments provided by a *molecular field* with intensity $\lambda_m \mathbf{M}$ and proportional to the mean magnetic moment $\bar{\mu}$

$$H_{eff} = \lambda_m \mathbf{M} = \lambda_m n \bar{\mu} = -\lambda_m n g \mu_B \langle J \rangle_T,$$

where n is the number of magnetic moments per unit volume and $\langle J \rangle_T$ is the thermal average of J. We can approximate the ion i interaction, assuming that the sum is made over the z nearest neighbors

$$\mathcal{H}_i = -2\mathcal{J}(g-1)^2 \left(\sum_j^z J_j \right) \cdot J_i \approx -2\mathcal{J}(g-1)^2 z \langle J \rangle_T J_i. \tag{3.29}$$

Remembering that the Hamiltonian of the magnetic moment in the presence of an external effective field is:

$$\mathcal{H} = -\mu \cdot H_{eff}. \tag{3.30}$$

Using the fact that $\mu = -g\mu_B J$ and from both Eq. 3.29 and Eq. A.14 we obtain the relation between $\mathcal{J}$ and the molecular field (Eq. 3.31).

$$\mathcal{J} = \left(\frac{n g^2 \mu_B^2}{2z(g-1)^2} \right) \lambda_m. \tag{3.31}$$

We can establish an approximate connection between the exchange integral J and the Curie temperature T_c (Eq. 3.32). Where z is the number of nearest neighbors, each connected to the central atom by the interaction $\mathcal{J}$ and k_B the Boltzmann constant.

$$\mathcal{J} = \frac{3k_B T_c}{2zS(S+1)}. \tag{3.32}$$

One final remark is that this mean field approximation is only applicable if the amplitude of the fluctuations in the magnetic field acting on the atomic moments is not very large on a given site, and if it is small from point to point [19].

4

Experimental method and characterization techniques

4.1 Combustion reaction synthesis

Combustion synthesis (CS) or self-propagation high-temperature synthesis (SHS) is an effective, low-cost reactive method for production of several industrially useful materials involving capabilities such as material improvement, energy saving, and environmental protection[46]. Nowadays combustion synthesis is highly used as a versatile alternative route to produce nanomaterials and has been used in the production of various ceramic powders for a variety of advanced applications because provides a good control in stoichiometry and structure, homogeneous microstructural products, cheap and easy to use and implement in any laboratory [25, 47].

The process consist in taking an aqueous solution mixture with some salts, metal nitrates, among others, of the desirable compound and added with an organic fuel (mainly urea $CO(NH_2)_2$) to boil, until the mixture ignites and a self-sustaining and rather a fast combustion reaction takes off, resulting in a dry, usually crystalline, fine powder [48, 49]. A detail schematic diagram showing the stages followed during the synthesis is shown in figure 4.1. First, we mixed both metal nitrates and fuel using diluted water until achieved a homogeneous solution in a ceramic recipient. Then, this liquid is mounted onto a preheated hot blanket where after a few minutes the sample starts to boil liberating first water with a subsequent release of other gases until finally react and ignites generating a fragile foam. With the help of an agate mortar and pestle, a fine powder is accomplished.

This technique is characterized by being highly exothermic with a high heat release rate, which can lead to an explosive reaction to maintain a self-propagation high temperature or the appearance of a flame result of the large amounts of gases present in the synthesis [25, 48]. This method is far from equilibrium, based on the principle that once an exothermic reaction

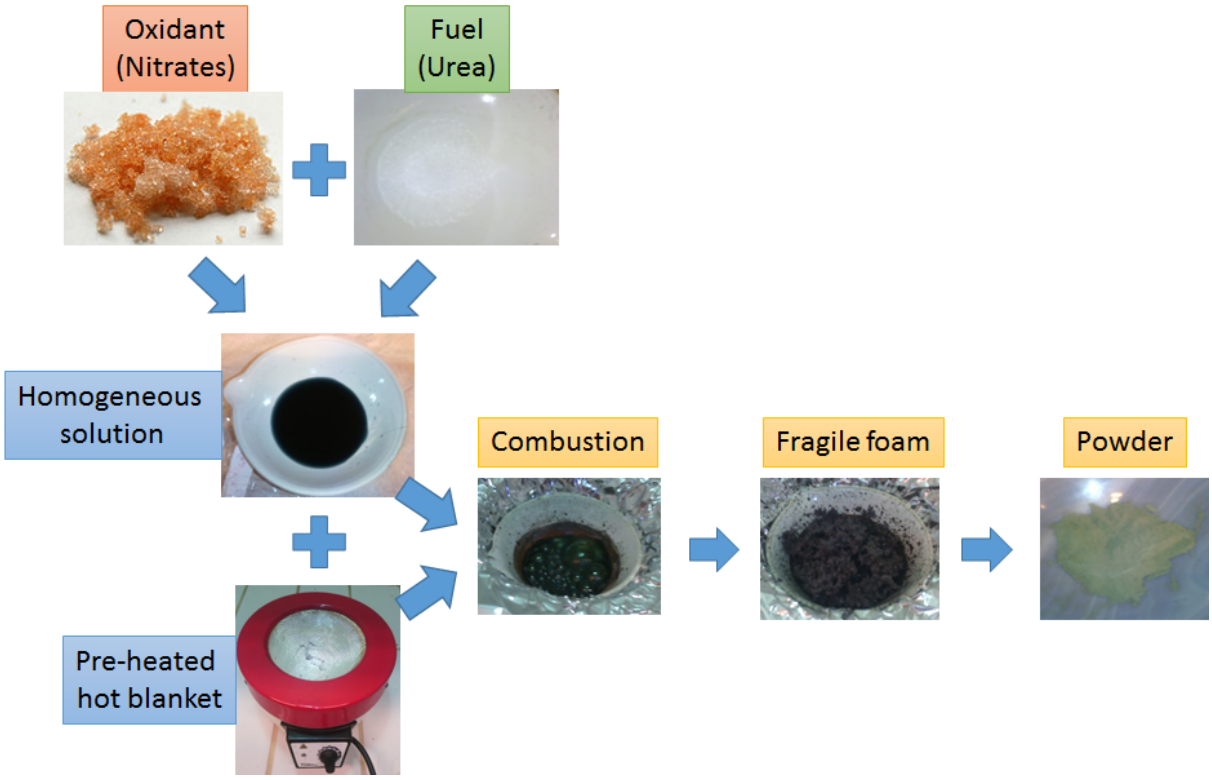

Figure 4.1: Stages for combustion reaction process.

takes place and becomes self-sustain a final product is achieved in a short period of time and in some cases without the need for a subsequent heat treatment [50]. The properties of the resulting powders (crystalline structure, amorphous structure, crystallite size, purity, specific surface area and particle agglomeration) depend heavily on the adopted processing parameters, although not many studies have an emphasis on this particular topic. Some of them are listed below.

Table 4.1: Flame types [51]

Type	Temperature	Burning rate
Flaming (gas phase)	Over 1,000 °C	–
Smouldering (Solid-gas phase)	Below 1,000 °C	~cm/s
Explosive type	High temperature and pressure	4000–8000 m/s

Flame types. Generally, during the combustion reaction the release of heat from the chemical burning of the transformed substances produce a flame. The flame changes according to the chemical elements used in the synthesis and has certain characteristics depending on the maximum temperature reached. The table 4.1 shows some flame types according to its behavior and temperature. A large number of factors influences the flame temperatures. The flame temperature can increase with the addition of excess oxidants, such as nitrate ammonium, or

the increase of the fuel-oxidant.

Characteristic temperature. Literature reports four kinds of temperatures achieved in the combustion process [47, 52]:

- Initial temperature (T_o) is the average temperature of the reagent solution before the reaction is ignited.
- Ignition temperature (T_{ig}) represents the point at which the combustion reaction is dynamically activated without an additional supply of external heat.
- Adiabatic flame temperature (T_{ad}) is the maximum combustion temperature achieved under adiabatic conditions.
- Maximum flame temperature (T_m) is the maximum temperature reached in the actual configuration, i.e., under conditions that are not adiabatic.

Gas generation. The quantity of gas liberated from the reaction are closely related to particle size and surface area, being responsible for breaking large clusters and creating pores between particles. In fact, the clusters disintegrate in conditions of high production of combustion gases where more heat from the system is released, hindering particle growth [47].

Fuel-oxidant ratio. The thermochemical concepts used in propellant chemistry are the cornerstone where combustion reaction synthesis have established their principles. The composition of a fuel-oxidizer mixture is important in the field of propellants and explosives for various reasons, therefore, this is one of the most important parameters in order to have a good combustion synthesis reaction and various studies have paid attention to this subject.

The relation that usually determines the fuel richness or leanness of a combustible mixture is based on two parameters, $\phi = \phi_m/\phi_s$, where ϕ_m is the mixture ratio (fuel/oxidizer) and ϕ_s is the stoichiometric ratio. For $\phi > 1$ the mixture is fuel lean and $\phi < 1$ shows a fuel rich behavior [53]. The first correction to this relation was proposed by Bakhman [54], when for a given value of ϕ different mixtures may differ substantially with respect to oxygen balance. This new approach prove to be tricky and quite tedious, because involves solving and balancing chemical equations, thus in his work Jain *et al* [55] report an easier method to obtain this coefficient, (Φ_e) (see eq. 4.1), finding similar results to those of Bakhman.

$$\Phi_e = \frac{\sum C_o \times \text{ valency}}{(-1)\sum C_r \times \text{ valency}} = \frac{p}{r}. \tag{4.1}$$

Where C_o is the coefficient of oxidization and C_r coefficient of the reduction element in molar units both of them. p and r are integers representing the total composition of the oxidizing and reducing elements respectively in the mixture [55]. For an stoichiometrically balanced mixture $\Phi_e = 1$. One last consideration should be made due the empirical character of these calculations, being necessary in many cases to increase the concentration of fuel. Applying thermochemical concepts from propellant chemistry to the synthesis, the total sum of the products of the cation and anion valences by the stoichiometric coefficients should be zero (eq. 4.2).

$$\sum \text{oxidant element coefficients} \times \text{Valences} + \sum \text{reduct element coefficients} \times \text{Valences} = 0. \quad (4.2)$$

Some finals remarks about the combustion synthesis reaction are aimed at the nature of the precursors. The oxidants are often nitrates, being chosen as metal precursors, not only because they are fundamental to the combustion method, for providing the metal ion, but also because of their great water solubility, allowing a greater homogenization, moreover, the water molecules do not affect the nitrate valence, thus are irrelevant for the reaction [47].

Urea ($CO(NH_2)_2$) is largely employ as fuel for its high exothermicity and low cost [56]. This combustible is also attractive for originating the formation of powders with crystallite sizes in the submicron/nanosize range and act as a complexing agent for metal ions because it contains two amino groups located at the extremes of its chemical structure [47].

4.2 Characterization techniques

The characterization of the samples was made using the facilities of the Physics department (Departamento de Física-DF) at the Universidade Federal de Pernambuco (UFPE) and the Institute of physics (Instituto de Física-IF) at the Universidade Federal de Goiás (UFG).

4.2.1 X-ray diffraction

The German physicist Wilhelm Conrad Röntgen discovered in early in 1895 a new kind of radiation that he called “X-rays” [57, 58] due its unknown nature. It was only until 1912 that another German physicist Max von Laue with the help of some colleagues at University of Munich, develop a theory based on the idea of diffracting X-rays by means of crystals. If

crystals were composed of regularly spaced atoms, which might act as scattering centers for X-rays, and if X-rays were electromagnetic waves of wavelength about equal to the interatomic distance in crystals, then it should be possible to see some interaction between them [59, 60]. It was still the year 1912, when two English physicists, W. H. Bragg and his son W. L. Bragg, successfully analyzed the Laue experiment and were able to express the necessary conditions for diffraction in a somewhat simpler mathematical form than that used by von Laue [59, 58]. All of these developments gave birth to a new brand field named X-ray crystallography.

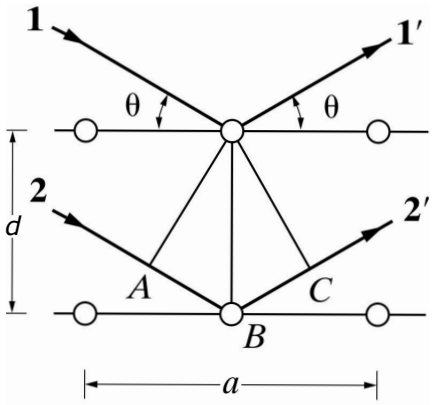

Figure 4.2: Diffraction of a X-ray beam in a single crystal, configuration $\theta - 2\theta$ [59]

Diffraction is essentially a scattering phenomenon in which a large number of atoms cooperate, which need two indispensable elements: a wave motion capable of interference (X-rays) and a set of periodically arranged scattering centers (the atoms of a crystal). When this radiation with a certain wavelength (λ) is incident at a certain angle (θ) over some crystalline planes spaced a specific distance (d) diffraction appears (Fig. 4.2). The phase relation is such as destructive interference can occur in most directions of scattering, but in a few directions constructive interference takes place and diffracted beams are formed and produce a characteristic X-ray pattern [59]. Using the expression introduced by Bragg (eq. 4.3) that relates the entities involved in the diffraction phenomenon some information can be found, such as interplanar distance (d_{hkl}) associated with the lattice parameter of the crystal cubic cell (eq. 4.4).

$$2d_{hkl}\sin\theta = n\lambda, \tag{4.3}$$

$$d_{hkl} = \frac{a}{\sqrt{(h^2+k^2+l^2)}}. \tag{4.4}$$

In the eq. 4.4, h, k and l correspond to the miller indices of a particular crystal lattice posi-

tion. From the diffraction pattern can be also estimated the mean crystallite size as a measure of the width of the principal diffracted peak (most intense) with Scherrer's equation 4.5. Before applying eq. 4.5 to experimental data, it is necessary to correct the observed diffraction line widths for geometrical and instrumental effects (β), employing the Warren correction [61].

$$\tau = \frac{0.9\lambda}{\beta \cos\theta}. \tag{4.5}$$

A most accurate method was developed by Hugo Rietveld around 60's decade. Rietveld's refinement method is capable of accurately determining structural parameters of the sample allowing the extraction of the maximum amount of information contained in the powder diffractogram, starting from the construction of a theoretical model that fits the experimental diffraction pattern by a least square method. As proposed by Rietveld, the least-squares parameters can be divided into two groups. The first group is the profile parameters; define the positions, the halfwidths, and the possible asymmetry of the diffraction peaks in addition to a property of the powder sample i.e. preferred orientation. The second group, the structure parameters, define the contents of the asymmetric unit cell [62]. There are several software systems that used this method to analyze x-ray diffraction patterns, among them MAUD [63] is one of the most exciting, suitable for its simplicity and multi-platform orientation.

4.2.2 Magnetic characterization

To experimental study, a magnetic material it is required (a) a means of producing the field which will magnetize the material, and (b) a means of measuring the resulting effect on the material [14]. As previously stated, some of the basic magnetic information in a sample is commonly obtained by the hysteresis loop. This curve is a measure of the amount of magnetization induced as a function of a known magnetic field (M vs. H), giving information about the magnetic behavior, coercivity, remanence and saturation in the material. It is also important to measure the susceptibility that is associated with both magnetization and magnetic field. In this section, we describe two important techniques used in this study.

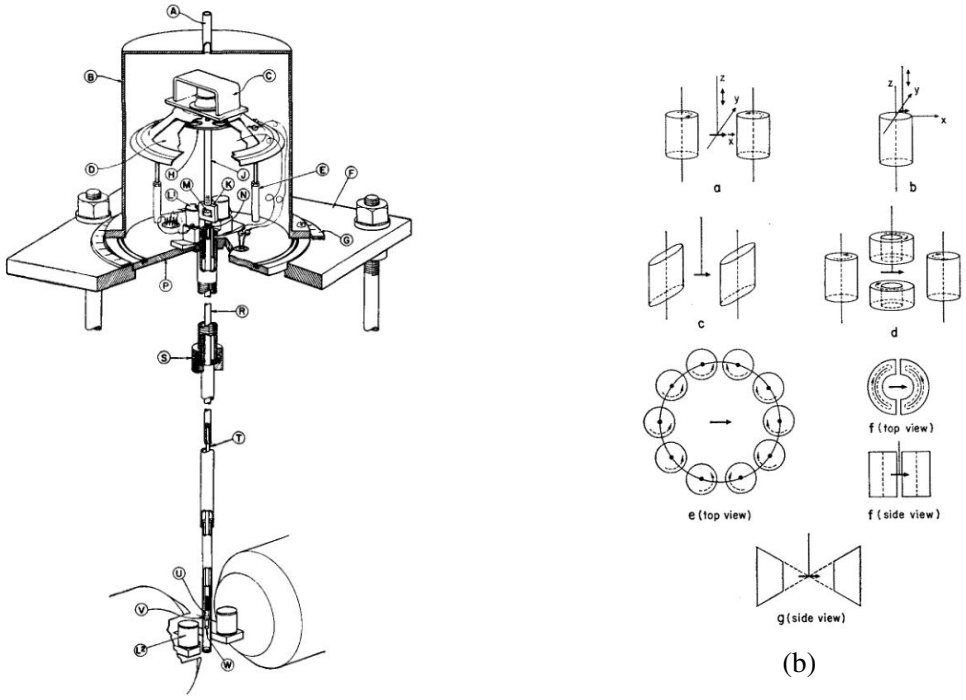

(a) (b)

Figure 4.3: a) Detailed mechanical construction and b) pick-up coils arragements for a VSM built by Forner [64].

4.2.2.1 Vibrating sample magnetometer

The usual methods of measuring magnetic moments are made in three ways: i) inductive methods, ii) as a measure of force or displacement under a magnetic field gradient or iii) through the variation of an intrinsic property of the material, as Hall effect, magnetoresistance, magneto-optics, etc. [64, 65]. All the magnetic induction measurements involve observation of the voltage induced in a detection coil by a flux change when the applied magnetic field, coil position, or sample position is changed. Between them, we have the vibrating sample magnetometer (VSM) pioneered by S. Forner in 1959 [64]. This simple but yet effective technique for characterizing properties of magnetic materials is widely used in both basic research laboratories and production environments for its good performance, low price, and simplicity of operation. Based on Faraday's law of induction, the VSM relies on the detection of the electromotive force (emf) or voltage induced in a coil of wire given by the eq. 4.6. N is the number of wire turns in the coil, A is the coil turn area, and θ is the angle between the B field and the direction normal to the coil surface. In practice, knowledge of coil parameters such as N and A is unnecessary if the system can be calibrated with a known sample [66].

$$\varepsilon = V(t) = -N\frac{d}{dt}\left(BA\cos\theta\right). \tag{4.6}$$

The operation of the VSM is quite simple. The basic configuration is shown in Fig. 4.3a, a magnetic sample mount in a rigid rod which vibrates sinusoidally as a function of frequency between the poles of an electromagnet in a known magnetic field applied in a transversal or longitudinal configuration. This movement generates an induced change in voltage acquired by the pick-up coils. The induced voltage is proportional to the sample's magnetization.

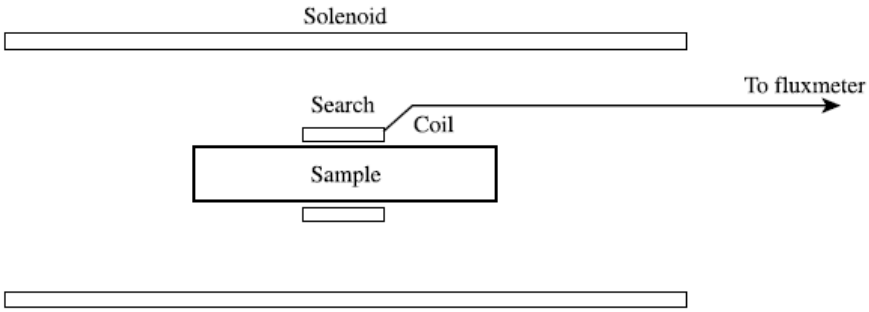

Figure 4.4: Extraction magnetometer description [14]

4.2.2.2 Extraction magnetometry

This method is based on the measurement of a flux change in a search coil when the specimen positioned at the center of a coil inside an external magnetic field is quickly removed (extracted) from the coil to a larger distance from the field (See Fig. 4.4). It can also be found in a configuration where the specimen and search coil together are extracted [9, 14]. According to Faraday's law the resulting change of flux in a coil can be linked to the induced emf, then the magnetic moment of the sample is proportional to the change of flux registered, Eq. 3.7. Where N_d is the demagnetization factor[1], A the specimen area and M the induced over the sample.

$$\Phi_2 - \Phi_1 = \mu_0(1 - N_d)MA. \tag{4.7}$$

A variation of this method involves two identical search coils, located symmetrically in the solenoid. These are connected in "series opposition", i.e., if one is wound clockwise, viewed along their common axis, the other is wound counterclockwise, so changes of applied field do

[1] or demagnetizing coefficient is a mainly a geometrical (shape) dependent factor caused by the presence of demagnetizing field induced in a sample

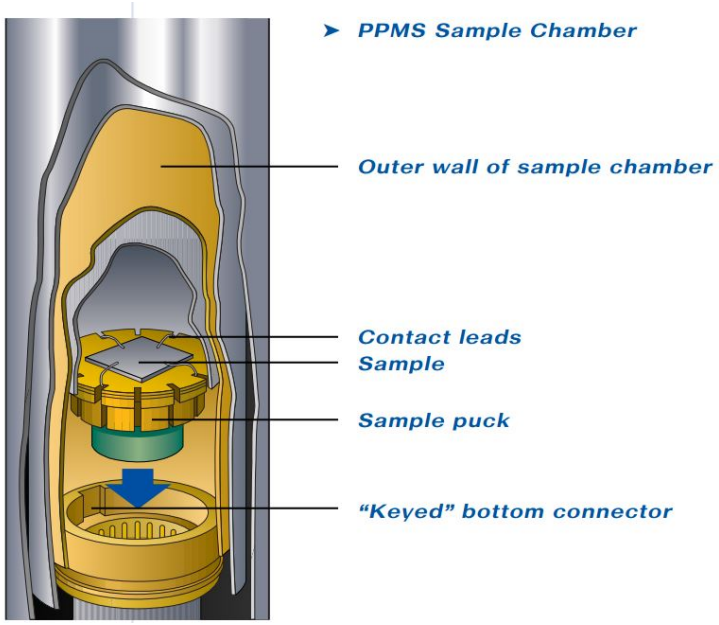

Figure 4.5: Detailed PPMS chamber and connector [67]

not register [36, 14].

Due to its versatility, this principle is widely used in equipment such as the SQUID magnetometer and the Physical properties magnetic system or better known as PPMS. The quantum design PPMS represents a unique concept in laboratory equipment. It is an open architecture, variable temperature-field system that is optimized to perform a variety of automated measurements. It works like a dedicated system, but its tremendous flexibility allows different types of measurements such as magnetometry, electro-transport, microscopy, thermal measurements, etc. [67].

Another interesting and unique feature is the sample-mounting system, Fig. 4.5. At the bottom of the sample chamber is a 12-pin connector pre-wired to the system electronics. [67]. The equipment can be configured to reach a $\pm$ 85 kOe magnetic field in a temperature range from 2 K to 350 K controlled using helium gas that is drawn into the annular region where heaters warm the gas to the correct temperature. This design reduces thermal gradients and increases system flexibility by making the sample chamber a controllable environment. For example, the sealed sample chamber may hold a high vacuum without the need for additional inserts.

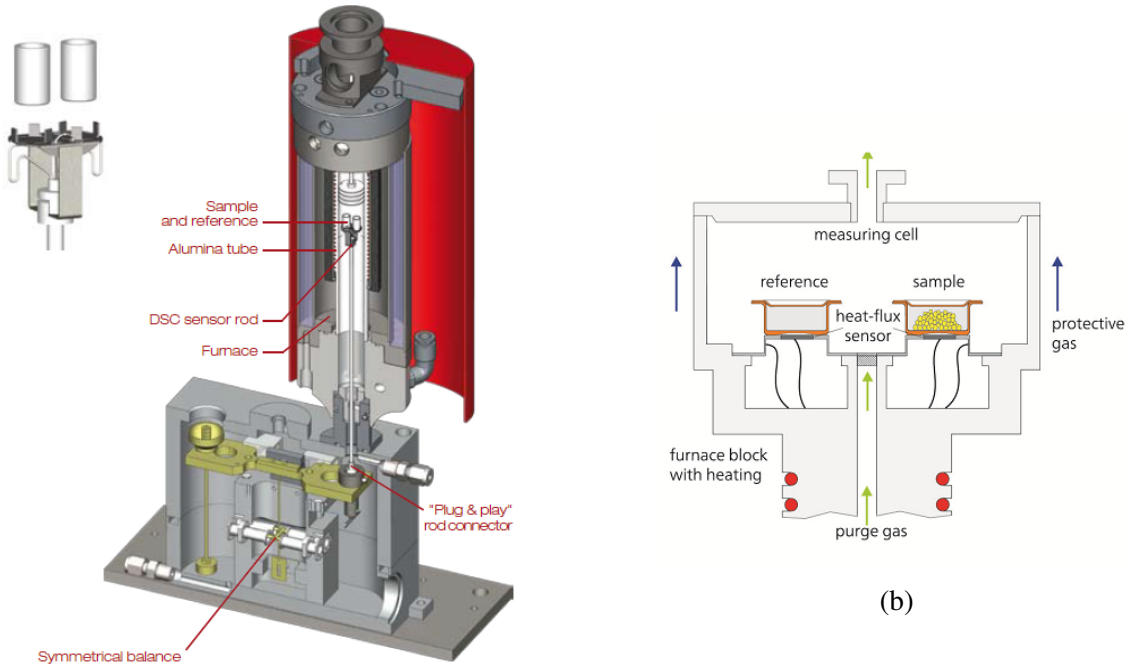

(a) (b)

Figure 4.6: (a) LabSys TG-DSC equipment with a description of the rod used [69]; (b) Heat flux configuration for DSC [70]

4.2.3 Thermal analysis

Thermal analysis (TA) is a group of physical or chemical methods, which deal with studying materials and processes under specific conditions while the temperature of the sample is programmed and controlled. Another definition given by the ICTAC (International Confederation for Thermal Analysis and Calorimetry), is that TA is the study of the relationship between a sample property and its temperature as the sample is heated or cooled in a controlled manner [68]. In the true sense, the thermal analysis covers all the phenomena that register the variations of a certain physical property or quantity as function of the temperature. In some techniques as calorimetry, dilatometry and thermoporometry the influence of temperature on the sample are directly recorded. However, methods such as thermogravimetry, sorptometry and hygrometry are often complementary: gas release or uptake as a function of temperature and gas pressure.

The thermal measurements were carried out in a LabSys Evo by SETARAM (Fig. 4.6a) equipped with different roads and crucibles which allow us to make the different measurements described below in this section.

4.2.3.1 Thermogravimetry (TGA)

Thermogravimetric analysis is a technique in which the mass of a substance is monitored as a function of temperature or time as the sample specimen is subjected to a controlled temperature program in a controlled atmosphere. A certain mass is lost or gained if the substance contains a volatile fraction, thus, this weight curve gives information on changes in sample composition, thermal stability and kinetic parameters for chemical reactions in the sample. In this technique, a known amount of material (in our case, powder sample) is poured into a container positioned at the end of a fine rod, and then the rod is carefully coupled inside the equipment and starts to heat up. A precise balance in top loading configuration, register the weight variations during the process (see Fig. 4.6a).

4.2.3.2 Differential Scanning Calorimetry (DSC)

DSC is a thermal analysis technique that looks at how a material's heat capacity changes with temperature. A sample of known mass is heated and the modifications in its heat capacity are track down as changes in the heat flow.

$$\dot{q} = E(t)\Delta T \tag{4.8}$$

There are two basic types of DSC configurations: heat-flux and power compensation, nevertheless our discussion is focus only on the first one. In the heat flux mode, the instrument evaluates the difference between the heat-flow rates into a sample and a reference material. The sample material, enclosed in a pan and an empty reference pan are placed on a thermoelectric disk surrounded by a furnace. The furnace is heated at a linear heating rate, and the heat is transferred to the sample and reference pan through the thermoelectric disk (Fig. 4.6). Within the instrument the difference in temperature signal (ΔT) is converted to a heat flow rate using a temperature dependent factor (eq. 4.8), the proportional factor E(t) depends on geometry and materials of construction of the differential temperature sensor [71].

4.2.4 Microscopy and optical based characterization

4.2.4.1 Electron microscopy

In 1896, Lord Rayleigh gave an estimate of the minimal resolvable distance between two equally bright light sources that are imaged in a diffraction-limited system [72]. This classic concept known as Rayleigh criterion for visual light microscopy states that the smallest distance that can be resolved, δ, depends on the wavelength of the radiation and also of the semi-angle of collection of the magnifying lens (β) (eq 4.9). Therefore, for optical microscopy, the resolution is limited by the wavelength of light (410-660 nm).

$$\delta = \frac{0.61\lambda}{\sin\beta}. \tag{4.9}$$

Louis de Broglie (1925) first theorized that the electron had wave-like characteristics, with a wavelength substantially less than visible light, the subsequent experimental research carried out around this notion allowed the invention of electron microscopes devices in early 1930's. There are two varieties of electron microscopes: transmission electron microscope (TEM) and scanning electron microscope (SEM), who had the same basic configuration consisting in the ability to generate an electron beam, and then to deflect and focus such a beam with the use of electrostatic and magnetic coils or lenses which resembles to a cathode ray tube.

4.2.4.2 Transmission electron microscopy (TEM)

This term was first used for Knoll and Ruska in 1932 when they developed the idea of electron lenses into a practical reality and demonstrated electron images could be obtained with a magnification of 13x. Within a year of Knoll and Ruska's publication, the resolution limit of the light microscope was surpassed. Ruska, surprisingly, revealed that he had not heard of de Broglie's ideas about electron waves and thought that the wavelength limit did not apply to electrons [73]. In the TEM, a beam of electrons is incident on an ultra-thin specimen. Some of the electrons are absorbed, some are scattered and some are transmitted. The basic design consists of a source of electrons (electron gun) followed by a condenser lens that focuses the electron beam onto the specimen located in the specimen plane. An objective lens and two projector lenses focus the transmitted electron beam onto a fluorescent screen, and the observer or a charge-coupled device (CCD) camera records the image. For TEM observations, thin samples are required due

to the important absorption of the electrons in the material Fig. 4.7.

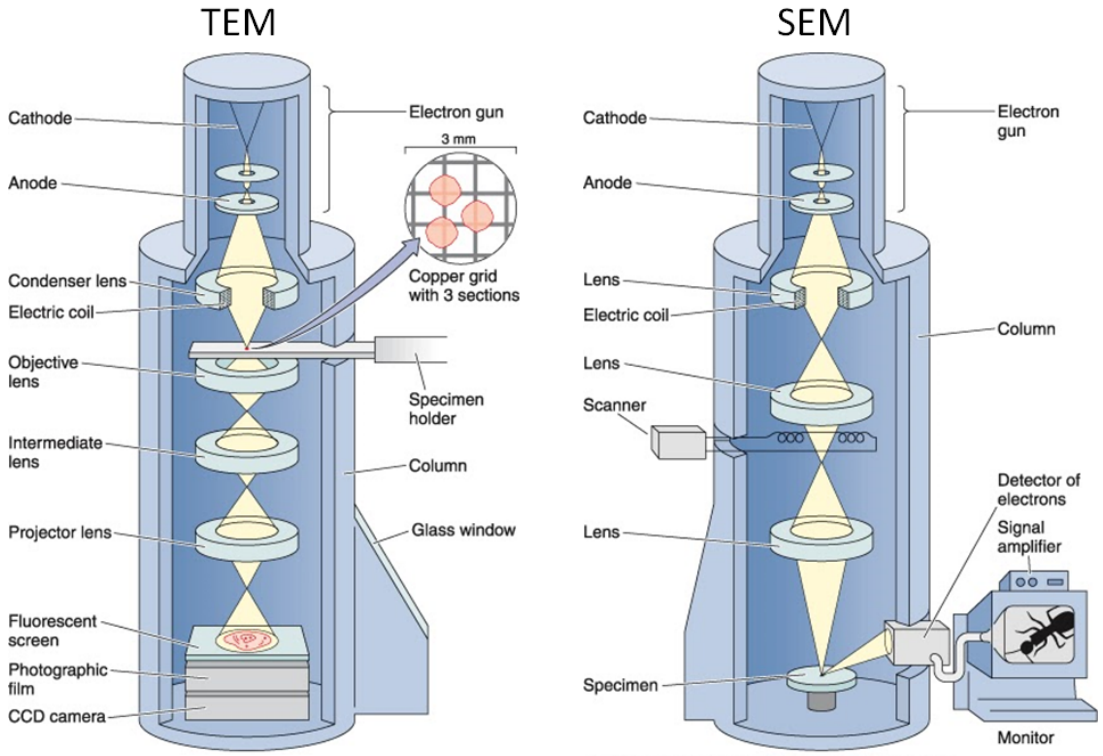

Figure 4.7: TEM and SEM detailed configurations [74]

4.2.4.3 Scanning electron microscopy (SEM)

Scanning electron microscopy (SEM) is one of the most versatile instruments available to observe and analyze the microstructural characteristics of solid materials. In 1938 von Ardenne made theoretical and instrumental developments to build the first SEM adapting scanning coils of a transmission electron microscopy (TEM) developed early by Knoll and Ruska (1935) [75]. Although, the first true SEM was described and developed in 1942 by Zworykin, who showed that secondary electrons provided topographic contrast by biasing the collector positively relative to the specimen [76]. In SEM, a fine probe of electrons is focused on a specimen and scanned along a pattern of parallel lines. The beam is typically produced by an electron gun, which consist of an incandescent tungsten filament (cathode) with energies up to 40 keV, processed by magnetic lenses (two condensers and one objective lens), focused at the specimen surface (that serves as the anode) and systematically scanned (raster) across the surface of a specimen (see fig. 4.7). Various signals are generated as a result of the impact of the incident electrons, which are collected to form an image or to analyze the sample surface. These are

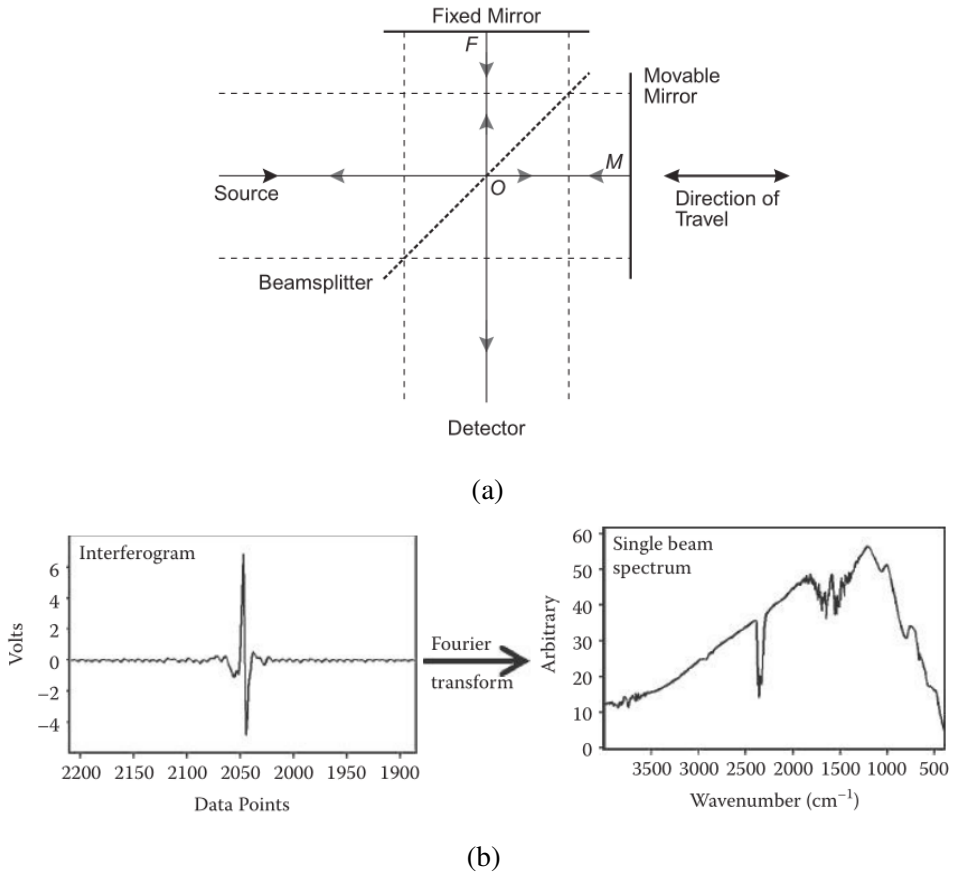

Figure 4.8: (a) Michelson interferometer [77] and (b) Fourier transform interferogram [78]

mainly secondary electrons, with energies of a few tens of eV, high-energy electrons backscattered from the primary beam, auger electrons, and characteristic X-rays [76]. There is a physical relationship between the wavelength of characteristic X-rays emitted from an element and its atomic number Z. *Energy Dispersive X-ray Spectroscopy* (EDS) detector is an additional attachment coupled to the SEM system that collects and quantifies this kind of radiation produced during the reaction between the beam and sample to determine the element composition present in the specimen.

4.2.5 Fourier Transform Infrared (FTIR) spectroscopy

The discovery that radiation existed outside the visible spectral region was made by Sir William Herschel in the spring of the year 1800. In order to facilitate his studies of sunspots, he was seeking some filtering technique which would give adequate light for seeing, without undesirable heating [79]. Using an experimental setup consisted of a prism to split the beams of light and thermometer to see the changes in temperature, he found that the temperature increased as

he went from the violet to the red, attributing this changes in radiation to an "invisible light". Nowadays, we can find several uses for this discovery, one of them is *infrared spectroscopy*. FTIR consist in the interaction of infrared light with a sample, some of the radiation will be absorbed and other proportion passes through (transmitted), where the resulting spectrum represents the molecular absorption and transmission, creating a molecular fingerprint of the sample. One of the most important components of FTIR is the interferometer. The design of many interferometers used today is based on that of the two-beam interferometer originally designed by Michelson in 1891 [77]. The Michelson interferometer (MI) is a device that can divide a beam of radiation into two paths and then recombine the two beams after a path difference has been introduced. The resulting signal is called an interferogram. The resulting interferogram has to be analyzed in terms of frequency, hence, we need to find the proper tool to do so. This can be accomplished via a well-known mathematical technique called the Fourier transformation, thus, when an interferogram is Fourier transformed it produces a single beam spectrum (Fig. 4.8b) [78]. This transformation leads to a graphic in terms of wavenumber ($\nu = 1/\lambda$), that is proportional to the energy of a light wave (Eq. 4.10). Since energy is proportional to ν, high wavenumber light has more energy than low wavenumber light. In general, wavenumber is given in cm^{-1}.

$$E = \frac{hc}{\lambda} = hc\nu \tag{4.10}$$

5

Synthesis of iron doped europium orthochromites

In this chapter, we discuss the synthesis process used to prepared pure and doped with iron europium chromites by combustion reaction process. As we have said before, one of the advantages of using, combustion is its efficiency in time and low cost. The whole set of samples was prepared using the laboratory facilities at the Institute of Physics (Instituto de Física-IF) at the Universidade Federal de Goiás.

Figure 5.1: Hot blanket used in the synthesis and ceramic capsule with urea

In the standard route used, the reactants (stoichiometrically combined) were hand mixed in a ceramics recipient with *urea* as fuel and dissolved in deionizated water (10 to 30 mL) to obtain a homogenized solution. Then this mixture was heated up around 400 °C on a hot blanket inside a fume cupboard (see Fig. 5.1) under air ventilation until reach the combustion reaction. The properties of the reactants are shown in the Table 5.1. Using the considerations proposed by Jain *et al* [55] and according to the thermochemical concepts of propellant chemistry, elements such as H, C, Eu and Fe are considered as reducing elements, O is considered as an oxidizing element and N has a neutral valency. Thus the corresponding valency values for each element

are: Eu = +3, N = neutral= 0, H = +1, O = -2, Cr = +3, Fe = +3 and C = +4, in order to find the correct fuel/oxidant ratio in the reaction.

Table 5.1: Properties of the reactants used in the synthesis process

Chemical Formula	Name	Molecular weight	Brand
$Eu(NO_3)_3 \cdot 5H_2O$	Europium(III) nitrate pentahydrate	428.06	Sigma-Aldrich
$Fe(NO_3)_3 \cdot 9H_2O$	Iron(III) nitrate nonahydrate	404.00	Sigma-Aldrich
$Cr(NO_3)_3 \cdot 9H_2O$	Chromium(III) nitrate nonahydrate	400.15	Sigma-Aldrich
$CO(NH_2)_2$	*Urea*	60.06	Sigma-Aldrich

Table 5.2: $Eu_{1-x}Fe_xCrO_3$ calculated mass of the reactants for different x values

x (mol)	$Eu(NO_3)_3 \cdot 5H_2O$	$Fe(NO_3)_3 \cdot 9H_2O$	$Cr(NO_3)_3 \cdot 9H_2O$	$CO(NH_2)_2$
0.00	2.1403	0.0000	2.0008	4.5045
0.10	1.9263	0.2020	2.0008	4.5045
0.20	1.7122	0.4040	2.0008	4.5045
0.30	1.4982	0.6060	2.0008	4.5045
0.40	1.2842	0.8080	2.0008	4.5045
0.50	1.0702	1.0100	2.0008	4.5045
0.60	0.8561	1.2120	2.0008	4.5045
0.70	0.6421	1.4140	2.0008	4.5045
0.80	0.4281	1.6160	2.0008	4.5045
0.90	0.2140	1.8180	2.0008	4.5045
1.00	0.0000	2.0200	2.0008	4.5045

5.1 $EuCrO_3$ doped with Fe

First we need to find the total valencies for each component in the mixture, then for $Eu(NO_3)_3 \cdot 5H_2O$ adds up to -15, for $Fe(NO_3)_3 \cdot 9H_2O$ adds up to -15, for $Cr(NO_3)_3 \cdot 9H_2O$ is -15 and finally *urea* is +6, so the molar weight for fuel in the stoichiometrically compound $Eu_{1-x}Fe_xCrO_3$ is:

$$\begin{aligned} -15(1-x) - 15x - 15 + 6n &= 0 \\ -15 - 15 + 15x - 15x + 6n &= 0 \\ n &= 5\,mol. \end{aligned}$$

Independent of the value of x the fuel weight is always the same. Using an excess of 200% in urea was calculated the mass of different samples varying x in the composition, the necessity of adding an excess of fuel is due to heat loss with the large amount of gases released by the reaction, as well as *urea* being the fuel, which releases the lowest amount of gas. The values are shown in Table 5.2, with $0.0 \leq x \leq 1.0$ and are referred in grams (g).

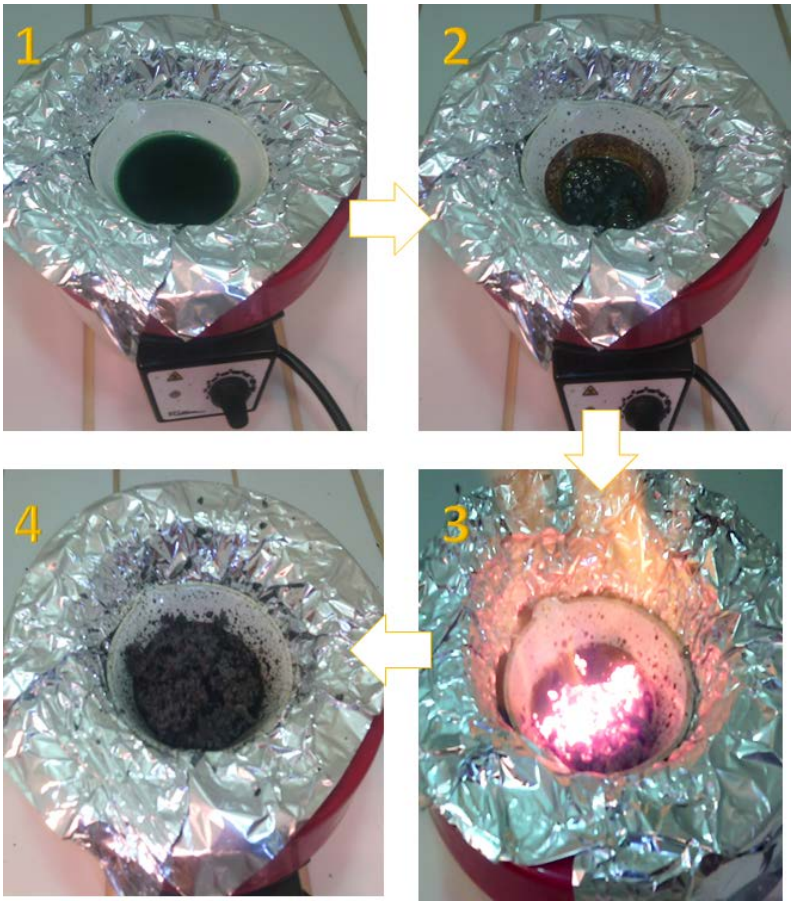

Figure 5.2: Stages for the combustion reaction during the synthesis of $Eu_{1-x}Fe_xCrO_3$

Samples between $0.0 \leq x \leq 1.0$, were synthesized. The reaction was carried out in a pre-heated (20 minutes before placing the ceramic container) hot blanket. With a rise in temperature, the aqueous mixed begin to evaporated changing from a green color to a darker one and expelling gases in the process as it can be seen in Fig. 5.2 (1 and 2). Soon after this, the thickened liquid began to frothing, ignition took place in a non-centered focal point and then propagated through the surface of the capsule liberating a considerable amount of gases into the chamber (Fig. 5.2 section 3). The whole reaction took between 20 to 30 minutes, with the flame only lasting for a few seconds and producing a dry, very fragile foam which transformed into powder at the slightest touch (Fig. 5.2 section 4) as reported by Franco Júnior *et al* [80]. As the concentration of Fe increases the powder changes from a green color for pure $EuCrO_3$

to a dark black in the $FeCrO_3$ chromite as seen in Fig. 5.3. Also, the addition of iron modifies the combustion process, for high contents of europium the reaction is highly reactive. For high content of Fe, on the other hand, the ignition occur in a more controlled way.

Figure 5.3: Evolution in color for pure chromites of Eu and Fe

6

Results and discussion: $EuCrO_3$

In this chapter, we present the results and analysis obtained from the different characterization techniques used to study the rare earth europium chromites synthesized by combustion reaction. In the first half, we introduce the highlights of our research about the synthesis of pure $EuCrO_3$. Later we explore the evolution of iron doping on the as prepared and thermally treated samples, in a systematically attempt to understand how the different properties of these chromites can be modified by the substitution of ions.

6.1 Pure europium orthochromites

6.1.1 Structural and morphological analysis

X-ray diffractograms obtained at room temperature were analyzed using the Rietveld refinement method with the help of MAUD software [63]. Fig. 6.1a shows the refined spectra for $EuCrO_3$, where the dotted line represents the experimental data (I_{obs}), the red line stands for the fitted data (I_{calc}) and the blue one exhibits the difference between them (I_{obs} - I_{cal}). The

Table 6.1: Comparison of lattice parameters for $EuCrO_3$ orthochromites.

Lattice parameter	Ours	Reference [1]	Reference [2]	Reference [5]
a (nm)	0.553(2)	0.552	0.550	0.554
b (nm)	0.764(2)	0.762	0.763	0.762
c (nm)	0.535(2)	0.534	0.535	0.525

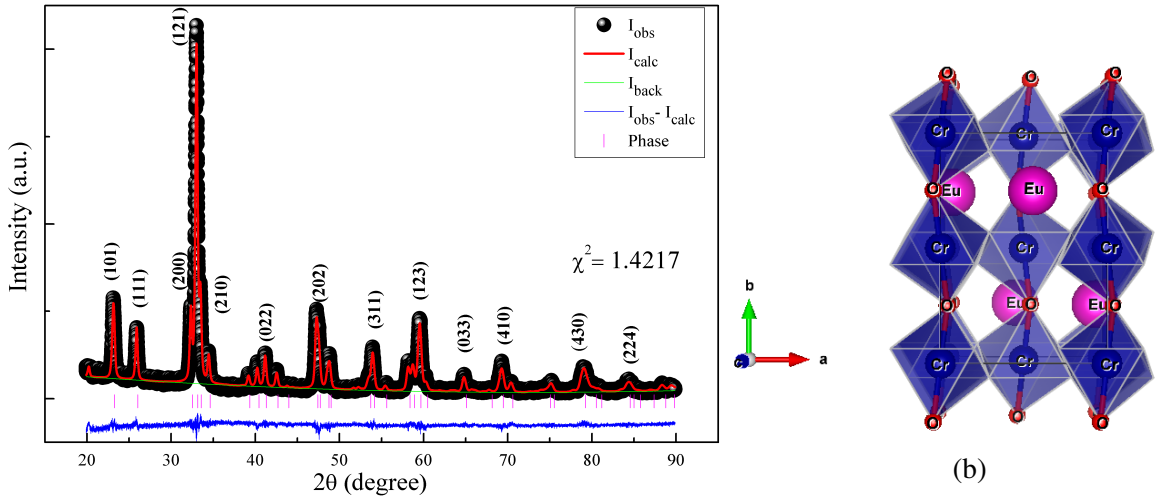

(a) (b)

Figure 6.1: (a) Refined X-ray diffraction pattern of the as-cast $EuCrO_3$ ortochromite and (b) Crystal structure of $EuCrO_3$ along *c*-axis.

diffraction pattern presents well defined and intense peaks, which are in good agreement with the JCPDS PDF #251053 (magenta line) data for an orthorhombic perovskite structure, space group *Pnma* (number 62), without the presence of extra reflection peaks, ensuring a pure single phase $EuCrO_3$. The lattice parameters obtained from the Rietveld analysis are close to those reported, as shown in Tab. 6.1 presents, with a calculated average crystallite size of ≈ 66 nm.

Table 6.2: Refined parameters for $EuCrO_3$ obtained by combustion reaction synthesis

Ion	Wyckoff's position	x/a	y/a	z/c	Occupancy
Eu1	4c	0.4450	0.2500	0.0157	1.0000
Cr1	4a	0.0000	0.0000	0.0000	1.0000
O1	8d	0.2097	0.0703	0.2734	1.0000
O2	4c	0.5402	0.2500	0.5624	1.0000
Volume (Å^3)			225.98		
Density (g/cm^3)			7.4058		
χ^2			1.4217		
Rp (%)			7.2069		
Rwp (%)			9.7273		
Micro-strain (%)			0.16		

The corresponding crystallographic information file (cif) derived from the XRD Rietveld refinement was schematized using VESTA software [81] and is presented in Fig. 6.1b, where the cationic order in Wyckoff notation of the crystallographic A- and B- sites is shown in table 6.2. The blue spheres represent Cr^{3+} ions, red ones O^{2-} and the magenta Eu^{3+}. The interplanar distortion observed along the *c*-axis, is responsible for the alignment of the Cr^{3+} moments

for an easy magnetization direction [5]. Hence, we have calculated a Cr^{3+}-O^{2-}-Cr^{3+} bond angle of 156.3° which compared to the standard crystallographic information file for europium chromite has a relative increase of 6% [1]. It is obvious then that the structural results prove our previous hypothesis that the synthesis of single phase $EuCrO_3$ by combustion reaction proves to be adequate and improves notably parameters such as time of synthesis, temperature and calcination steps, when compared to other methods [1, 2, 3, 4].

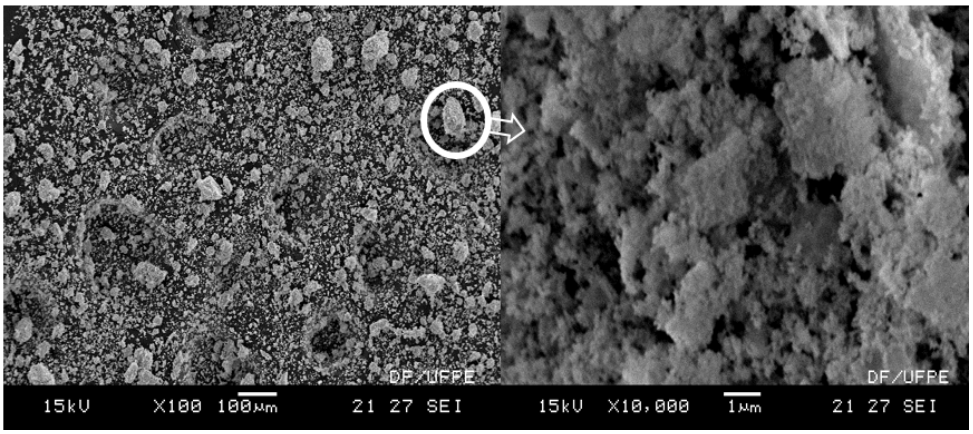

(a)

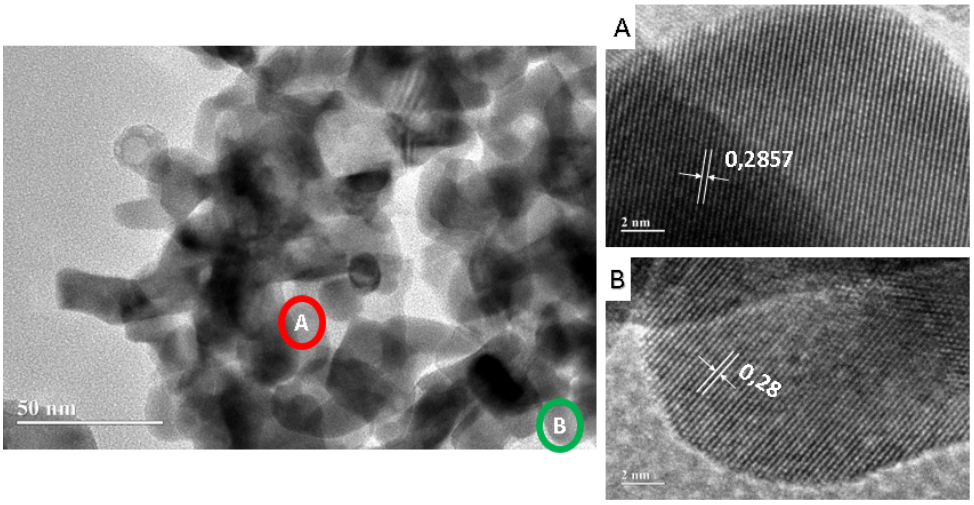

(b)

Figure 6.2: (a) SEM and (b) TEM images of $EuCrO_3$ nanoparticles synthesized by combustion reaction method.

The combustion reaction process has a particularity, we do not have any control over it once the ignition starts, so there is not control in parameters such as final grain or particle size of the system. SEM micrographs of the as-synthesized $EuCrO_3$ reveal that the powders have nanometric sizes, in agreement with XRD. However, as expected, there is a random distribution of particle size along the sample (Fig. 6.2a). A complete approach to determine crystallite sizes and morphology have been made using transmission electron microscopy (TEM) images of the

as cast europium chromites, as can be seen in Fig. 6.2b. The morphology of the particles is not uniform, although a reasonable tendency to generally form oblated or spherical grains can be perceived which are in agreement with previous works [82]. High resolution transmission electron microscopy (HRTEM) images (Fig 6.2b (a) and (b)) revealed that the average interplanar distance is about 0.28 nm with particle grains below 50 nm.

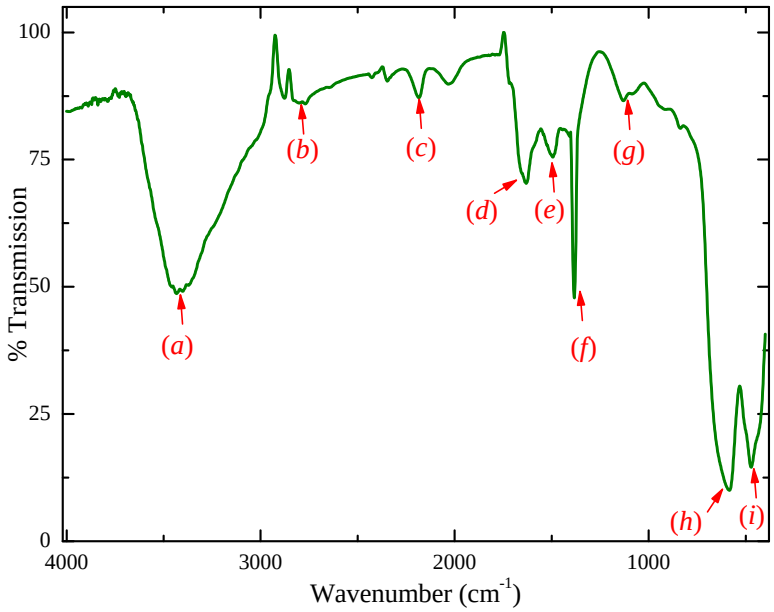

Figure 6.3: FTIR spectra of europium orthochromite

6.1.2 FTIR analysis

There are only a few studies made with infrared spectroscopy analysis on rare earth chromites, and no of them (that we are aware of) have been made in the $EuCrO_3$ system. For the FTIR studies, we mixed the samples with KBr and the measurements were done at room temperature using a range between 4000 cm^{-1} to 400 cm^{-1} in a Shimadzu IRTracer-100 equipment, which offers high sensitivity with a 60,000:1 S/N ratio. In Fig. 6.3, we show the FTIR spectroscopy data for the $EuCrO_3$ nanoparticles. Each broad absorption band displayed was labeled from (a) to (i). The very notorious and broad peak (*a*) around 3400 cm^{-1} corresponds to the normal polymeric O–H stretching vibration which is assigned to chemisorbed and/or physisorbed water molecules trapped in the system. The absorption band (b) near 2800 cm^{-1} is attributed to C–H, C–C and C–N bonding. Around $\sim$ 2177 cm^{-1} peak (c) is assigned to the CO_2 molecules in the air. About 1450-1700 cm^{-1} there are two broad peaks (d) and (e), with the first one to H–O–H

bending vibrating, which is assigned to a small amount of H_2O in the sample with the other one may be associated to Cr-O [83]. A sharp peak around $\sim$1250 cm^{-1} (f) in addition with several low-intensity peaks between 800-1122 cm^{-1} (g) corresponds to NO^{3-} of unreacted precursor salts and N–H stretching [84].

Heavy elements mostly exhibit stretching bands at low wavenumbers. In fact, peaks (h) and (i) around 473-584 cm^{-1} can be attributed to the stretching of Eu–O bond [85, 86]. Metal oxide Cr_2O_3 generally reveal absorption bands below 1000 cm^{-1} (600 to 540 cm^{-1}) due to inter-atomic vibrations [83] but in our case they are not visible, which is expected due to the single phase $EuCrO_3$ achieved in the synthesis.

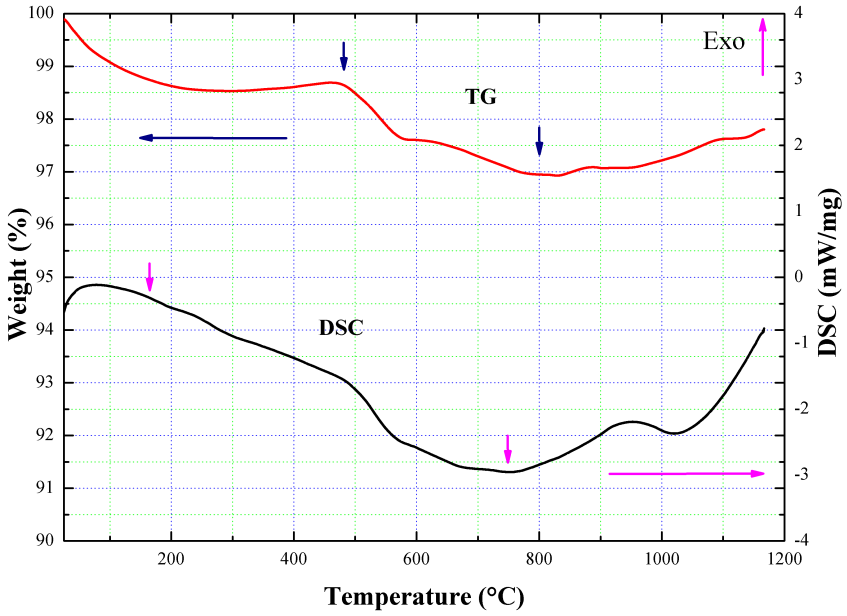

Figure 6.4: $EuCrO_3$ TG-DSC measurement

6.1.3 Thermal analysis

Thermal analysis was carried out using a platinum crucible in O_2 atmosphere. The furnace temperature was increased from room temperature to 1200°C at 10°C/min rate and cooled down in the same way. $EuCrO_3$ TG results exhibit a maximum weight loss through the process of nearly 3%, Fig. 6.4. Starting from room temperature up to 200°C, there is an initial decay in the plot due to the presence of water trapped in the sample, which is being evaporated. Two pronounced peaks are found around 480°C and 620°C, with a greater weight loss for their first one. DSC analysis corroborates the presence of water for low temperatures. Afterward,

the reaction is principally endothermic, meaning that most of the exothermic reactions in the system happened during the combustion process. From both TG-DSC data, we can visualize mild oxidation process starting after 800°C, evidenced by a little gain in weight. Nevertheless, in general terms, the reaction was quite stable.

6.1.4 Magnetic analysis

Magnetic measurements were made at room and low temperatures for the single phase $EuCrO_3$. Fig. 6.5 shows an M vs H curve measured at room temperature in a vibrating sample magnetometer up to an external field of 20 kOe for the as-prepared $EuCrO_3$. The powders were prepared using a straw holder which is glued to a glass rod using Teflon, avoiding as possible any magnetic material that can affect the measurement. As expected, above the Néel temperature, the rare earth chromites have a predominant paramagnetic behavior [4, 82, 87]. The maximum value for magnetization at the maximum applied field ($M(H_{max})$ has a value of 0.33 emu/g and a low susceptibility value was calculated being close to approximately 1.96×10^{-5} emu/g Oe.

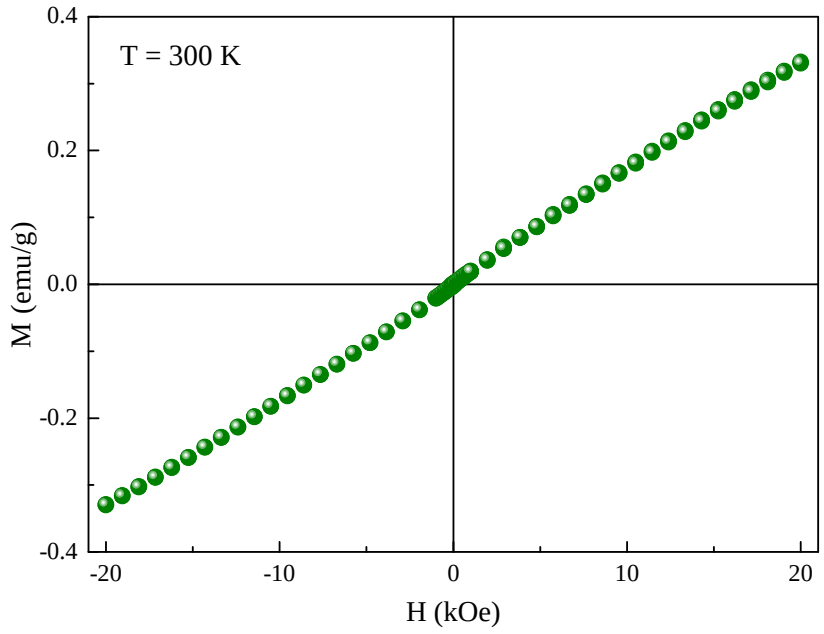

Figure 6.5: M vs H curve at room temperature for $EuCrO_3$

The temperature dependence for the zero field cooling (ZFC) and for the field cooling (FC) magnetizations measured with an applied field of $H = 100$ Oe for samples of $EuCrO_3$ are shown in Fig. 6.6. These measurements were taken between 5-300 K in a PPMS, in the ACMS mode.

There is a clear difference among the curves that is related to the weak ferromagnetic behavior typical of this system. The net magnetic moment has been attributed to the observed small canting angle of the otherwise antiferromagnetic Cr^{3+} (S=3/2) spin magnetic moment followed by the tilting of two adjacent CrO_6 corner-sharing octahedra, with a Cr-O-Cr bond angle of ≈ 152°. This value of angle is far from the ideal 180° in distorted orthorhombic perovskite-like material [3, 88]. At low-temperature the magnetic properties are dominated only by Cr^{3+} spins because the RE^{3+}-RE^{3+} sublattice orders at very low temperatures T_N (≈ 2 - 15 K) and only for certain ions [3].

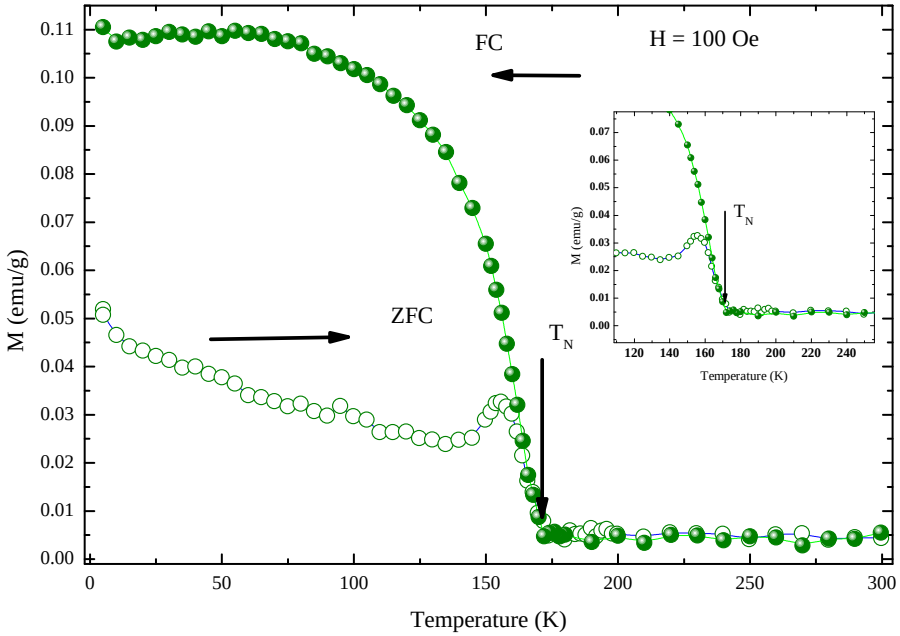

Figure 6.6: ZFC (open ○) and FC (filled ●) magnetization as function of temperature curves for $EuCrO_3$ with an applied field of $H = 100$ Oe

$$C = \frac{N_A P^2 \mu_B^2}{3k_B} \tag{6.1}$$

The inset in Fig. 6.6 the Néel temperature determined for the pure $EuCrO_3$. We have found a value of $T_N \approx 172$ K which is lower than the 181 K reported by several references [1, 4, 82]. The reduction in the value of T_N can be accounted for by the stress induced during the synthesis. In the high-temperature region (above T_N) the paramagnetic state follows the Curie-Weiss law (see Eq. 3.12). So, a linear fit can be made to show the dependence of T with the reciprocal magnetic susceptibility χ^{-1}. The best fit corresponds to a Weiss temperature of Θ = -249 K. The negative value is typical of antiferromagnetic interactions, which is consisted with the CAFM behavior

reported for this the rare earth chromite. Using Eq. 6.1 (where N_A is the Avogadro constant, k_B is the Boltzmann constant, C is the Curie constant, μ_B and P are the Bohr magneton and its effective number, respectively) a value of the effective magnetic moment has been calculated, with $P\mu_B = 6.97\mu_B$. This value is higher than the calculated ($P\mu_{theo} = 5.15\mu_B$) by using the free ion values $3.4\mu_B$ for Eu^{3+} and $3.87\mu_B$ for Cr^{3+} but is close to 6.62 μ_B value reported for a sample of $EuCrO_3$ sample prepared by a different method [4]. The value of Θ depends on the total number of neighbors in each neighbor shell and it is independent of the magnetic ordering in a given crystal. The ratio between $|\Theta|/T_N$ is equal to 1.45 (>1) which differ from the expected unity value (1), indicating that the next-nearest-neighbor interactions and sublattice arrangements should be considered, been crucial to understanding the magnetic environment of an arrangement of magnetic ions [8, 88]. Then, in general terms we can conclude from the different properties found in powder samples of $EuCrO_3$ that the combustion reaction process is an ideal technique to produce nanoparticles of high quality and within the parameters expected for such system. Furthermore, our synthesis process has the advantage of being faster, easier and cheaper method than those reported.

6.2 Iron doped orthochromites ($Eu_{1-x}Fe_xCrO_3$): As prepared

A comparative study of the structural, magnetic, and thermal properties of europium chromites doped with iron ($Eu_{1-x}Fe_xCrO_3$) is presented in this chapter. Powder samples were synthesized by the combustion reaction process using urea as fuel and the reactants were combined stoichiometrically based on the total oxidizing and reducing valences, according to the concepts from propellant chemistry presented on chapter 5.

6.2.1 Structural and morphological analysis

As a first approach to understanding the effect of iron inclusion in the orthorhombic perovskite structure, samples with high concentration of iron (x = 0.0, 0.2, 0.5, 0.6, 0.8 and 1.0) were prepared using the atomic concentrations introduced in Tab. 5.2. As for the pure $EuCrO_3$, Rietveld analysis of the XRD patterns at room temperature for $Eu_{1-x}Fe_xCrO_3$ nanopowders showed that the system belongs to a Pnma structure (space group 62) as well. The evolution of

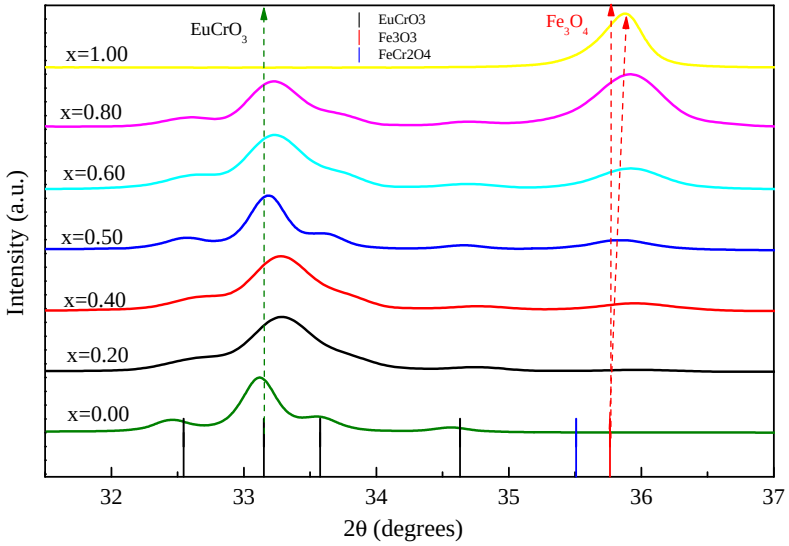

(a)

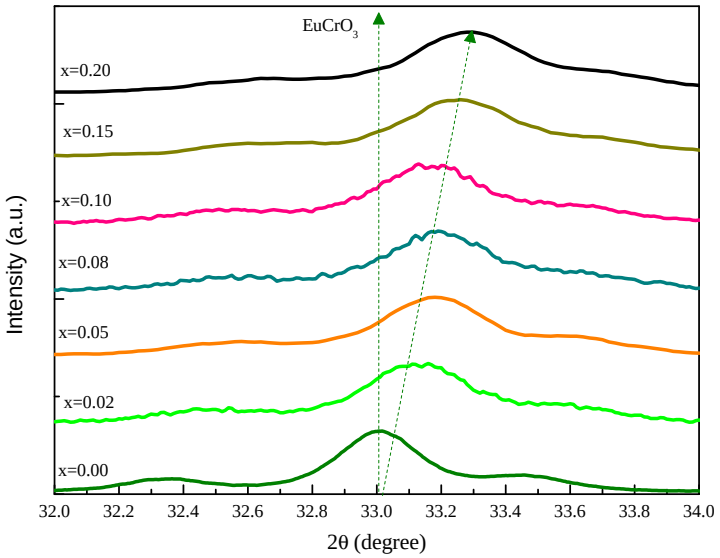

(b)

Figure 6.7: (a) Detailed peak evolution as function of iron content for (a) high concentrations ($0.0 \leq x \leq 1.0$) and (b) low concentrations ($0.0 \leq x \leq 0.2$) for the $Eu_{1-x}Fe_xCrO_3$

the main diffraction peak as a function of iron content is shown in Fig. 6.7a. The diffraction peak around 33.2° corresponding to the $EuCrO_3$ pure phase shifts to left when the iron concentration is increased. Moreover, above 20% of iron, a peak due to a secondary phase starts to appear close to 36°. According to our analysis, iron ions enter substitutionally replacing the europium ones positioned in the A site of the perovskite structure. This ion replacement produces a strain in the system due to the mismatch in ionic atomic radii ($Eu^{3+} = 120.6$ pm and $Fe^{3+} = 92$ pm, both in eight coordination). Then, we can infer that there is a limit in dissolution of iron for $x \leq 20\%$ which can enter to the system and form the single phase $Eu_{1-x}Fe_xCrO_3$ perovskites.

Afterwards, we have identified the secondary phase to be magnetite (Fe_3O_4).

Table 6.3: Phase concentration for iron doped chromites

x (mol)	$Eu_{(1-x)}Fe_xCrO_3$ (%)	Fe_3O_4 (%)	$FeCr_2O_4$ (%)
0.0	100	0	0
0.2	95	3	2
0.4	75	25	0
0.5	75	24	1
0.6	60	17	23
0.8	33	9	58
1.0	0	41	59

Table 6.3 presents the phase concentration percentage values achieved through the refinement. It was also verified that for x >0.60 another phase of $FeCr_2O_4$ (iron chromite) chromite) is observed. This phase became the main constitutive phase after x=0.8. The iron chromite presented a lattice parameter of 0.8347(5) nm and an average crystalline size about 29.6 nm. For all XRD data (Fig. 6.7b) obtained for the samples prepared below $x \leq 0.2$ ($x = 0.02$, 0.05, 0.08, 0.10 and 0.15) we have found a single phase $Eu_{1-x}Fe_xCrO_3$ with only small traces of magnetite and iron chromite (1-4%).

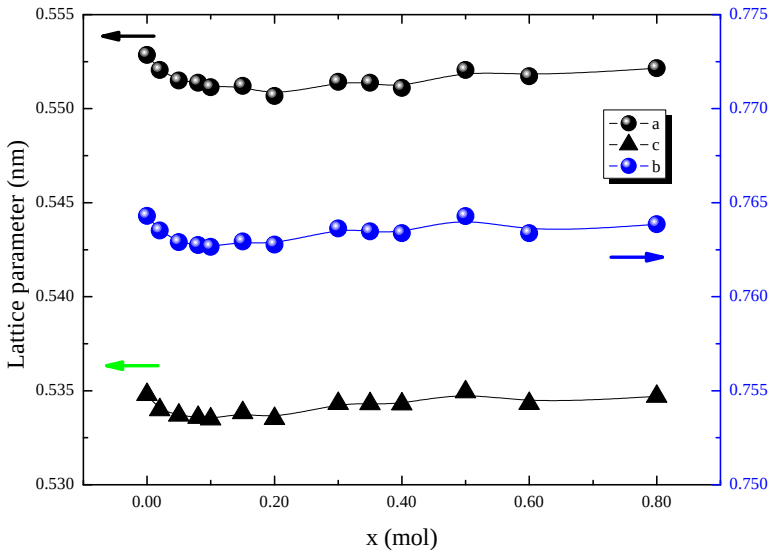

Figure 6.8: Lattice parameter for the $Eu_{1-x}Fe_xCrO_3$ ($0.0 \leq x \leq 1.0$) phase

Fig. 6.8 presents the values for the lattice parameters (a, b and c) of the $EuCrO_3$ perovskite structure, being nearly independent of the iron concentration above $x > 0.2$. Below $x < 0.2$ one sees a slight reduction in the cell parameters, as expected from the small shift in the main diffraction peak attributed to the inclusion of iron ions in the structure. Furthermore, a microstrain analysis (see Fig. 6.9) achieved by the refinement shows once again that the maximum

introduction of iron into the system is about 20%, leading to a maximum in stress on the structure.

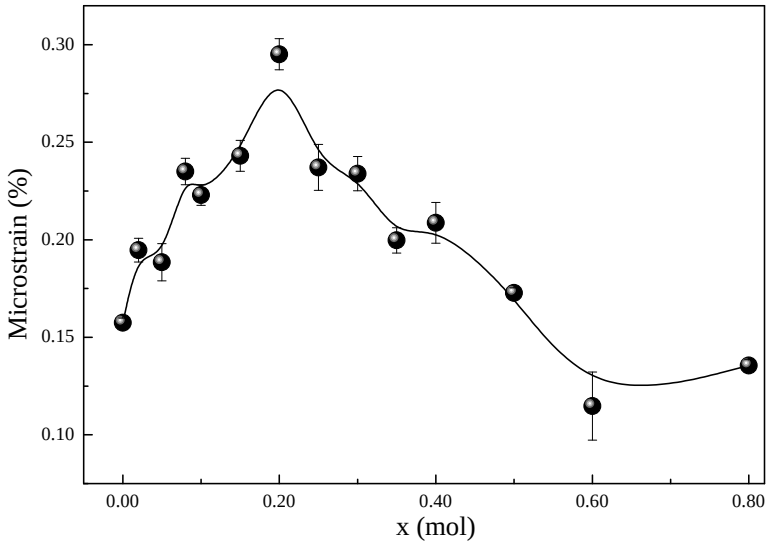

Figure 6.9: Microstrain analysis for the $Eu_{1-x}Fe_xCrO_3$ ($0.0 \leq x \leq 1.0$) phase

6.2.2 Optical analysis

According to the calculation from group theory for the space group Pnma (Number 62) with point group is D_{2h} (mmm), we have eight different vibration modes (Eq. 6.2) where three modes ($\Gamma_{acoustic} = B_{1u} + B_{2u} + B_{3u}$) are acoustic and the other five are optical modes. From those optical modes three are infrared active modes $9B_{1u}$, $7B_{2u}$ and $9B_{3u}$ [89].

$$\Gamma = 7A_g + 8A_u + 5B_{1g} + 10B_{1u} + 7B_{2g} + 8B_{2u} + 5B_{3g} + 10B_{3u} \tag{6.2}$$

FTIR spectra for all the samples doped with iron for the high and low concentrations are presented in Fig 6.10. As observed before, we have several peaks indexed from (a) to (g). Absorptions bands (a) and (d) are attributed to water trapped in the systems, (c) is for carbon dioxide in the air, (b) is related to C-H, C-C and C-N bonding and finally, (e) to the unreacted precursor nitrates, (f) and (g) can be ascribed to Eu-O, Fe-O or Cr-O vibrational modes [85, 86, 90]. From Fig. 6.10b we can infer that for high concentrations of iron there is a small shift in both peaks (which are assigned to the stretching modes of the heavier elements, i.e. Eu-O and Fe-O) towards higher frequency values. In general, the gradual shift in the absorption frequency is due to the increase of oxygen defects that increases with Fe doping concentration and/or

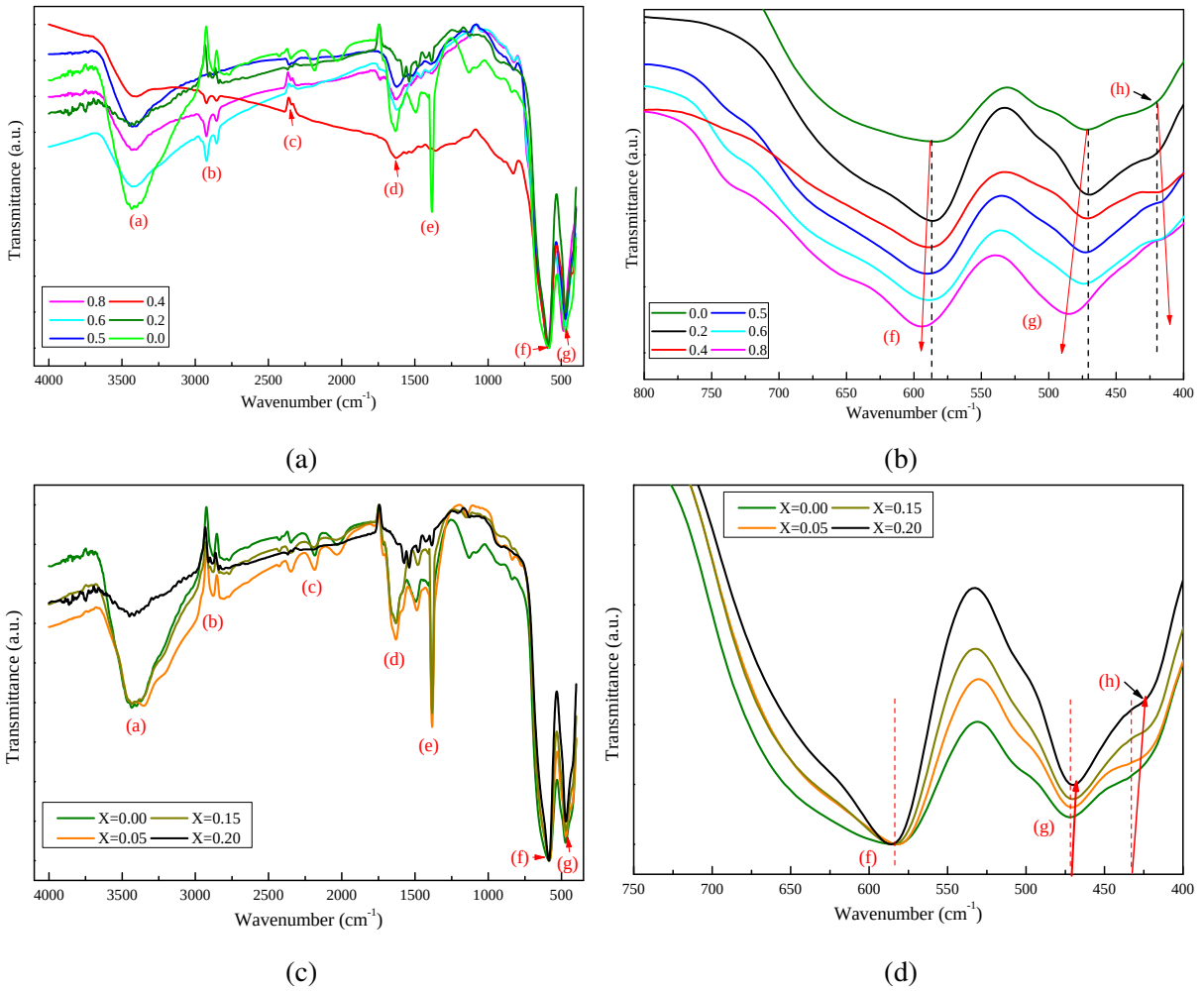

Figure 6.10: FTIR spectra of the undoped- and Fe-doped $EuCrO_3$ nanoparticles in the wavenumber ranges for high concentrations in the range (a) 4000–400 cm^{-1}, (b) enlarged area near the absorption band for Eu-O of 750–400 cm^{-1}.

possible changes in particle size as observed in the X-ray analysis. In addition, the oxygen defects present in the Fe-doped europium chromites are inherent to the sample preparation method. The combustion reaction is regarded as a highly exothermic process that releases a huge amount of heat that may as the iron concentration is increased, thus increasing the amount of oxygen defects. On the other hand, with increasing Fe-doping concentration, more Eu^{3+} ions are gradually substituted by Fe^{3+} ions in the perovskite structure, thus, the wavenumber must change. This phenomenon can be explained using a simple harmonic oscillator model, where the wavenumber has a direct relation with the bond force constant (k) and the reduced mass (μ) of the system (Eq. 6.3). Since Eu and Fe have different molar masses (151.964 g/mol and 55.8545 g/mol, respectively), the wavenumber should suffer some changes in the doping process. In fact, the wavenumber of Eu-O bonding can be compared to the Fe-O bonding by $\nu_{Eu-O} \approx 0.89\nu_{Fe-O}$ [91].

$$\nu = \frac{1}{2\pi c}\sqrt{\frac{k}{\mu}} \tag{6.3}$$

It is important to remark that around 420 cm^{-1} a small peak (h) can be noticed when we enlarge the spectrum for low wave numbers (Fig. 6.10b and 6.10d). This peak belongs to the O–Cr–O vibrational mode which has a very fine shift to a lower wavenumber as function of doping. This behavior has a correlation with O–Cr–O bond angle, implying that there are a deformation in the structure due to the entrance of Fe^{3+} ions at the A site [84].

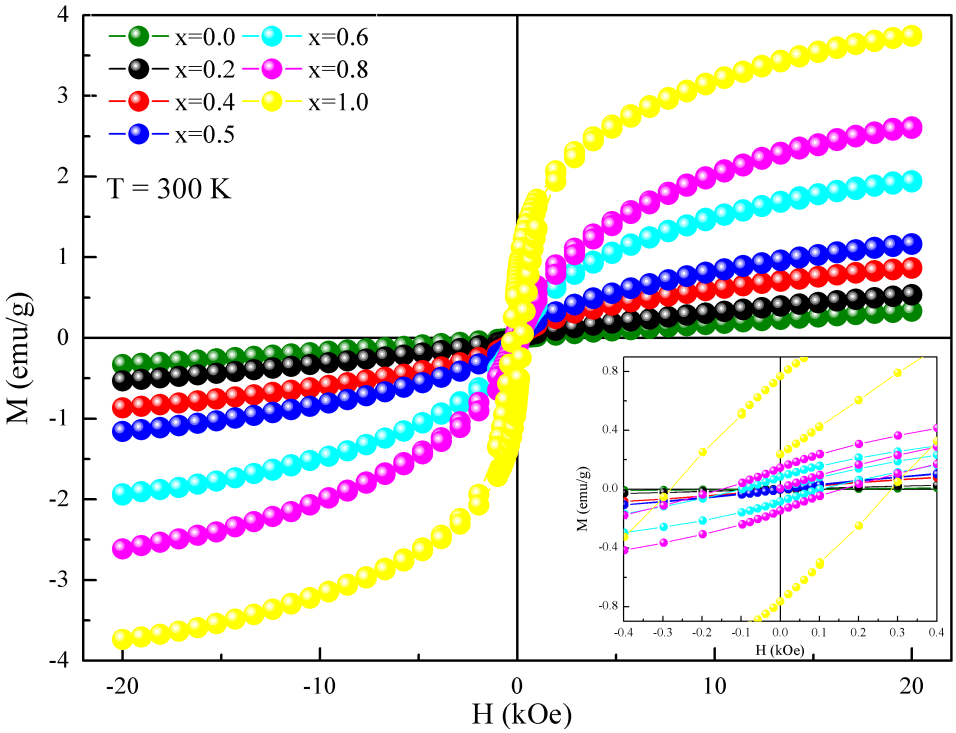

Figure 6.11: M vs H magnetization curves for the iron doped $Eu_{1-x}Fe_xCrO_3$ with $x = 0.0$, 0.2, 0.4, 0.5, 0.6, 0.8 and 1.0

6.2.3 Magnetic analysis

6.2.3.1 Room temperature measurements

At room temperature, we already established that $EuCrO_3$ is paramagnetic (Fig. 6.5), while the magnetic measurements made on the Fe-doped samples, showed a predominant ferromagnetic interaction that gradually enhances as the Fe concentration increases, as seen in Fig. 6.11. This magnetic behavior can be explained as the iron ions are entering progressively in the A-site of the perovskite replacing those europium paramagnetic ones, hence changing their surroundings

(neighborhood). Nevertheless, the principal factor which is leading to this histeretic nature has been related to the presence of the residual magnetite as determined by the X-ray diffraction analysis. As we already know, the limit in iron substitution has been identified to be around $x = 0.2$, were the principal phase present is chromite. After this concentration, the curve starts to have higher values in magnetization that are associated with the increase in the Fe_3O_4 phase and a respective decrease on the single phase chromite (see Table 6.3).

From the M vs H curves, we have extracted some relevant information about the system. The values for the coercive field and magnetization at the highest field applied ($M(H_{max})$) are given by Fig. 6.12. A soft magnetic character is observed (H_c goes from 0 to 280 Oe) with the already discussed rise in the magnetization from 0.33 to 3.75 emu/g when x changes from 0.0 to 1.0 in concentration. As for the remanence (M_r) and the susceptibility (χ) in our nanopowders we have encounter a similar behavior, for instance, M_r increases from ≈ 0 to 0.77 emu/g and the susceptibility slightly raises from values close to 0 to 6.94×10^{-3} emu/g Oe.

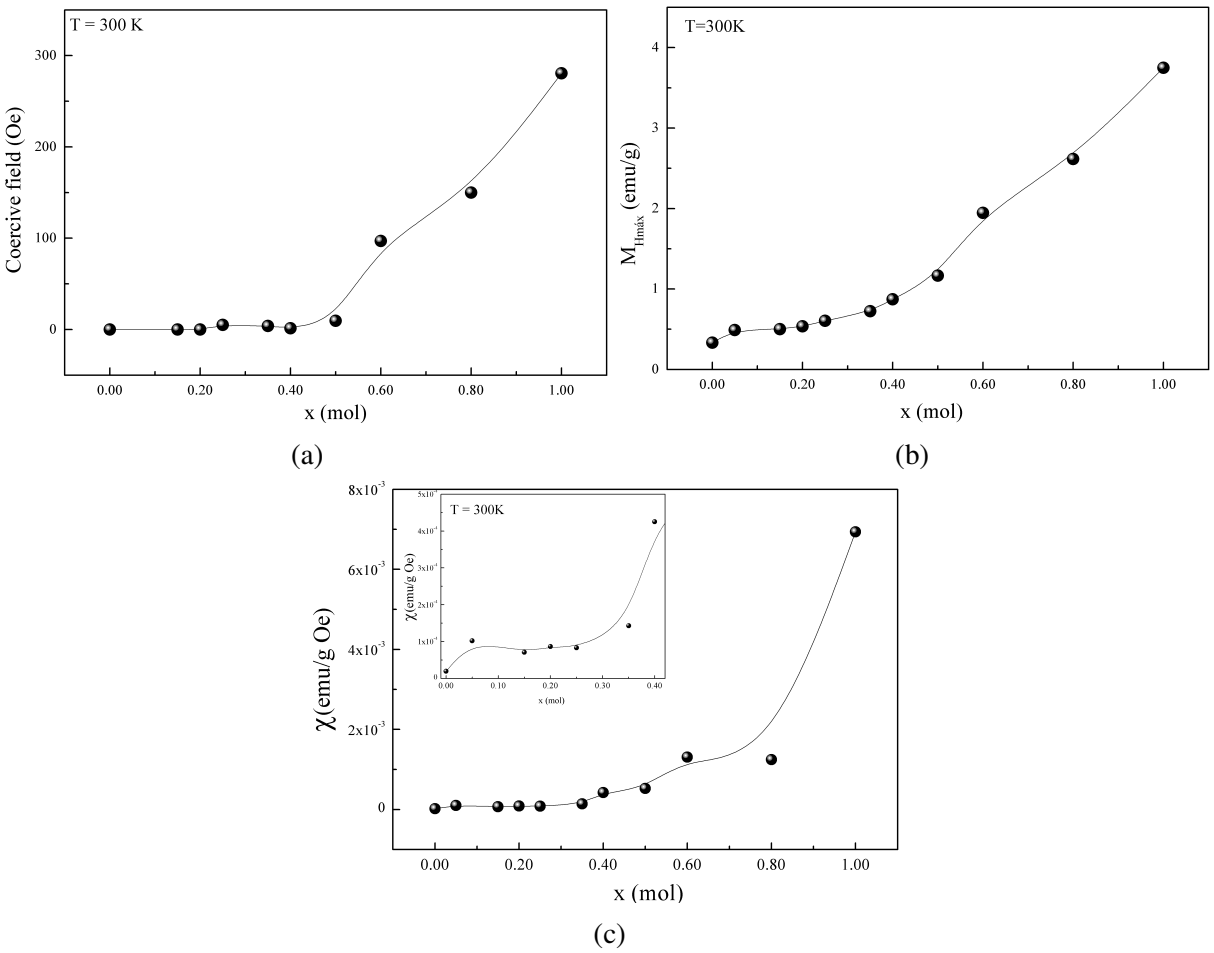

Figure 6.12: (a) Coercive field, (b) $M(H_{max})$ and (c) susceptibility for $Eu_{1-x}Fe_xCrO_3$

6.2.3.2 Low temperature measurements

The magnetization versus temperature for the Fe-doped samples was recorded using both PPMS and VSM systems but focusing our research in low iron concentrations (below $x < 0.2$). This means that we have studied samples that exhibited single phase of $Eu_{1-x}Fe_xCrO_3$.

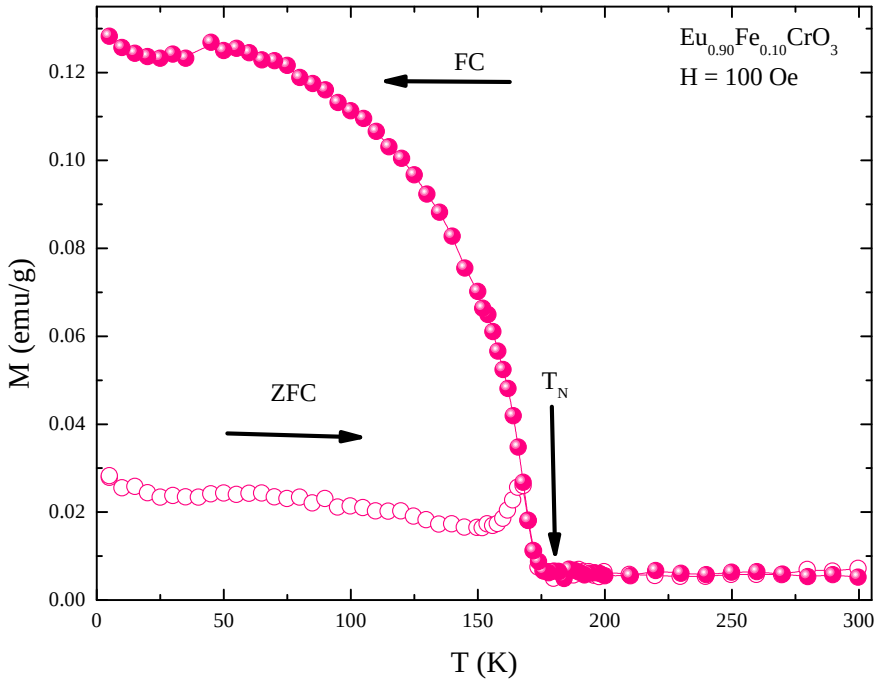

Figure 6.13: Magnetization against temperature measurements for the Fe-doped $Eu_{0.9}Fe_{0.1}CrO_3$ system

Fig. 6.13 presents the ZFC (open circle)-FC (closed circle) data for the sample doped with 10% of iron with an applied field of $H = 100$ Oe in the range 5-300 K. A Néel temperature of 174 K was found, which has a little increase with respect to that of pure europium chromite (171 K). This behavior is expected due to the fact that the microstrain in the system has suffered some changes (increase) in the presence of iron leading to a variation in the bond angle of Cr^{3+}-O^{2-}-Cr^{3+}, in turn, is responsible for the weak magnetic behavior of the system [3, 88]. Furthermore, for the non-doped iron chromite we have also a weak ferromagnetic behavior at temperatures below T_N and a paramagnetism nature at higher temperatures. A detailed analysis of the magnetization curve leads to a Weiss temperature of $\Theta = -213$ K which is connected to the reduction in the magnetization as Fe^{3+} replaces the Eu^{3+} ions. The effective moment (6.95 μ_B) determined by using Eq. 6.1 was found to be close to the one obtained for pure iron chromite (6.97 μ_B). Moreover, microstructures such as phase separation and point defects induced by the presence of iron may also affect the coupling of Cr^{3+} ions.

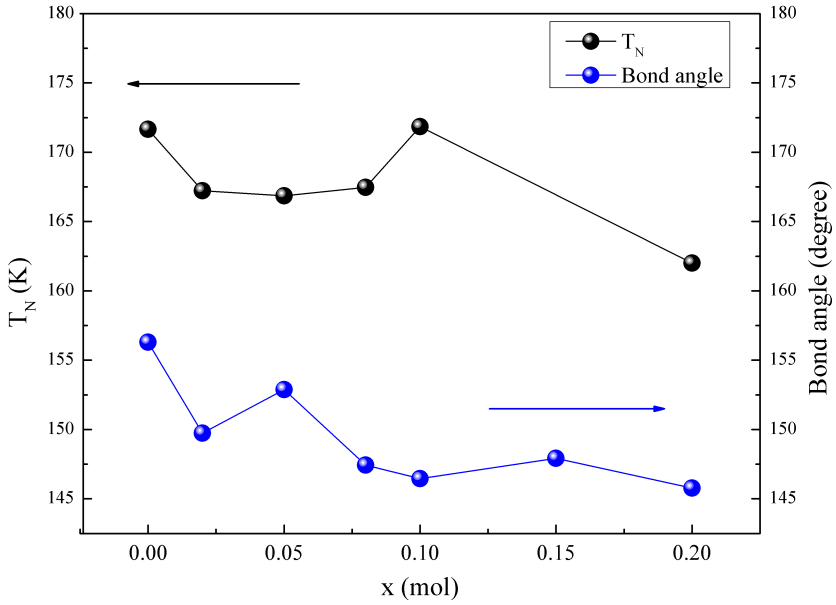

Figure 6.14: Cr-O-Cr bond angle evolution for low iron concentrations ($0.0 \leq x \leq 0.2$)

The Néel temperature was acquired for the set of samples in the region of low iron concentration, i.e. in the area where the system has a structural single phase chromite (below $x \leq 0.2$). An important analysis of the evolution of this quantity as a function of the bonding angle determined from the Rietveld refinements was made with the help of VESTA software. Their respective values are presented in Fig. 6.14, from where we can infer that their behavior are close related. The antiferromagnetic transition temperature (T_N) for Cr^{+3}-Cr^{+3} ordering increases with the rare earth cationic radius (Fig. 2.6a) or, as in our case, when the bonding angle is modified by doping and by the microstrain induced by the synthesis process. This is associated with the diminution in the lattice distortions and increase in the Cr^{+3}-O^{-2}-Cr^{+3} bond angles, thereby varying the intercationic superexchange interaction [3, 92]. Although this phenomenon has had an important role describing the changes in the transition temperature, no detailed reports yet have been found showing the evolution of T_N as a function of the bond angle.

An interesting phenomena can be seen on both M vs. T curves for the $EuCrO_3$ (Fig. 6.6) and $Eu_{0.9}Fe_{0.1}CrO_3$ (Fig. 6.13). When heating the sample the ZFC (open circle) measurement shows a peak in the magnetization just below Néel temperature (Fig. 6.15a). This peak has been associated with the Hopkinson effect which is a result of the difference on the temperature dependence of the magnetocrystalline anisotropy and of the magnetization. This effect can give us an indication of the transition temperature [14]. In fact, it is observed that the Hopkinson peak shifts to higher temperature as the iron concentration is increased (Fig. 6.15b). In Fig.

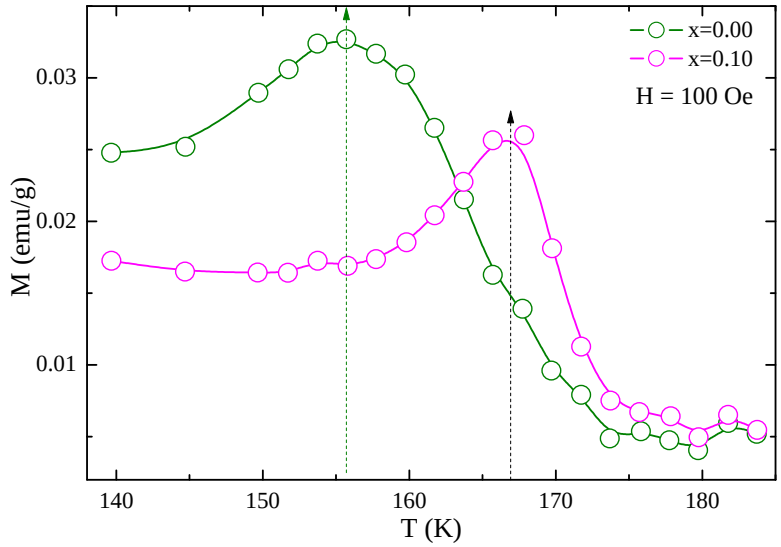

(a)

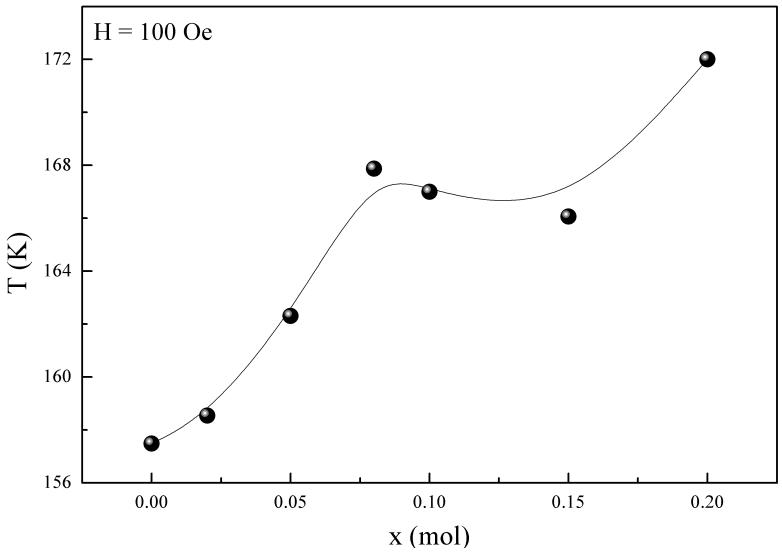

(b)

Figure 6.15: (a) Evidence of the Hopkinson effect for the pure and iron doped ($x = 0.1$) and (b) Hopkinson peak values for $Eu_{1-x}Fe_xCrO_3$ ($0.0 \leq x \leq 0.2$)

6.15a are shown the Hopkinson peaks for the pure europium chromite and for the sample with $x = 0.10$ yielding 156 K and 167 K for the transition temperatures, respectively.

Magnetization against applied magnetic field measurements were made at different temperatures for the low concentration samples. At 5 K we observed that for pure and iron doped chromites with nominal values $x = 0.05$ and 0.10, we are not even close to a saturation magnetization. Additionally the hysteresis loops close at the highest applied magnetic field only. This is a further evidence of the canted antiferromagnetic behavior that needs even higher external fields to align the Cr^{+3} canted ions. As a result, of the difference between the values for the magneti moment of Fe (2.22 μ_B) and Eu (3.4 μ_B), joint with the ionic substitution, leads to a

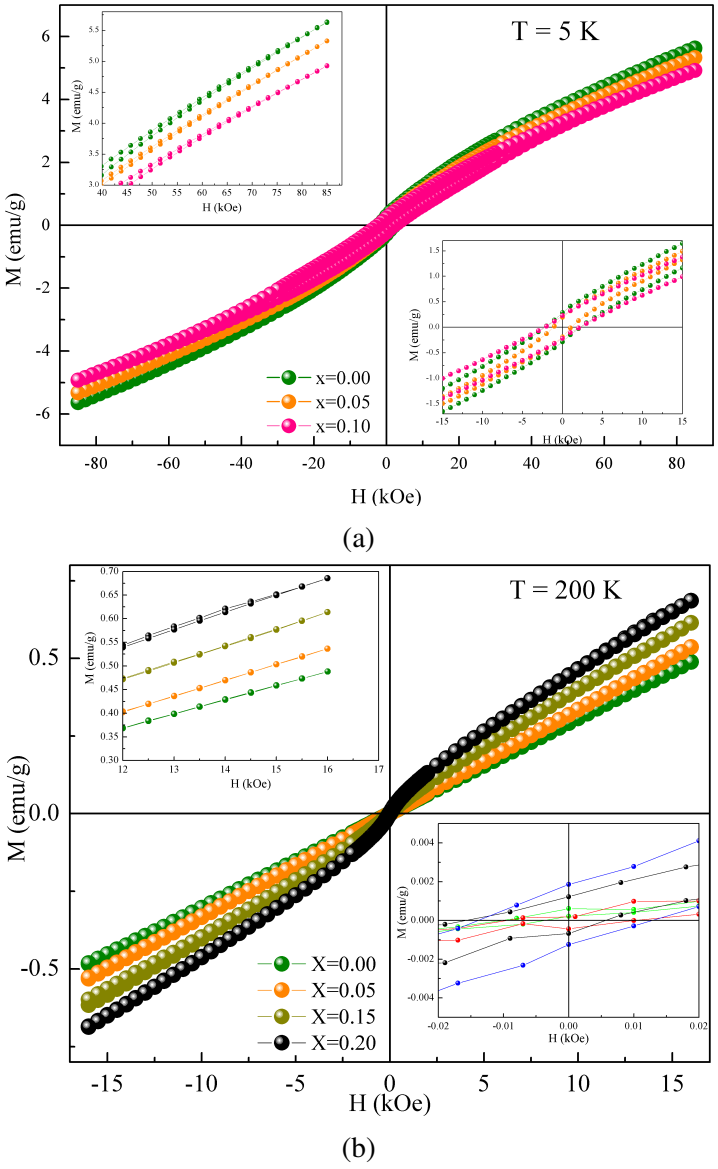

Figure 6.16: Low temperature hysteresis loops measured at (a) 5 K and (b) 200 K.

decrease in the $M_{H(max)}$ upper left inset in Fig. 6.16a. For temperatures above T_N (200 K) we did not expect any considerable changes with respect to those already measured at room temperature, even though we have to observed that for $x = 0.15$ and $x = 0.20$ there are small traces of magnetite in the system. For lower values of x, the nature of the chromites remains the same (paramagnetic).

6.2.4 Thermal analysis

To understand the different transitions that the system fully doped with iron ($x = 1.0$) experiences when heat is supplied to the sample, we have made a TGA-DSC analysis of the as

prepared $FeCrO_3$ (Fig. 6.17). Pure iron doped chromite nanopowders with $x = 1.0$ have a maximum weight loss of 3% and a minor weight gain after 800°C. DSC analysis showed two broad peaks typical of an "exothermic" reaction which is located around at 370°C and at 650°C. Furthermore, after 800°C, there is an increase in the heat absorbed by the system which may be can benefit the formation of oxides such as magnetite.

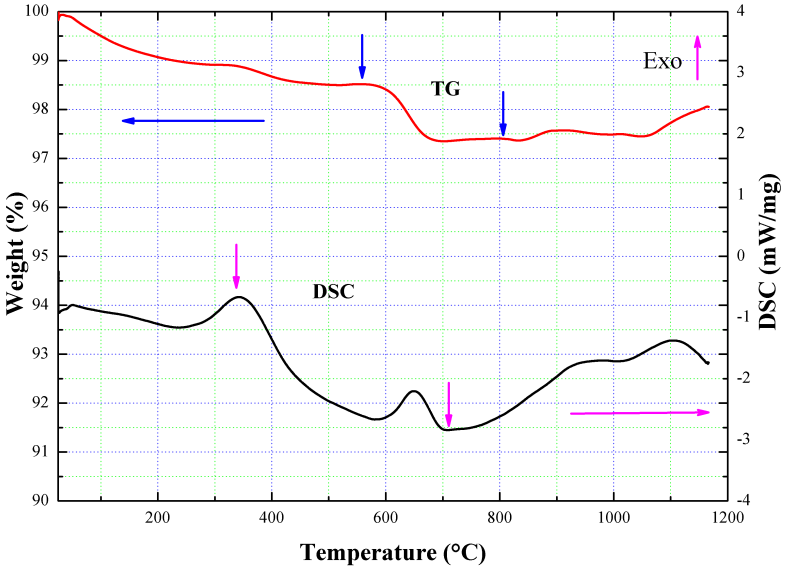

Figure 6.17: $FeCrO_3$ TG-DSC analysis

6.3 Iron doped orthochromites: Thermal treatment

In order to check if there is a slight possibility to extend the limit of diffusion of iron ions into the perovskite structure, we have made two thermal treatments at different time rates to determine the evolution of the system towards a single phase compound, i.e., diminishing the amount of magnetite. The annealing was performed under air atmosphere in a tubular furnace at a maximum temperature of 800°C for 6 and for 24 hours. A heating rate of 10°C/min was used, for cooling down the samples we employed the furnace inertia (close to 6 hours).

6.3.1 Structural analysis

Fig. 6.18a presents the X-ray diffraction results obtained from the annealing of the samples during 6 hours. The central region of the peaks has been detailed to show the evolution of the

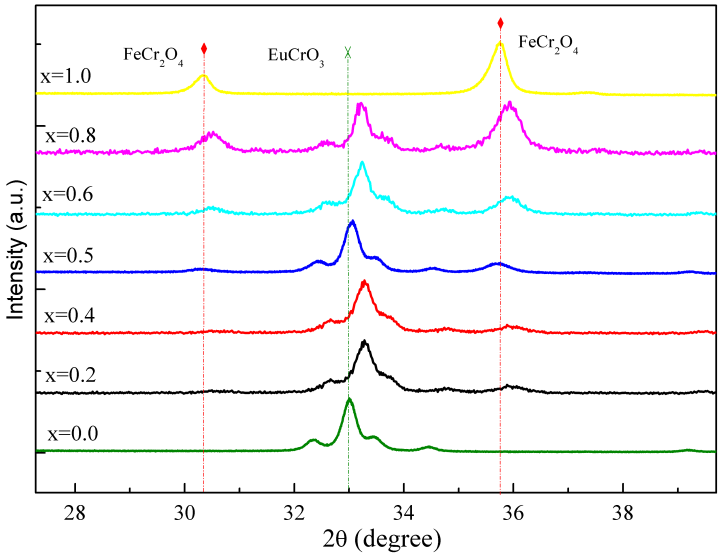

(a)

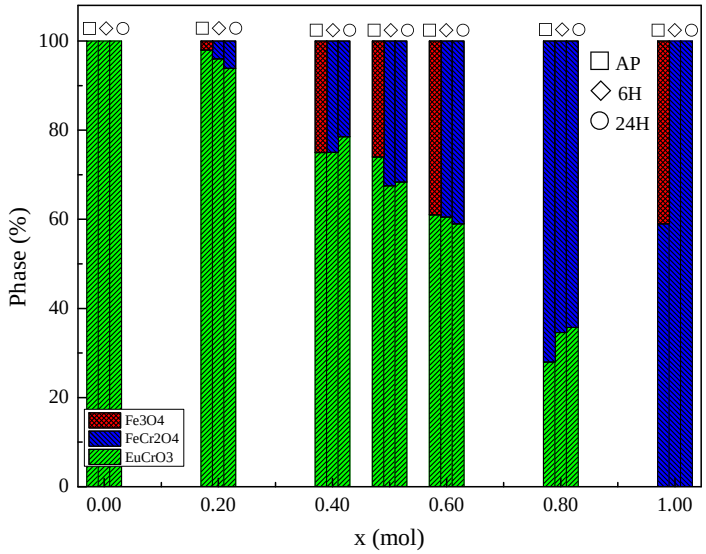

(b)

Figure 6.18: (a) XRD patterns after 6 hours of annealing and (b)phase percentage distribution of the $Eu_{1-x}Fe_xCrO_3$ phase for the (□) as prepared-AP, (◊) 6 and (◯) 24 hours annealed samples

chromite with the addition of iron. From the respective indexing of the diffraction peaks it is easy to determine the presence of two predominant phases ($EuCrO_3$ and $FeCr_2O_4$) and the total reduction of the residual Fe_3O_4. Contrary to what we were expecting, the thermal treatments employed did not affect the substitution of iron ions in the chromite, more precisely, it seems as it favors the appearance of iron chromite independent of the annealing time. For $x = 1.0$ there is no evidence of magnetite which leads to the fact that in order to synthesize this type of chromites (iron based) it is essential to use an additional calcinating step after the combustion reaction preparation.

Lattice parameters a and c for the annealed perovskiste $EuCrO_3$ phase remains nearly constant when compared to to the results for the non-annealed samples (Fig. 6.19a). The b parameter has a slight increase ($\approx 1\%$), yet the final values are in good agreement to the reported for single phase $EuCrO_3$. Fig 6.19b exhibits the microstrain analysis of the as-prepared samples compared to those annealed, revealing that the thermal treatment leads to a relief of strain on the system, with a nearly 50% reduction in values which is independent of the annealing time. Furthermore, it seems as the annealing has no direct consequences on the conformation of doped chromite structures above $x = 0.20$. Crystallite size increases (about 30%), because temperature promotes the crystallization and formation of agglomerates in the compound. This increment goes from 66 nm for the as-prepared samples to 94 nm for the thermal treated $EuCrO_3$.

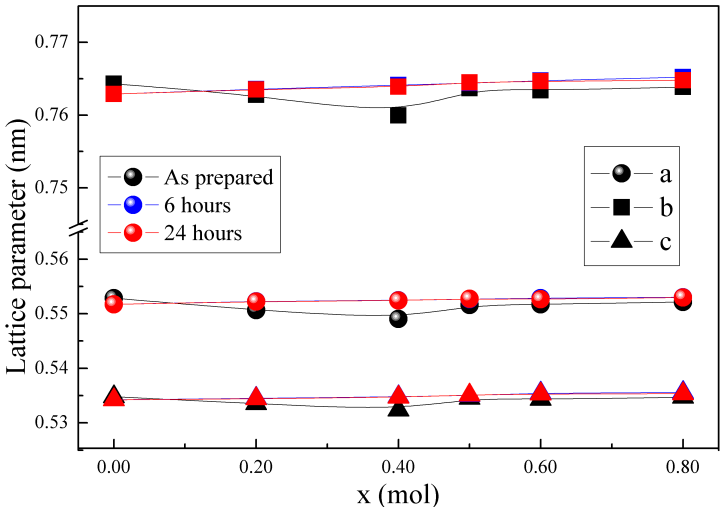

(a)

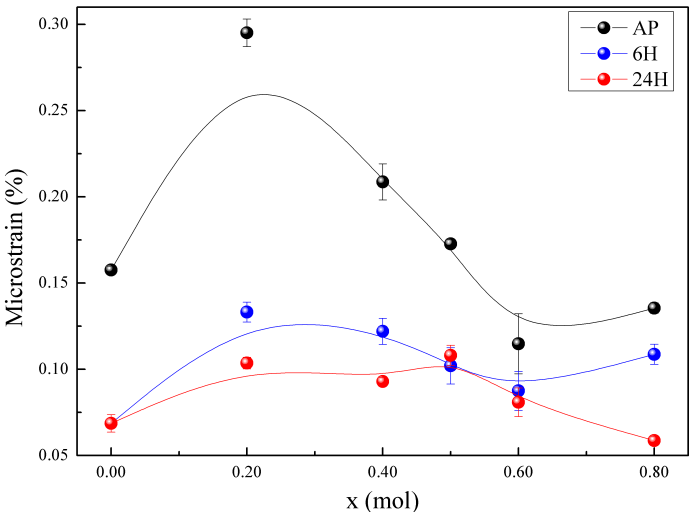

(b)

Figure 6.19: Comparison of the (a) lattice parameter and (b) microstrain values for the as prepared (black), 6 hours (blue) and 24 hour annealed (red) samples of $Eu_{1-x}Fe_xCrO_3$

6.3.2 Magnetic analysis

Curves of magnetization as a function of the external applied magnetic field were measured at room temperature for the annealed iron doped samples (Fig. 6.20a). Compared to the as prepared system we can observe that there is an inhibition of the ferromagnetic-like character, which is affiliated to the structural changes suffer from the annealing (reduction and disappearance of magnetite). This new phase, i.e, spinel $FeCr_2O_4$ has a canted spin antiferromagnet nature at low temperature [93] and a T_N in the 70–80 K range [94]. At room temperature presents a weak paramagnetic behavior as Fig 6.20b suggest. It is important to notice that the magnetization (or χ) of the sample decreases as the spinel phase growths (see 6.18) which mean that the $FeCr_2O_4$ has a weaker magnetic moment than $EuCrO_3$ at room temperature, as seen in Fig. 6.20b. Crystallite size evolution through the process can also give us an insight of what is happening since there is a larger formation of the spinel compared to the $EuCrO_3$, which implies that the net magnetic moment all over the sample decreases.

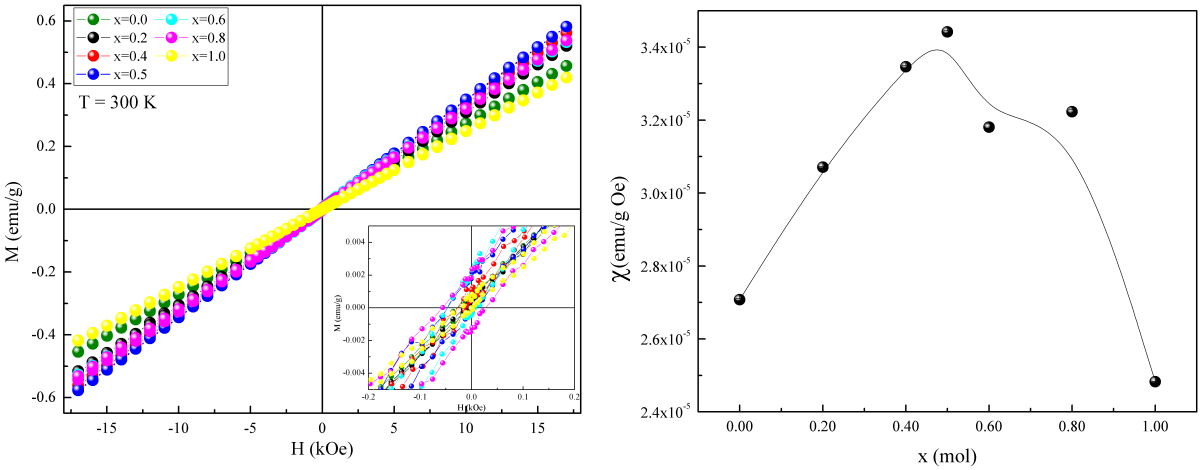

(a) (b)

Figure 6.20: (a) M vs H curves as function of iron concentration and (b) susceptibility evolution for the annealed samples

7

Conclusions and perspectives

One of the main landmarks of our research was to synthesized the rare earth europium chromite ($EuCrO_3$) using the combustion reaction method. This an important improvement in terms of time compared with techniques such as solid state reaction, wet-chemical synthesis or microwave-assisted synthesis. $EuCrO_3$ presents a nanometric size ($\approx$ 66 nm) with a broad distribution of grain sizes, a bonding angle between Cr-O-Cr ions of 152° and is quite stable in terms of temperature. Furthermore, exhibits a paramagnetic behavior above Néel temperature ($T_N = 172$ K) and a weak ferromagnetism below this temperature which is attributed to the canting of Cr^{+3} yielding an effective moment of $P\mu_B = 6.97\mu_B$. Optical analysis leads to an identification of the stretching mode for Eu-O around 473-584 cm^{-1}.

We were able to dope the system with iron in different concentrations and study the effect on the structural and magnetic characteristic of the system. For lower concentrations of iron (below 20%) we reached a nearly single phase of $Eu_{1-x}Fe_xCrO_3$. After this point segregate phases were found, such as iron chromite and magnetite were observed. The presence of magnetite has been accounted for the ferromagnetic-like behavior at room temperature of the samples above $x \geq 0.20$. From the Rietveld analysis performed on the X-ray diffractograms, we have identified a maximum in microstrain and an increase in lattice parameter for x below 0.20 that is linked to a maximum iron substitution in the A-site of the perovskite. As expected, it was observed a broad distribution of particle sizes with roughly spherical form. FTIR measurements indicated a slight modification of the stretching mode of O-Cr-O towards lower values due to the effect of iron in the cell.

Changes in the magnetization of the $Eu_{1-x}Fe_xCrO_3$ at low iron concentration limit have

been observed. The changes were associated to the substitution of iron ions in the distorted perovskite occurs in the A-site which is occupied by Eu ions. Moreover, when Eu ions are replaced by Fe ions the net magnetic moment become weaker. Low-temperature magnetization measurements data unfold that the Néel temperature is modified through the process, this is a direct consequence of the Cr^{+3}-O^{-2}-Cr^{+3} angle distortion generated by both synthesis process and microstrain. This behavior is expected for such systems and no other report has been found that describes in detail the evolution of the Néel temperature angle as function of the Cr^{+3}-O^{-2}-Cr^{+3} angle. Finally, a thermal treatment at 800°C for the Fe-doped based samples at different annealing times shows a reduction in the microstrain.

Further analysis should be made at low temperature for the whole range of iron doped samples $Eu_{1-x}Fe_xCrO_3$ to expand our understanding of the transition temperature with the bonding angles. Likewise, we could study the effect of different doping in the europium chromites. For instance, we already have started to research the effects of holmium. Moreover, magnetization against temperature measurements over the annealed samples will give us an insight to determine which parameter is more important in the distortion of the Cr^{+3}-O^{-2}-Cr^{+3}, microstrain or the addition of iron..

Bibliography

[1] TSUSHIMA, K.; TAKEMURA, I.; OSAKA, S. Weak ferromagnetism in $EuCrO_3$. *Solid State Communications*, Oxford, p. 71–73, 1969.

[2] WIDATALLAH, H.; AL-SHAHUMI, T.; KLENCSáR, Z.; PEKALA, M.; GISMELSEED, A.; AL-OMARI, I.; AL-RAWAS, A.; SEIFU, D. Structural, magnetic and ^{1}51Eu mössbauer studies of mechanosynthesized nanocrystalline $EuCr_{1-x}Fe_xO_3$ particles. *Acta Materialia*, , n. 12, p. 4461–4473, 2013.

[3] PRADO-GONJAL, J.; SCHMIDT, R.; ROMERO, J.-J.; ÁVILA, D.; AMADOR, U.; MORÁN, E. Microwave-assisted synthesis, microstructure, and physical properties of rare-earth chromites. *Inorganic Chemistry*, v. 52, n. 1, p. 313–320, 2013.

[4] DENG, D.; WANG, X.; ZHENG, J.; QIAN, X.; YU, D.; SUN, D.; JING, C.; LU, B.; KANG, B.; CAO, S.; ZHANG, J. Phase separation and exchange bias effect in Ca doped EuCrO3. *Journal of Magnetism and Magnetic Materials*, Amsterdam, v. 395, p. 283–288, 2015.

[5] KUZNETSOV, M. V.; PARKIN, I. P. Convenient rapid synthesis of rare earth orthochromites $LnCrO_2$ by self-propagating high-temperature synthesis. *Polyhedron*, v. 17, n. 25,26, p. 4443–4450, 1998.

[6] RASHAD, M.; EL-SHEIK, S. Magnetic properties of nano-clusters lanthanum chromite powders doped with samarium and strontium ions synthesized via a novel combustion method. *Material Research Bullerin*, v. 46, p. 469–477, 2011.

[7] KHETRE, S.; CHOPADE, A.; JADHAV, H.; KULAL, S.; JAGADALE, P.; BANGALE, S.; BAMANE, S. Auto-combustion synthesis of nanocrystalline $FeCrO_3$. In: . c2011. p. 1–6.

[8] KITTEL, C. *Introduction to solid state physics*. 8. ed. John Wiley & Sons, Inc., 2005.

[9] JILES, D. Recent advances and future directions in magnetic materials. *Acta Materialia*, v. 51, p. 5907–5939, 2003.

[10] MASSARI, S.; RUBERTI, M. Rare earth elements as critical raw materials: Focus on international markets and future strategies. *Resources Policy*, v. 38, p. 36–43, 2013.

[11] D, X.; GRAEDEL, T. E. *Environ. Sci. Technol.*, v. 45, p. 4096–4101, 2011.

[12] JORDENS, A.; CHENG, Y. P.; WATERS, K. E. *Minerals Engineering*, v. 41, p. 97–114, 2013.

[13] GUPTA, C.; KRISHNAMURTHY, N. *Extractive metallurgy of rare earths*. CRC Press, 2005.

[14] CULLITY, B.; GRAHAM, C. *Introduction to magnetic materials*. Second. ed. Wiley, 2009.

[15] JENSEN, J.; MACKINTOSH, A. R. *Rare earth magnetism*. Clareddon Press - Oxford, 1991.

[16] CHIKAZUMI, S. *Physics of ferromagnetism*. Second. ed. Oxford, 2009.

[17] O'HANDLEY, R. C. *Modern magnetic materials: Principles and applications*. John Wiley & Sons, INC., 2000.

[18] MORRISH, A. H. *The physical principles of magnetism*. IEEE Press, 2001.

[19] GUIMARAES, A. P. *Principles of nanomagnetism*. Springer, 2009.

[20] GIAQUINTA, D. M.; ZUR LOYE, H.-C. Structural predictions in the ABO3 phase diagram. *Chemistry of Materials*, v. 6, n. 4, p. 365–372, 1994.

[21] KUMAR, A.; VERMA, A.; BHARDWAJ, S. *The Open Applied Physics Journal*, 2008.

[22] WEBER, M. C.; KREISEL, J.; THOMAS, P. A.; NEWTON, M.; SARDAR, K.; WALTON, R. I. *Physical Review B*, 2012.

[23] MARTIN, L.; CRANE, S.; CHU, Y.; HOLCOMB, M.; GAJEK, M.; HUIJBEN, M.; YANG, C.; BALKE, N.; RAMESH, R. Multiferroics and magnetoelectrics: thin films and nanostructures. *J. Phys.: Condens. Matter*, v. 20, n. 434220, p. 13 pp, 2008.

[24] SAHU, J. R.; SERRAO, C. R.; RAY, N.; WAGHMARE, U. V.; RAO, C. N. R. Rare earth chromites: a new family of multiferroics. *J. Mater. Chem.*, v. 17, p. 42–44, 2007.

[25] DURÁN, A.; ARÉVALO-LÓPEZ, A.; CASTILLO-MARTÍNEZ, E.; GARCÍA-GUADERRANA, M.; MORAN, E.; CRUZ, M.; FERNÁNDEZ, F.; ALARIO-FRANCO, M. Magneto-thermal and dielectric properties of biferroic $YCrO_3$ prepared by combustion synthesis. *Journal of Solid State Chemistry*, Orlando, v. 183, n. 1863-1871, 2010.

[26] HORNREICH, R. Magnetic interactions and weak ferromagnetism in the rare-earth orthochromites. *Journal of Magnetism and Magnetic Materials*, Amsterdam, v. 7, n. 1–4, p. 280 – 285, 1978.

[27] PRADO-GONJAL, J.; SCHMIDT, R.; AVILA, D.; AMADOR, U.; MORAN, E. Structural and physical properties of microwave synthesized orthorhombic perovskite erbium chromite $ErCrO_3$. *J. of the European Ceramic Society*, v. 32, n. 611, 2012.

[28] RAO, G. S.; WANKLYN, B.; RAO, C. Electrical transport in rare earth ortho-chromites, -manganites and -ferrites. *Journal of Physics and Chemistry of Solids*, v. 32, n. 2, p. 345 – 358, 1971.

[29] GOLOVENCHITS, E. I.; SANINA, V. A.; SHAPLYTINA, T. A. *Sov. Phys. JETP*, v. 53, n. 5, May 1981.

[30] SU, Y. L.; ZHANG, J. C.; LI, L.; FENG, Z. J.; LI, B. Z.; ZHOU, Y.; CAO, S. X. Novel magnetization induced by phase coexistence in multiferroic $HoCrO_3$ chromites. *Ferroelectrics*, v. 410, n. 1, 2011.

[31] SARDAR, K.; LEES, M. R.; KASHTIBAN, R. J.; SLOAN, J.; WALTON, R. I. Direct hydrothermal synthesis and physical properties of rare-earth and yttrium orthochromite perovskites. *Chemistry of Materials*, v. 23, n. 1, p. 48–56, 2011.

[32] RATH, C.; P.MOHANTY; A.BANERJEE. Magnetic properties of nanoparticles of cobalt chromite. *J. Mag. Mag. Materials*, v. 323, n. 1698, 2011.

[33] KINGSLEY, J.; PEDERSON, L. Combustion synthesis of perovskite $LnCr0_3$ powders using ammonium dichromate. *Materials Letters*, v. 18, p. 89–96, 1993.

[34] CALLISTER, W. D.; RETHWISCH, D. G. *Materials science and engineering: An introduction*. 8. ed. Wiley, 2009.

[35] SERWAY, R. A.; JOHN W. JEWETT, J. *Physics for scientists and engineers 8th edition*. 8. ed. Cengage Learning, 2010.

[36] COEY, J. M. D. *Magnetism and magnetic materials*. Cambridge, 2010.

[37] BLUNDELL, S. *Magnetism in condensed matter*. Oxford, 2001.

[38] SILVERA, I.F., THORNLEY, J.H.M, TINKHAM, M. Magnetic properties of the canted. v. 539, n. 1959, 1962.

[39] GETZLAFF, M. *Fundamentals of magnetism*. Springer, 2008.

[40] SÍAMA, J.; ŠOKA, M.; GRUSKOVÁ, A.; GONZALEZ, A.; JANČÁRIK, V. Hopkinson effect study in spinel and hexagonal ferrites. *Journal of Electrical Engineering*, v. 62, n. 4, p. 239–243, 2011.

[41] STONER, E. C.; WOHLFARTH, E. P. A Mechanism of Magnetic Hysteresis in Heterogeneous Alloys. *Philosophical Transactions of the Royal Society of London Series A*, v. 240, p. 599–642, May 1948.

[42] FANG, Q.; CHENG, H.; HUANG, K.; WANG, J.; LI, R.; JIAO, Y. Doping effect on crystal structure and magnetic properties of chromium-substituted strontium hexaferrite nanoparticles. *Journal of Magnetism and Magnetic Materials*, Amsterdam, v. 294, n. 3, p. 281–286, 2005.

[43] NOLTING, W.; RAMAKANTH, A. *Quantum theory of magnetism*. Springer, 2009.

[44] YOSHIDA, K. *Theory of magnetism*. Springer, 1996.

[45] GUIMARÃES, A. P. *Magnetism and magnetic resonance in solids*. Wiley, 1998.

[46] ARUNA, S. T.; MUKASYAN, A. S. Combustion synthesis and nanomaterials. *Current opinion in Solid State and Materials Science*, , n. 12, p. 44–50, 2008.

[47] ALVES, A.; BERGMANN, C.; BERUTTI, F. Novel synthesis and characterization of nanostructured materials. *Engineering Materials, DOI: 10.1007/978-3-642-41275-2_2*, , n. 85, 2013.

[48] FUMO, D.; MORELLI, M.; AES, A. S. Combustion synthesis of calcium aluminates. *Material Research Bulletin*, v. 31, n. 10, p. 1243–1255, 1996.

[49] JUNIOR, A. F.; SANTANA, R. C. Electron paramagnetic resonance (epr) of antiferromagnetic nanoparticles of $La_{1-x}Sr_xCrO_3$ ($0.000 \leq x \leq 0.020$) synthesized by combustion reaction. *Materials Chemistry and Physics*, v. 120, p. 225–228, 2010.

[50] RUTH H.G.A, K. Combustion synthesis of nanopowder ceramic powders. *KONA*, v. 19, p. 156–166, 2001.

[51] MIMANI, T. Fire synthesis: preparation of alumina related products. *Resonance*, v. 5, p. 50–57, 2000.

[52] MOORE, J.; FENG, H. Combustion synthesis of advanced materiasl: Part II. classification, applications and modelling. *Progress in material science*, v. 39, p. 275–316, 1995.

[53] BARRERE, M.; JAUMOTE, A.; DEVEUBEKE, B.; VANDENKEREKHOVE. Rocket propulson. *Elsevier, Amsterdam*, v. 132, 1960.

[54] BAKHMAN, N. A stoichiometric coefficient reflecting the elemental composition of fuel and oxidizer. *Combustion, explosion and shock waves*, v. 4, n. 1, p. 16–19, 1968.

[55] JAIN, S.; ADIGA, K.; VERNEKER, V. P. A new approach to termochemical calculations of condensed fuel-oxidazer mixtures. *Combustion and Flame*, v. 40, p. 71–79, 1981.

[56] LIMA, M.; BONADIMANN, R.; DE ANDRADE, M.; TONIOLO, J.; BERGMANN, C. Nanocrystalline Cr_2O_3 and amorphous CrO_3 produced by solution combustion synthesis. *Journal of the European Ceramic Society*, v. 26, p. 1213–1220, 2006.

[57] RÖNTGEN, W. K. On a new kind of rays. *Nature*, London, p. 274–276, 1986.

[58] EWALD, P. *Fifty years of x-ray diffraction*. International union of cristallography (IuCr), 1962.

[59] CULLITY, B. *Elements of x-ray diffraction*. Addison-Wesley, 1956.

[60] ECKERT, M. Max von laue and the discovery of x-ray diffraction in 1912. *Ann. Phys. (Berlin)*, v. 524, n. 5, p. A83–A85, 2012.

[61] WARREN, B. X-ray diffraction. *Dover, New York: addison wesley*, p. 251–314, 1990.

[62] RIETVELD, H. The rietveld method - a historial perspective. *Aust. J. Phys.*, p. 113–116, 1988.

[63] LUTTEROTTI, L.; MATTHIES, S.; WENK, H. Maud: a friendly java program for material analysis using diffraction. *IUCr: Newsletter of the CPD*, v. 21, n. 14-15, 1999.

[64] FONER, S. Versatile and sensitive vibrating-sample magnetometer. *The review of scientific instruments*, v. 30, n. 7, p. 548–557, July 1959.

[65] SAMPAIO, L.; GARCÍA, F.; CERNICCHIARO, G.; TAKEUCHI, A. Técnicas de magnetometria. *Revista Brasileira de Ensino de Física*, v. 22, n. 3, p. 406–410, September 2000.

[66] BURGEI, W.; PECHAN, M.; JAEGER, H. A simple vibrating magnetometer for use in a materials physics course. *Am. J. Phys.*, v. 71, n. 8, p. 825–828, August 2003.

[67] http://www.qdusa.com/sitedocs/productBrochures/1070-002.pdf.

[68] BROWN, M.; GALLAGHER, P. *Handbook of thermal analysis and calorimetry*. Elsevier, 2008. v. 5.

[69] `http://www.setaram.com/traitement/export_doc.php?doc=/files/documents/LABSYSevo-2012.pdf`.

[70] https://www.netzsch-thermal-analysis.com/us/products-solutions/differential-scanning-calorimetry/dsc-214-polyma/. Dsc analysis.

[71] DANLEY, R. New heat flux dsc measurement technique. *Thermochimica Acta*, v. 395, p. 201–208, 2003.

[72] MASTERS, B. History of the electron microscope in cell biology. *Encyclopedia of Life Sciences (ELS)*, 2009. John Wiley and Sons, Ltd: Chichester.

[73] WILLIAMS, D.; CARTER, C. B. *Transmission electron microscopy. a textbook for materials science*. Springer, 2009.

[74] http://www.ufrgs.br/imunovet/molecular¡mmunology/microscopy.html.TEMandSEMconfigurations

[75] DEDAVID, B.; GOMES, C.; MACHADO, G. *Microscopia electrônica de varredura. aplicações e preparação de amostras*. EDIPUCRS, 2007.

[76] BOGNER, A.; JOUNEAU, P.-H.; AMD D. BASSET, G. T.; GAUTHIER, C. A history of scanning electron microscopy developments: Towards "wet-stem" imaging. *Micron*, v. 38, p. 390–401, 2007.

[77] GRIFFITHS, P. R.; HASETH, J. A. D. *Fourier transform infrared spectrometry*. 2. ed. John Wiley & Sons, INC., 2007.

[78] SMITH, B. *Fundamentals of fourier transform infrared spectroscopy*. 2. ed. CRC Press, 2011.

[79] BARR, E. The infrared pioneers—I. Sir William Herschel. *Infrared Physics*, v. 1, n. 1, p. 1 – IN6, 1961.

[80] JúNIOR, A. F.; DE OLIVEIRA LIMA, E. C.; NOVAK, M. A.; JR, P. R. W. Synthesis of nanoparticles of $Co_xFe_{3-x}O_4$ by combustion reaction method. *Journal of Magnetism and Magnetic Materials*, Amsterdam, v. 308, p. 198–202, 2007.

[81] MOMMA, K.; IZUMI, F. *VESTA3* for three-dimensional visualization of crystal, volumetric and morphology data. *Journal of Applied Crystallography*, v. 44, n. 6, p. 1272–1276, Dec 2011.

[82] WIDATALLAH, H.; AL-HARTHI, S.; JHONSON, C.; KLENACSáR, Z.; GISMELSEED, A.; MOORE, E.; AL-RAWAS, A.; WYNTER, C.; BROWN, D. Formation, cationic site exchange and surface estructure of mechanosynthesized $EuCrO_3$ nanocrystalline particles. *J. Phys. D: Appl. Phys.*, v. 44, n. 265403, p. 9pp, 2011.

[83] FARZANEH, F.; NAJAFI, M. Synthesis and characterization of Cr_2O_3 nanoparticles with triethanolamine in water under microwave irradiation. *Journal of Sciences, Islamic Republic of Iran*, v. 22, n. 4, p. 329–33, 2011.

[84] ATHAWALE, A.; DESAI, P. Silver doped lanthanum chromites by microwave combustion method. *Ceramics International*, v. 37, n. 8, p. 3037–3043, 2011.

[85] JAISWAL, A.; DAS, R.; ADYANTHAYA, S.; PODDAR, P. Synthesis and optical studies of $gdcro_3$ nanoparticles. *Journal of Nanoparticle Research*, v. 13, n. 3, p. 1019–1027, 2011.

[86] PARKIN, I.; KOMAROV, A.; FANG, Q. Alternative solid state routes to mixed metal oxides ($LnCrO_3$, $LnFeO_3$). *Polyhedron*, v. 15, n. 18, p. 3117 – 3121, 1996.

[87] YOSHII, K. Magnetic Properties of Perovskite GdCrO3. *Journal of Solid State Chemistry*, Orlando, v. 159, n. 1, p. 204–208, 2001.

[88] TIWARI, B.; SURENDRA, M. K.; RAO, M. S. R. $HoCrO_3$ and $YCrO_3$: a comparative study. *J. Phys.: Condensed Matter*, v. 25, n. 216004, p. 7pp, 2013.

[89] http://www.cryst.ehu.es/cgi-bin/cryst/programs/nph-sam. Bilbao crystallographic server.

[90] PATIL, R. M.; SHETE, P. B.; THORAT, N. D.; OTARI, S. V.; BARICK, K. C.; PRASAD, A.; NINGTHOUJAM, R. S.; TIWALE, B. M.; PAWAR, S. H. Non-aqueous to aqueous phase transfer of oleic acid coated iron oxide nanoparticles for hyperthermia application. *RSC Adv.*, v. 4, p. 4515–4522, 2014.

[91] FRANCO, A.; PESSONI, H. Enhanced dielectric constant of Co-doped ZnO nanoparticulate powders. *Physica B: Condensed Matter*, v. 476, p. 12–18, 2015.

[92] JAISWAL, A.; DAS, R.; VIVEKANAND, K.; MAITY, T.; ABRAHAM, P. M.; ADYANTHAYA, S.; PODDAR, P. Magnetic and dielectric properties and Raman spectroscopy of GdCrO3 nanoparticles. *Journal of Applied Physics*, Woodbury, v. 107, n. 1, p. 013912, 2010.

[93] ROBBINS, M.; WERTHEIM, G.; SHERWOOD, R.; BUCHANAN, D. Magnetic properties and site distributions in the system $FeCr_2O_4$-Fe_3O_4. v. C1, n. 32, p. 266–267.

[94] GATTACCECA, J.; ROCHETTE, P.; LAGROIX, F.; MATHé, P.-E.; ZANDA, B. Low temperature magnetic transition of chromite in ordinary chondrites. *Geophysical Research Letters*, v. 38, n. 10, 2011.

[95] Y., S.; J., Z.; Z., F.; Z., L.; Y., S.; S., C. Magnetic properties of rare earth $HoCrO_3$ chromites. *Journal of rare earths*, v. 29, n. 11, p. 1060–1065, 2011.

[96] http://www.chemistryviews.org/details/ezine/2064331/100th$_A nniversary_o f_t he_D iscovery_o f_X - ray_D if f raction.html$.

[97] M.WHITE, R. *Quantum theory of magnetism*. Springer Series in solid-state sciences. Springer, 2007.

[98] HTTP://MMRC.CALTECH.EDU/FTIR/FTIRINTRO.PDF.

Appendix A

Theory of paramagnetism

The origin of paramagnetism has already been introduced where the first systematic measurements of the susceptibility of a large number of substances over an extended range of temperature were made by Pierre Curie and reported by him in 1895. But their behavior remains without explanation for ten years, then in 1905, Langevin introduced his theory of paramagnetism. In here we will look into the classical and quantum treatment of the theory of paramagnetism, from which we can obtain the relation between the susceptibility and temperature, better known as Curie law and Curie-Weiss law.

A.1 Classical theory of paramagnetism

We consider a unit volume of material containing n atoms, each having a magnetic moment μ. Let the direction of each moment be represented by a vector, and let all the vectors be drawn through the center of the sphere. The magnetic energy E_M is:

$$E_M = -\mu H \cos\theta.$$

Thermal energy tends to randomize the alignment of the moments. Langevin supposed that the moments are non-interacting in which case we can use classical Boltzmann statistics to express the probability of any given electron occupying an energy state E_M. If $k_B T$ is the thermal energy

$$P(E) = e^{-\frac{E_M}{k_B T}} \Rightarrow P(E) = e^{\frac{\mu H \cos\theta}{k_B T}}.$$

We wish to find the number dn of moments inclined at an angle between θ and $\theta + d\theta$ to the field **H**.

$$dn = 2\pi C \sin\theta d\theta,$$

where

$$\int_0^N dn = N,$$

C is a normalizing constant which gives the total number of moments per unit area. The probability then of find a magnetic moment in any position inside the sphere is:

$$dn = 2\pi C \sin\theta e^{\frac{\mu H \cos\theta}{k_B T}} d\theta, \tag{A.1}$$

Setting $a = \frac{\mu H}{k_B T}$, integrating both sides and leaving in evidence C we have that

$$C = \frac{N}{2\pi \int_0^\pi \sin\theta e^{a\cos\theta}}. \tag{A.2}$$

The total magnetization in the solid equals to:

$$M = \int_0^\pi \mu \cos\theta dn. \tag{A.3}$$

Combining Eq. A.1 and Eq. A.2 to find dn and substituting in Eq. A.3 we get

$$M = \frac{N\mu \int_0^\pi \sin\theta \cos\theta e^{a\cos\theta}}{\int_0^\pi \sin\theta e^{a\cos\theta}}. \tag{A.4}$$

If $x = \cos\theta$ and $dx = -\sin\theta$ then

$$M = \frac{N\mu \int_{-1}^{1} x e^x dx}{\int_{-1}^{1} e^x dx},$$

After solving each integral, we reach the expression:

$$M = N\mu \left(\frac{e^a + e^{-a}}{e^a - e^{-a}} - \frac{1}{a} \right), \tag{A.5}$$

or more precisely

$$M = N\mu \mathrm{L(a)}. \tag{A.6}$$

This is the Langevin equation for the magnetization of a paramagnet. L(a) is known as the Langevin function (Eq. A.7) and always lies in the range $-1 < \mathrm{L(a)} < 1$.

$$\mathrm{L(a)} = \coth(a) - \frac{1}{a}, \tag{A.7}$$

The Langevin theory leads to the Curie law for paramagnetic materials. Considering $a << 1$ then

$$\coth(a) = \frac{1}{a} + \frac{a}{3} + \mathcal{O}(a^3),$$

so $\mathrm{L(a)} \approx \frac{a}{3}$ and the magnetization has a value of

$$M = N\mu\frac{a}{3} \qquad \Rightarrow \qquad M = \frac{N\mu^2 H}{3k_B T}. \tag{A.8}$$

Since the susceptibility is $\chi = \frac{M}{H}$, we found Eq. A.9 which is Curie's law and $C = N\mu^2/3k_B T$

$$\chi = \frac{C}{T}. \tag{A.9}$$

The Langevin theory of paramagnetism, which leads to the Curie law, is based on the assumption that the individual carriers of magnetic moment (atoms or molecules) do not interact with one another, but are acted on only by the applied field and thermal agitation. But not every material obeys this behavior. In order to explain this phenomenon Weiss introduced the concept of *molecular field* (H_m) by postulating that the elementary moments do interact with one another. Assuming that $H_m = \gamma M$, where γ is called the molecular field constant. Therefore, the total field acting on the material is

$$H_t = H + H_m.$$

Then,

$$\chi = \frac{M}{H_T} = \frac{M}{H + \gamma M} = \frac{C}{T}.$$

Solving for M, we find the Curie-Weiss law, where

$$\chi = \frac{C}{T - \gamma C} \qquad \Rightarrow \qquad \chi = \frac{C}{T - \Theta}. \tag{A.10}$$

Θ is a measure of the strength of the interaction because it is proportional to the molecular field constant γ and has both, positive and negative values. It is important to note that the molecular field is in no sense a real field; it is rather a force, which tends to align or disalign the atomic or molecular moments.

A.2 Quantum theory of paramagnetism

The central postulate of quantum mechanics is that the energy of a system is not continuously variable. When it changes, it must change by discrete amounts. Fig A.1 represents both classical and quantum mechanics point of view, in the classical we can see that the magnetic moment can have any orientation along θ, but from the quantum mechanics picture this is not possible and only a few values are allowed.

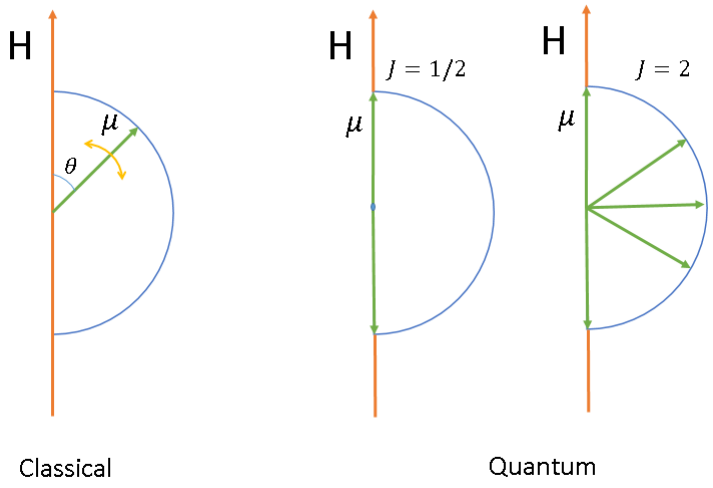

Figure A.1: Classical and quantum description of the magnetic moment

The rules governing space quantization are usually expressed in terms of angular momentum rather than a magnetic moment, so we need to establish the find the relation between orbital and spin moments. The orbital magnetic momentum is defined in Eq.A.11 and the spin magnetic moment in Eq. A.12.

$$\mu_{orb} = \frac{e}{2m}P_{orb}, \tag{A.11}$$

$$\mu_{spin} = \frac{e}{m}P_{spin}, \tag{A.12}$$

$$P_{orb} = \frac{sh}{2\pi} \qquad P_{orb} = \frac{1}{2}\frac{sh}{2\pi}.$$

From both equation we can infer a generalization for the effective magnetic moment (Eq. A.14), where g is better know as the Landé factor[1] and J is the total angular momentum.

$$\mu_{eff} = g\left(\frac{e\hbar}{2m}\right)\sqrt{J(J+1)}, \tag{A.13}$$

$$\mu_{eff} = g\sqrt{J(J+1)}\mu_B. \tag{A.14}$$

The possible values of μ_H, the component of μ_{eff} in the direction of the applied field H are $\mu_H = gM_J\mu_B$ where M_J is a quantum number associated with J and has $2J+1$ set of values. The maximum possible value for μ_H which is also the value for the magnetization saturation M_s is,

$$\mu_H = gJ\mu_B. \tag{A.15}$$

The energy of each moment in the field H is

$$E = -\mu_{eff}H = -gM_J\mu_B H. \tag{A.16}$$

Using the concepts of statistical mechanics and the formulation of the canonical ensemble we know that,

$$Z = \sum_{M_J} e^{-H(M_J)/k_BT} \qquad \Rightarrow \qquad Z = \sum_{M_J} e^{gM_J\mu_B H/k_BT},$$

or

$$Z = \sum_{M_J=-J}^{J} e^{xM_J}, \tag{A.17}$$

[1] $g = 1 + \frac{J(J+1)+S(S+1)-L(L+1)}{2J(J+1)}$

with

$$x = \frac{g\mu_B H}{k_B T}.$$

Remembering that in the canonical representation,

$$M = \frac{1}{Z}\frac{\partial Z}{\partial x}. \tag{A.18}$$

The calculation of the partition function (Eq. A.17) and $\frac{\partial Z}{\partial a}$ (setting $a = x/2$) after some quite tedious mathematics leads to

$$Z = \frac{\sinh\left(\sinh(2J+1)x/2\right)}{\sinh(x/2)} \tag{A.19}$$

$$\frac{\partial Z}{\partial a} = \frac{(2J+1)\cosh\left((2J+1)a\right)\sinh a - \sinh\left((2J+1)a\right)\cosh a}{\sinh^2 a}. \tag{A.20}$$

Then

$$\begin{aligned}\frac{1}{Z}\frac{\partial Z}{\partial a} &= (2J+1)\frac{\cosh\left((2J+1)a\right)}{\sinh\left((2J+1)a\right)} - \frac{\cosh a}{\sinh a} \\ &= (2J+1)\coth\left((2J+1)a\right)\coth a.\end{aligned}$$

Dividing by $M_s = g\mu_B J$, and leaving all in terms of x we have the well-known Brillouin function

$$B_J(x) = \frac{2J+1}{2J}\coth\left(\frac{2J+1}{2J}\frac{x}{2}\right) - \frac{1}{2J}\coth\left(\frac{1}{2J}\frac{x}{2}\right). \tag{A.21}$$

A.3 Hund's rules

This section has been adapted from Chikazumi [16], Jiles [9] Gezlaff [39] and Coey [36]. First of all, it is neccesary to introduce the concept of quantum angular momentum operators:

- **S**. Spin angular momentum.
- **L**. Orbital angular momentum.

- **J**. Total angular momentum (**J=L+S**)

Hund provided an empirical prescription for determining the lowest-energy state of a multielectron atom or ion. Hund's rules are three and described as follows:

1. The spins s_i, are arranged so as to form a resultant spin **S** as large as possible within the restriction of the Pauli exclusion principle.

2. The orbital vectors l_s, of each electron are arranged so as to produce the maximum resultant orbital angular momentum **L** within the restriction of the Pauli exclusion principle and also the first rule.

3. the total atomic angular momentum J is equal to IL - SI when the shell is less than half full, and is equal to IL + SI when the shell is more than half full. When the shell is exactly half full $L = 0$ so that $J = S$.

The justification for the first rule is that electrons minimize their Coulomb interaction by avoiding each other, which is best achieved if they can occupy different orbitals. The second rule means that the electrons orbit in the same sense whenever possible. The third and weakest rule is a consequence of the sign of the spin-orbit coupling. Hund's rules only predict the ground state; they tell us nothing about the position and order of the excited states.

One example for the ground state of Eu is given:

$$\begin{aligned} Eu(4f^7) \quad & n = 4 \quad & l = 3 \\ \mathbf{L} = 0 \quad & \mathbf{S} = 0 \quad & \mathbf{J} = 0 \\ \Rightarrow \quad & g = 0. \end{aligned}$$

As seen before this value is wrong (see Section 2.1), hence we proved that Hund's rules have certain limitations, but they offer a good approach to define the ground state in some ions.

Appendix B

GMI measurement system

In this section, we will present some aspects involved in the set-up of a GMI measurement system, which consisted of two phases: the first one, was focus on developing the required electronic to turn a DC unipolar power supply into a bipolar source for a DC electromagnet. In the second stage, we implement a user-friendly interface in LabVIEW which has the ability to control the power supply source changes as well as record the data from the experiment (voltage (**V**) and DC magnetic field **H**).

B.1 Power supply connection

As stated before used two *Agilent N5769A DC Power Supply* power supply of the same voltage (100 V) and current rating (15 A) which can be connected in parallel (Fig. B.1) to provide up two times the output current capability in a master-slave configuration. In this set-up one, the power supply sources are controlled manually or automatically (PC) -master- and the other one

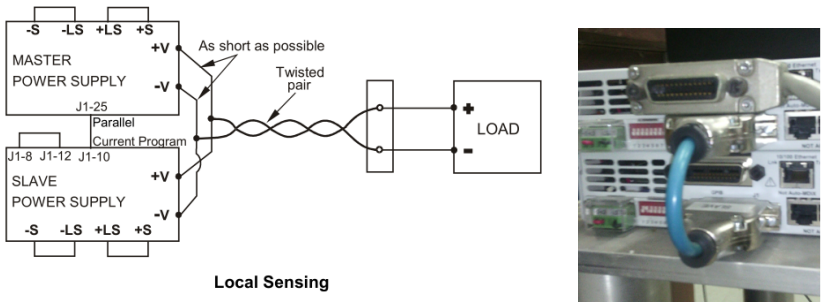

Figure B.1: Parallel connection for local sensing

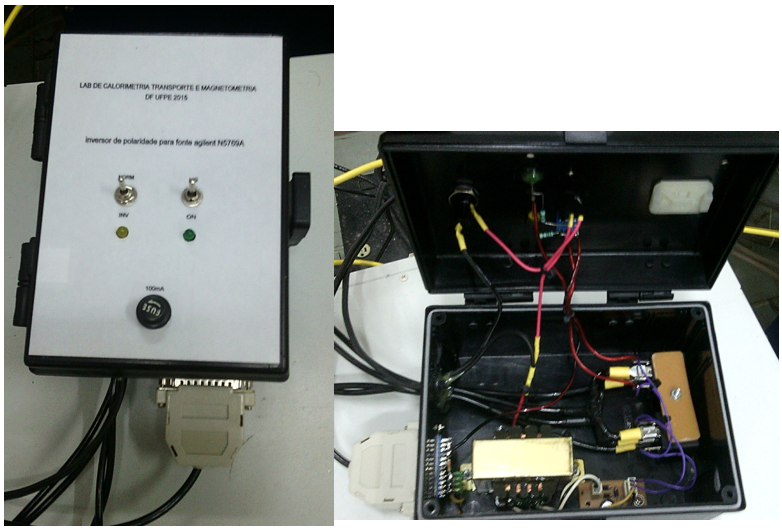

Figure B.2: Current polarization switch

(slave) follows every move made by the master. Therefore, is we need an output of 5A, the output from each power supply will be 2.5 A, if not, there is something wrong in the master-slave connection.

With the help of the electronics division of the Physics Department, we built an electronic relay (switch) which can be controlled manually or configured to work using the PC parallel port with a 0 V-5 V input signal (Fig. B.2). This input helps us to determine and change the polarity in which the supply source should run, for a 0V we have a supply from 0 A to +30 A, and in the high state, we have an inversion of the polarity, 0 A to -30 A. This means +6 kOe for 0 V and -6 kOe for 5 V. The electric diagram is shown in Fig. B.3; one of the most important factors is that the PC control is made through the PIN2 of the serial port. LabVIEW determines

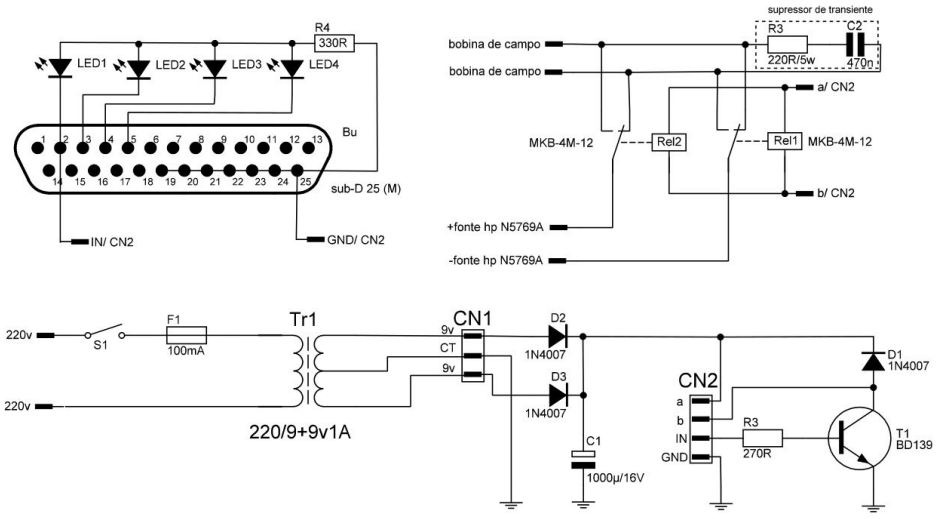

Figure B.3: Electric circuit

in which state this output is - low or high- and then sets the polarization in which we want to start the measurement.

B.2 LabVIEW interface

We wanted to control how the current is provided to the electromagnet and measure at the same time the changes in magnetic field and voltage in a test sample. Thus, we used LabVIEW to control and record this measurement. In here we will make a brief introduction to the program, due to the fact that is quite complicated and therefore not the aim of our work.

First of all, we need to establish the parameters of the measurement: maximum current, steps or $\Delta\mathbf{I}$, delay (ms) (between the measurements) and the path in which we want to save our files. These parameters are introduced by the user in the interface (Fig. B.4). The current limit is set to 28 A, even though the maximum output current is set to be 30 A; there is also a voltage limitation for both power supply sources in nearly 70 V, to avoid any overheat or overcurrent problems. There is also a text box in which we can write the path of the measurement that we want to graphically monitor during the execution of the program (measurement of V vs H).

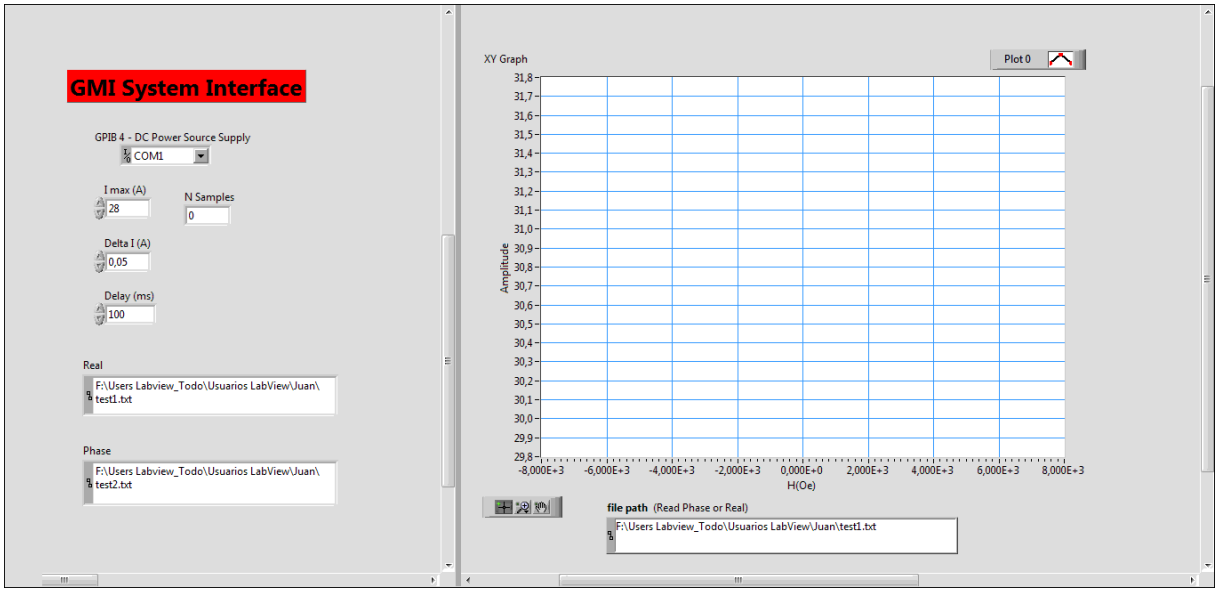

Figure B.4: GMI user interface in LabVIEW

Now, let us enumerate some of the most important stages in which the program executes:

1. The program starts sending a signal through the parallel port to the electronic switch, in order to know if it is at a low or high level. It will always start from the low level (0 V

input).

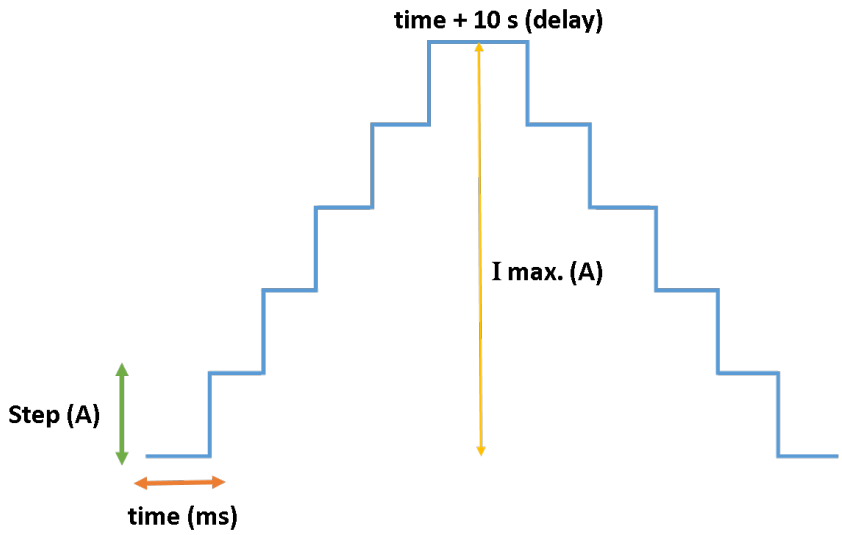

Figure B.5: Controlled current output

2. Set the output to 0 V and wait for 10 s.

3. Initiate the *saving file* routine and after 10 s begin the sequence shown in Fig. B.5. Every step or delta is taken by the program to the DC power supply. The delay not only represents the amount of time between each step but also how much time do the program take to record a measurement of both magnetic field and voltage.

4. After reaching its goal (maximum current), the system waits for 10 seconds and begins to decrease the current output.

5. Once it reaches the zero value in the current, the program waits for 10 seconds. This delay was included in the program, so the electrical control system has a quite high response time to invert the polarity in the electromagnet.

6. Send a 5 V signal through the parallel port to the control box.

7. Start the current output (staircase-like signal Fig. B.5) in the range between 0 kOe to -6 kOe and then -6 kOe to 0.

8. Once again as it reaches zero value in current, set the parallel output to low (0 V), wait for 10 s and start the current output until the maximum value is achieved. This last *staircase* closes the hysteresis loop cycle.

9. Finally as the maximum current value is reached for the third time (+28 A, -28 A and +28 A) end the program.

10. To end the program correctly, set all the outputs to zero (DC power supply and parallel port) and save the data files.

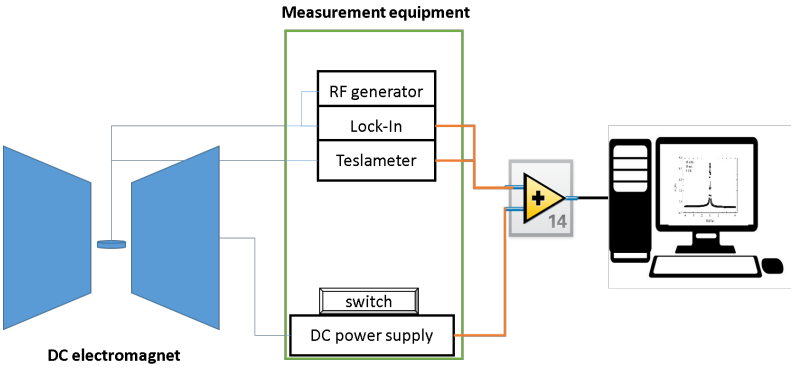

Figure B.6: GMI measurement set-up

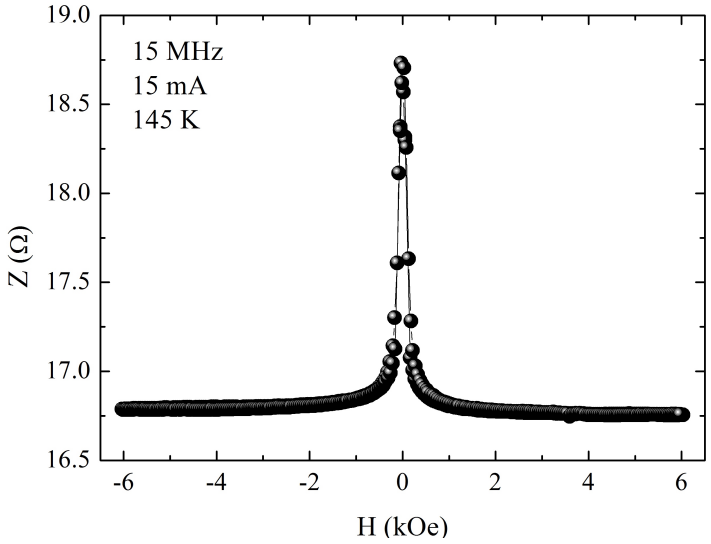

Figure B.7: Impedance as function of the magnetic field measured at 15 MHz and 145 K for a Fe_9Zr_{91} ribbon

By using this program and the set-up shown in Fig. B.6 we have made several measurements of giant magnetoimpedance (GMI) as a function of frequency and temperature on different systems, such as FeZr and CoNi. Fig. B.7 represents one of those curves, where we have the impedance as a function of temperature and frequency for Fe_9Zr_{91} amorphous ribbon.

C

Appendix C

Events and abstracts

Thanks to the help of the physics department and the contribution of several founding agencies we were able to participate in two national congress. The corresponding abstracts are presented.

- **XXXVIII Encontro Nacional de Física da Matéria Condensada**, may 24 to 28 of 2015, Foz do Iguaçu, PR. *Poster presentation*.

Effect of iron substitution in the structural and magnetic properties of the $EuCrO_3$ chromite

Juan Marcos Marín Ramirez, Fernando Luis de Araujo Machado
Departamento de Física, Universidade Federal de Pernambuco, 50670-901, Recife, Pernambuco, Brazil

Hermínia Veridiana dos Santos Pessoni, Adolfo Franco Júnior
Instituto de Física, Universidade Federal de Goiás, C.P. 131, 74001-970 Goiânia, Goiás, Brazil

A comparative study of the structural, magnetic, and thermal properties of europium chromites doped with iron ($Eu_{1-x}Fe_xCrO_3$) is presented. Powder samples were synthesized by a combustion reaction method by using urea as fuel and by combining stoichiometrically the reactants. Rietveld analysis of the X-ray diffraction (XRD) patterns at room temperature for $EuCrO_3$ nanopowders shows a perovskite orthorhombic structure (*Pnma*) without the presence of extra diffraction peaks indicating that the samples have a high degree of purity. The lattice parameters obtained (a = 5.5286(2) Å, b = 7.6430(2) Å and c = 5.3480(2) Å) are close to those reported while the average crystallite size was found to be 65.62 ± 0.54 nm. It was also found that the presence of a residual phase, identified as magnetite (Fe_3O_4), when Fe added to the pure chromite sample. The iron concentration modifies both the structure and the magnetic properties of the chromite samples. For x higher than 0.8 the main phase is $FeCr_2O_4$ with lattice parameter of 8.3188 (4) Å and an average crystalline size of about 290 nm. The thermal decomposition process was investigated by using differential scanning calorimetry and thermal gravimetric analysis (TG-DSC). For both x=0.0 and x =1.0 systems, there is a maximum weight loss of 3% and a minor weight gain after 1000 ^{o}C. In general indicating that both reactions were quite stable in terms of mass loss. The DSC analysis for the $EuCrO_3$ sample (x=0.0) showed a broad peaks typical of exothermic reactions at around 500 ^{o}C while for x=1.0 the sample presents two well-defined exothermic peaks at 370 ^{o}C and at 650 ^{o}C. A vibrating sample magnetometer was used for measuring hysteresis loops at room temperature for magnetic fields up to 20 kOe. At room temperature $EuCrO_3$ is paramagnetic while the Fe-doped samples showed ferromagnetic behavior that gradually enhances as the Fe concentration is increased. For instance, the coercive field (H_c) and the remanence (M_r) increases from 0 to 280 Oe and from 0 to 0.77 emu/g, respectively, and the magnetization at the highest applied field M(H_{max}) varies from 0.33 to 3.75 emu/g when x is increased from 0.0 to 1.0. The results will be discussed by taking into consideration the change in the lattice parameters and the presence of the magnetite phase. Work partially supported by CNPq, CAPES, FACEPE and FINEP.

- **XXXIII Encontro de Físicos do Norte e Nordeste**, November 9 to 11 of 2015, Natal, RN. *Oral presentation*.

Room temperature magnetic study of the $HoCrO_3$ chromite synthesized by combustion reaction method

J.M. Marín, A.R. Rodrigues, F.L.A. Machado
Departamento de Física, Universidade Federal de Pernambuco, 50670-901, Recife, Pernambuco, Brazil

H. V. S. Pessoni, A. Franco Jr
Instituto de Física, Universidade Federal de Goiás, C.P. 131, 74001-970 Goiânia, Goiás, Brazil

Combustion reaction synthesis is a versatile, effective, low cost and fast method to produce materials in a nanometric scale. Rare earth based chromites have been receiving a great deal of attention due their possible application as multifunctional materials, coupling electrical and magnetic properties. Powder samples of $HoCrO_3$ were synthesized by using a combustion reaction method with urea as fuel. Calculations of the Goldschmidt factor ($t \approx 0.81$) indicate that this system should form a perovskite-like structure. However, X-ray diffraction and transmission electron microscopy images obtained for the as-prepared samples revealed an amorphous phase only. Therefore, a subsequent annealing was performed for 12h, 24h, 48h and 72h for crystallizing the samples. Rietveld refinement analysis reveals that after 12h a single phase orthorhombic perovskite structure (Pnma) of holmium chromite is achieved. This time scale is relatively faster compared to those reported. Lattice parameters remains practically constant ($a = 0.5523(2)$ nm, $b = 0.7540(3)$ nm and $c = 0.5245(2)$ nm) while the average crystallite size increases from about 120 nm to 240 nm. The thermal decomposition process was examined using differential scanning calorimetry and thermal gravimetric analysis (DSC- TGA) up to 1200^{o}C. The weight loss determined by TGA was nearly of 10%, indicating that the reaction process is stable. The DSC data showed a major endothermic peak approximately at 700^{o}C. The magnetization was measured using a vibrating sample magnetometer (VSM) for applied magnetic fields (H) up to 20 kOe. It was found that $HoCrO_3$ is paramagnetic at room temperature even for the annealed samples. Nevertheless, an increase in the susceptibility is observed after crystallization is achieved. Work partially supported by CNPq, CAPES, FACEPE and FINEP.